



OLLSCOIL NA GAILLIMHE
UNIVERSITY OF GALWAY

TITLE OF PROJECT

GRAVITY ENERGY STORAGE SYSTEM

by

JONATHON MURPHY

A project submitted in partial fulfilment of the requirements for the degree of

M.E. in Energy Systems Engineering

UNIVERSITY OF GALWAY

Date

11/04/2025

Project Supervisor: Dr. MAEVE DUFFY

ABSTRACT

DESIGN OF A GRAVITY ENERGY STORAGE SYSTEM

JONATHON MURPHY

Year of proposed Graduation 2025

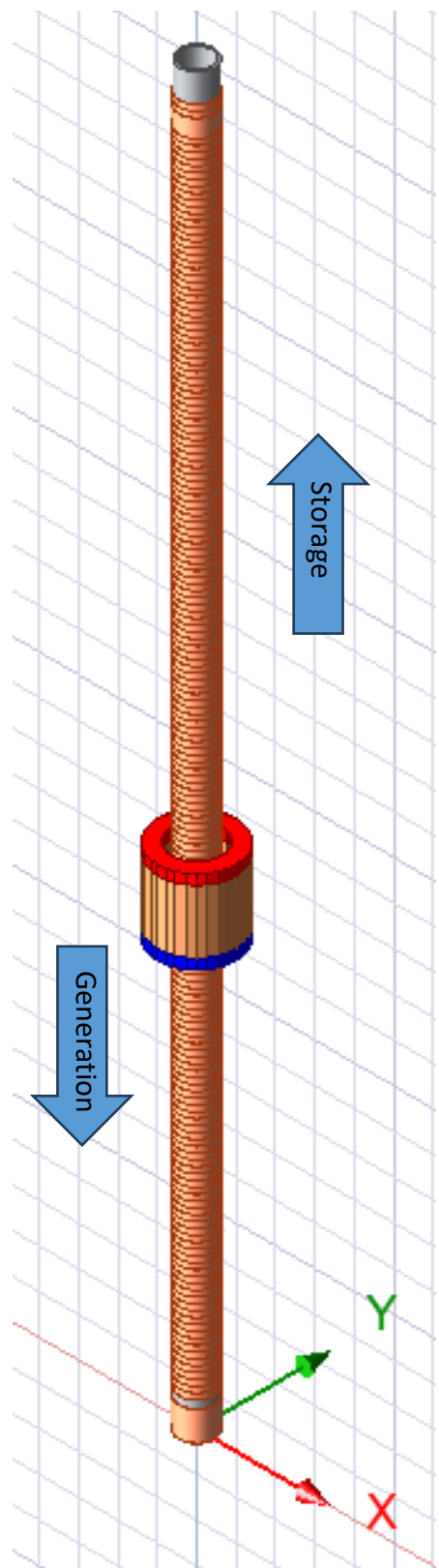
Advisor: Dr MAEVE DUFFY

Degree: ENERGY SYSTEMS ENGINEERING

As renewable energy penetration increases, energy storage systems must address the challenges of intermittency and grid reliability. This thesis explores a novel Electro-Magnetic Gravity Energy Storage (EMGES) system, which lifts a mass using electrical input and regenerates energy via electromagnetic induction during its descent. A 132-coil small-scale prototype was designed, simulated, and experimentally tested to assess its viability. Results showed energy outputs of up to 18.5 W and 1.04 J per coil drop, with storage mode efficiencies ranging from 0.49% to 1.87%. Simulations in Ansys Maxwell and LTSpice validated electromagnetic coupling and circuit behaviour. A scaled 400 m mineshaft model demonstrated the system's potential 2 kWh capacity but revealed significant electrical demands and low round-trip efficiency. A Levelized Cost of Storage (LCOS) analysis yielded values between €924 and €1,258/kWh, reflecting current design limitations. Despite these challenges, the system offers a modular, mechanically simple alternative to chemical storage, with future improvements focusing on regenerative braking, superconducting coils, and advanced control strategies.

Keywords: Electro-Magnetic Gravity Energy Storage, renewable energy, gravity energy storage, Ansys Maxwell, Electromagnetics, LCOS, grid stability, solar PV, energy systems engineering.

GRAPHICAL ABSTRACT



ACKNOWLEDGEMENTS

I would like to express my deepest gratitude to my supervisor, Dr Maeve Duffy, for her invaluable guidance, support, and encouragement throughout this project. Her technical expertise, constructive feedback, and consistent availability during our weekly meetings were instrumental in shaping the direction of this thesis. I am especially thankful for her assistance in the lab, where her insights helped bring the practical aspects of this work to life.

I would also like to extend sincere thanks to my friends and extended family, who have been a constant source of encouragement and understanding. Your support, patience, and belief in me have made this journey lighter and more meaningful—and I know you'll be just as relieved and proud as I am to see this thesis completed.

To my dad, John—thank you for always keeping me grounded. Your willingness to listen, even when I went on for far too long, and your steady reassurance have meant the world to me. You reminded me to keep pushing forward, especially when it mattered most.

And finally, to my mom, Jacqui. Your unwavering belief in me and your constant encouragement to aim high and never back down from a challenge continue to inspire me every day. Although you're not here to witness the final result, I carry your strength with me always—and I know you would be proud.

PLAGIARISM DECLARATION

Energy Systems Engineering, University of Galway

--	--	--

Student Number

Family Name

Other Names

Design of a Gravity Energy Storage System

I declare that:

1. I have read and understood both the University of Galway Code of Practice on Plagiarism and “Plagiarism – a guide for engineering and computer science students in the University Galway”.
2. I am the original author of all work included in this report, except for material which has been fully and properly acknowledged using a standard referencing method.
3. The material in this report has not been presented for assessment in any other course in this university or elsewhere.
4. I have taken all reasonable care to ensure that no other person has been able to copy any part of this report either in paper or electronic form.

	11/04/2025
--	------------

Signature

Date

TABLE OF CONTENTS

1	Introduction	1
1.1	Chapter overview.....	1
1.2	Background & Motivation.....	1
1.3	Aims and objectives	2
1.4	Thesis outline	3
1.5	Chapter summary	4
2	Literature review.....	5
2.1	Chapter overview.....	5
2.2	The Growing Importance of Energy Storage in the Renewable Energy Transition ...	5
2.3	Existing Systems Study.....	6
2.4	Academic Research Papers	29
2.5	Gap Analysis.....	32
2.6	Chapter summary	35
3	Methods.....	36
3.1	Chapter overview.....	36
3.2	Principle of Operation and Background of EMGES.....	36
3.3	Fundamental Principles and Governing Equations.....	45
3.4	Prototype Component Options and Selection.....	48
3.5	Electromagnetic Prototype Design	57
3.6	Prototype Implementation	76
3.7	Experimental Validation.....	78
3.8	System Modelling and Simulation	80
3.9	Chapter summary	84
4	Results, Analysis & Discussion	85
4.1	Chapter overview.....	85
4.2	Flux Distribution (Generation mode).....	85
4.3	Magnet v Iron Core Position	91
4.4	Coil & PM Zones of Interaction (Storage mode).....	95
4.5	Performance Results.....	108
4.6	Scaled -Up Model.....	121
4.7	Scaled-Up EMGES LCOS	124
4.8	Exploration of Unimplemented Design Concepts.....	127
4.9	Chapter Summary	130
5	Conclusions and Future Work.....	131

5.1	Summary of Findings.....	131
5.2	Conclusions	131
5.3	Future work.....	133
6	References	135

TABLE OF FIGURES

Figure 2.3.1 : ARES	7
Figure 2.3.2 : Gravitricity Mine Shaft.....	7
Figure 2.3.3 : Energy Vault Storage Method.....	8
Figure 2.3.4 Lithium-Ion BESS	9
Figure 2.3.5 Flow battery operation [29].....	10
Figure 2.3.6 : Lead Acid Battery	11
Figure 2.3.7 : Linear Electric Machine Concept	12
Figure 2.3.8 : LEM Operation	12
Figure 2.3.9 : Traditional PHES.....	15
Figure 2.3.10 : Open Pit Mines.....	16
Figure 2.3.11 : Abandoned Coal Mines.....	17
Figure 2.3.12 : Buoyancy Energy Storage Experimental Setup.....	18
Figure 2.3.13 : WGES Comparison	20
Figure 2.3.14 : Gravity Power Module	21
Figure 2.3.15 : Deep Ocean Gravity Energy Storage Plan.....	25
Figure 2.3.16 : SMES System Operation	27
Figure 2.4.1 : Energy Storage Rating Comparison	32
Figure 3.2.1 : EMGES Operation Flow chart	37
Figure 3.2.2 : Ansys Maxwell Design Setup fully Depleted from Generation Mode, Real Setup Operating in Storage Mode	38
Figure 3.2.3 : Conceptual flow diagram of the proposed EMGES integration with a DC-coupled solar PV system and the AC grid	41
Figure 3.2.4 : Central European Live Grid [49].....	42
Figure 3.2.5 : Multiple PMs and Mass Configuration for Increased Energy Capacity	44
Figure 3.4.1 : Possible Magnet Shapes [66]	53
Figure 3.4.2 : Bronze Weight	55
Figure 3.5.1 : B-H Loop of Magnetic Material [67]	58
Figure 3.5.2 : Ring Magnet Ansys Maxwell	59
Figure 3.5.3 : Material Properties of PM	60
Figure 3.5.4 : Magnetic Flux Density and Field Strength	60
Figure 3.5.5 : Iron Core in Ansys Maxwell.....	61
Figure 3.5.6 : Summary of Iron Core Properties	62
Figure 3.5.7 : Bronze Weight Ansys Maxwell.....	65
Figure 3.5.8 : Permanent Magnet vs. Magnet with Bronze Weight Flux Density	65
Figure 3.5.9 : Set Eddy Effects.....	66
Figure 3.5.10 : Magnetic Flux Density with PVC	66

Figure 3.5.11 : EMGES Cross Section with Radii	67
Figure 3.5.12 : Magnetic Flux Gradient vs Distance	68
Figure 3.5.13 : Flux Gradient Comparison	69
Figure 3.5.14 : EM and Lengths of Analysis at Different Coordinates	71
Figure 3.5.15 : Force Analysis of Components.....	72
Figure 3.5.16 : Force Direction.....	72
Figure 3.5.17 : Ansys Maxwell Simulation Setup	73
Figure 3.5.18 : AWG Size Comparison [69]	75
Figure 3.6.1 : PM and Weight Housing	77
Figure 3.6.2 : EMGES Base Assembly (a) The bare structural base serving as the foundation; (b) The fully assembled base with the integrated system installed	77
Figure 3.6.3 : EMGES Top Mount for Stability and Cable Management	78
Figure 3.8.1 : LTSpice simulation of an H-bridge controlling coil energisation for EMGES storage mode	82
Figure 4.2.1 : Drop Test Time Collection.....	86
Figure 4.2.2 : EMF Induced in 45 Turn Prediction	87
Figure 4.2.3 : EMF Induced in 135 Turn Prediction	87
Figure 4.2.4 : Actual 45 Turn EMF Pattern for 1 Coil	89
Figure 4.2.5 : Predicted EMF Pattern for 1 Coil	90
Figure 4.3.1 : Magnetic Force of Attraction vs Distance.....	91
Figure 4.3.2 : PM and Iron Core z-axis Alignment and Misalignment	92
Figure 4.3.3 : Force vs Alignment Offset Ring Magnet	93
Figure 4.3.4 : Disk PM Inside Iron Core.....	94
Figure 4.3.5 : Force vs Alignment Offset Disk Magnet	94
Figure 4.4.1 : Single PM and EM Setup for Force Analysis	95
Figure 4.4.2 : Magnetic Flux Density on each line	97
Figure 4.4.3 : Ampere-Turns vs Lateral Distance from Coil	99
Figure 4.4.4 : Force vs Distance Plot for Line 1.....	100
Figure 4.4.5 : Force vs Distance Plot for Line 2.....	100
Figure 4.4.6 : Force vs Distance Plot for Line 3	101
Figure 4.4.7 : 3D Simulation Force Output ($N = 135, I = 1.04 A$)	102
Figure 4.4.8 : Acceleration and Velocity vs Distance	104
Figure 4.4.9 : Overlapping Coil Segment	105
Figure 4.5.1 : EMGES in Storage Mode	111
Figure 4.5.2 Predicted Power vs Actual Power 45 Turns [72]	113
Figure 4.5.3 : Predicted Power vs Actual Power 45 Turns.....	114
Figure 4.5.4 : AWG 28 vs 24 Power Output Prediction.....	115

Figure 4.5.5 : LTSpice Rectifier Circuit Using Measured EMF as PWL Input.....	120
Figure 4.5.6 : Output Voltage from LTSpice Simulation of Experimental EMF Through Bridge Rectifier.....	120
Figure 4.8.1 : Halbach Array Field Lines Diagram [77].....	128
Figure 4.8.2 : 3-Coil Magnetic Flux Density Vectors	129

TABLE OF TABLES

Table 1 PHES Technical Specification.....	15
Table 2 HHS vs GBES	24
Table 3 Key Parameters	26
Table 4 Iron v Silicon Steel Comparison.....	50
Table 5 AWG Comparison [65].....	51
Table 6 AWG Recommendation Per Line.....	107
Table 7 Line & AWG Comparison.....	112
Table 8 45 Turn, 28 AWG Theoretical & Actual Waveform	116
Table 9 Comparison of Theoretical v Actual Power Output	117
Table 10 Comparative Performance Summary.....	118
Table 11 2kWh Scaled-up Parameters.....	121
Table 12 Comparison of Scaled Storage Methodology	122
Table 13 Operating Comparison Assumptions	125
Table 14 Scales EMGES CAPEX.....	125
Table 15 Scaled EMGES OPEX	125
Table 16 Scaled Scenario Comparison	126
Table 17 SOTA Technology Comparison	126

GLOSSARY OF TERMS

Term	Meaning	Units
<i>Roman letters</i>		
V	Voltage	Volts (V)
R	Resistance	Ohms (Ω)
I	Current	Amps (A)
F	Force	Newton's (N)
m	Mass	Kilogram (kg)
v	Velocity	Meters per Second (ms^{-1})
l	Coil Length	Meters (m)
t	Time	Seconds (s)
x	Position/Displacement	Meters (m)
B	Magnetic Flux Density	Tesla (T)
A	Area	m^2
N	Number of Turns	
P	Power	Watts (W)
L	Inductance	Henries (H)
\Re	Reluctance	Webers (Wb)
F	Magnetomotive Force MMF	Ampere-Turns (A-t)
<i>Greek letters</i>		
α	Angle of attack	radians
μ_0	Permeability of Free Space	
μ_r	Relative Permeability	
ϵ	Electromotive Force (EMF)	Volts (V)
ϕ	Magnetic Flux	Webers (Wb)
γ	Flux Linkage	Weber-turns (Wb-t)
η	Efficiency	%

ρ	Density	kg/m ³
θ	Angle	Degrees (°)
<i>Acronyms</i>		
MW	Megawatt	-
PM	Permanent Magnet	-
LCOS	Levelized Cost of Storage	
kWh/m ³	Kilowatt hour per cubic meter	
EM	Electromagnet	
FWR	Full Wave Rectifier	
HWR	Half Wave Rectifier	
AC	Alternating Current	
DC	Direct Current	
RMS	Root Mean Squared	$\sqrt{2}$

1 INTRODUCTION

1.1 Chapter overview

This chapter introduces the pressing need for advanced energy storage solutions to support the integration of renewable energy sources, such as solar power, into modern electricity grids. It outlines the motivation behind developing the Electro-Magnetic Gravity Energy Storage System (EMGES) as a sustainable alternative to conventional chemical batteries, emphasising its potential to address intermittency challenges. The aims and objectives of the thesis are presented, focusing on designing, simulating, and evaluating a small-scale EMGES prototype to assess its technical and economic feasibility. Additionally, the chapter provides an overview of the thesis structure, setting the stage for a detailed exploration of this innovative storage technology.

1.2 Background & Motivation

In the current global energy paradigm, the transition towards sustainable power sources is not merely desirable but imperative. This shift is driven by the quantifiable environmental degradation associated with fossil fuel consumption, which remains the predominant source of anthropogenic greenhouse gas emissions. As the engineering community seeks to mitigate the environmental footprint of traditional energy generation, renewable energy technologies emerge as both a necessary and a viable alternative. These technologies, which include solar, wind, hydroelectric, and geothermal energy, harness natural processes that are inherently replenishable and have minimal environmental impacts compared to conventional power systems.

Solar energy exemplifies the potential of renewables due to its ubiquity and scalability. Advances in photovoltaic (PV) technology have significantly enhanced the efficiency and economic viability of solar installations. The dramatic reduction in the cost per watt of PV modules over the past decade has propelled solar energy to the forefront of competitive alternative energy sources. This cost-effectiveness, coupled with the decentralized nature of solar power generation, facilitates localized energy solutions that circumvent the logistical and economic challenges of extensive grid infrastructure and reduce transmission losses.

However, the integration of solar energy into the power grid introduces complexities due to its intermittent nature. Solar output fluctuates with diurnal cycles and meteorological conditions, necessitating robust solutions for energy storage and load balancing. Herein lies the critical role of advanced energy storage technologies, which ensure the stability and reliability of power supply by decoupling the timing of energy generation from its consumption.

Amongst energy storage systems, Systems EMGES represent a novel approach by leveraging the principles of gravitational potential energy and magnetic levitation. These systems store energy by using surplus power to elevate a mass in a gravitational field; energy is

subsequently recovered by allowing the mass to descend, converting potential energy back into electrical energy through regenerative braking systems. This method is not only highly efficient but also exhibits low round-trip energy losses, which are crucial for maintaining the overall efficiency of renewable energy systems.

The engineering implications of EMGES are profound. They offer a scalable and efficient solution for storing renewable energy, crucial for stabilizing renewable-heavy power grids. Moreover, the inherent simplicity of gravity-based storage mechanisms—wherein energy is stored mechanically rather than chemically—minimizes the environmental risks and operational complexities associated with chemical battery storage solutions. The longevity and durability of EMGES, free from the degradation issues that affect batteries, render it a sustainable choice for long-term energy storage.

The potential for EMGES and similar kinetic energy storage systems in the context of renewable energy integration is substantial. As engineers, the development of such innovative systems not only addresses the immediate technical challenges of renewable integration but also aligns with broader sustainability goals. By enhancing the dispatchability of renewable sources and reducing dependency on fossil-fuel-based peaking power plants, EMGES contributes to a more sustainable and resilient energy infrastructure.

In summary, the exploration of the framework of renewable energy integration represents a compelling area of study. It addresses key technical challenges in the energy sector, including energy storage, grid stability, and renewable integration, making it a pivotal topic for research and development in the pursuit of sustainable energy solutions for the future.

1.3 Aims and objectives

1.3.1 Aims

The overarching aims of this thesis are to:

Enhance Renewable Energy Integration: Improve the reliability and stability of renewable energy grids, with a focus on solar power, by developing an advanced storage solution to mitigate intermittency and variability. This aim seeks to demonstrate how the Electro-Magnetic Gravity Energy Storage System (EMGES) can store surplus solar energy and release it on demand, supporting consistent grid performance.

Pioneer a Novel Energy Storage Technology: Design and validate a groundbreaking energy storage system using EMGES that harnesses gravitational potential and electromagnetic forces. This aim emphasizes creating a sustainable alternative to conventional storage methods like chemical batteries, prioritizing scalability and mechanical simplicity over short-term efficiency.

1.3.2 Objectives

The specific technical objectives designed to achieve these aims are:

Design and Simulation of a Small-Scale EMGES:

- **Objective:** To design a scaled-down model of the EMGES using Ansys Maxwell [1] and other relevant engineering tools. This model will incorporate advanced materials and electromagnetic design principles to optimize the storage capacity and efficiency of the system.
- **Expected Outcome:** A comprehensive design blueprint and simulation results that validate the feasibility and functionality of the EMGES model under varying operational conditions.

Integration of EMGES with DC Power Source Systems:

- **Objective:** To develop a detailed plan and simulation for integrating the EMGES with existing solar PV systems. This includes designing the necessary electronic control systems to manage the energy flow between the solar panels, EMGES, and the grid.
- **Expected Outcome:** A simulation-based demonstration showing effective management of surplus solar energy, including storage and redistribution capabilities of the EMGES, enhancing solar PV's utility during peak and off-peak periods.

Evaluation of System Performance and Efficiency:

- **Objective:** To evaluate the performance, efficiency, and sustainability of the EMGES through rigorous testing and analysis. This objective focuses on assessing the system's energy conversion rates, round-trip efficiency, and operational longevity compared to traditional energy storage methods.
- **Expected Outcome:** Empirical data and analysis reports that benchmark the EMGES's performance against conventional energy storage systems, providing insights into its operational advantages and potential improvements.

Analysis of Technical and Economic Feasibility

- **Objective:** To evaluate the technical scalability and economic viability of EMGES, including a levelized cost of storage (LCOS) analysis and comparison with conventional storage technologies, while identifying key deployment challenges.
- **Expected Outcome:** A report detailing EMGES's scalability, LCOS, and technical hurdles, providing a basis for future optimization rather than broad adoption.

These objectives are structured to not only address the technical and operational aspects of the EMGES but also to highlight its broader implications for renewable energy systems globally. By achieving these objectives, this thesis will contribute valuable knowledge and practical solutions to the field of renewable energy storage and management.

1.4 Thesis outline

This thesis is structured across five chapters to systematically explore the Electro-Magnetic Gravity Energy Storage System (EMGES) as a potential solution for renewable energy storage. Following this introductory chapter, Chapter 2 provides a detailed literature review,

examining a range of existing energy storage technologies—including dry and wet gravity systems, electrochemical batteries, and emerging concepts—to situate EMGES within the broader field and identify its prospective benefits. Chapter 3 outlines the methodology, describing the design, simulation, and experimental testing of a small-scale EMGES prototype using tools such as Ansys Maxwell, alongside its simulated integration with solar photovoltaic systems. Chapter 4 assesses the system’s performance, presenting efficiency results for storage and generation modes, a scaling analysis based on a 400 m shaft, an economic feasibility evaluation through levelized cost of storage (LCOS), and a discussion of unimplemented design concepts such as Halbach arrays. Finally, Chapter 5 draws together the findings, evaluates the achievement of the stated aims and objectives, and suggests future research directions to improve the efficiency and practical applicability of EMGES for grid-scale deployment.

1.5 Chapter summary

This introductory chapter has established the critical need for advanced energy storage to support renewable energy integration, with a particular focus on addressing the intermittency of solar power through the Electro-Magnetic Gravity Energy Storage System (EMGES). It has outlined the thesis’s aims to enhance renewable energy reliability and pioneer a novel storage technology, alongside specific objectives covering the design, simulation, performance evaluation, and feasibility analysis of EMGES. The chapter has also provided a structural overview, detailing the progression of the subsequent chapters. The next chapter reviews existing energy storage technologies to contextualise EMGES within the field.

2 LITERATURE REVIEW

2.1 Chapter overview

This chapter introduces the pressing need for advanced energy storage solutions to support the integration of renewable energy sources, such as solar power, into modern electricity grids. It outlines the motivation behind developing the Electro-Magnetic Gravity Energy Storage System (EMGES) as a sustainable alternative to conventional chemical batteries, emphasising its potential to address intermittency challenges. The aims and objectives of the thesis are presented, focusing on designing, simulating, and evaluating a small-scale EMGES prototype to assess its technical and economic feasibility. Additionally, the chapter provides an overview of the thesis structure, setting the stage for a detailed exploration of this innovative storage technology.

2.2 The Growing Importance of Energy Storage in the Renewable Energy Transition

Energy Storage Systems (ESS) are becoming increasingly vital to the global energy transition, serving as essential tools for integrating renewable energy sources (RES) and ensuring grid stability. As renewables like wind and solar continue to gain prominence due to their sustainability and low environmental impact, their inherent intermittency poses a significant challenge for power systems. Energy storage addresses this issue by storing excess electricity generated during low-demand periods and releasing it when demand is high or generation is insufficient, thereby enhancing the flexibility and reliability of electricity networks.

From a market perspective, the global stationary energy storage market reflects this growing importance. In 2024, the market was valued at USD 53.84 billion, with projections indicating growth to USD 66.58 billion in 2025 and a staggering USD 450.52 billion by 2034. This represents a compound annual growth rate (CAGR) of 23.67% from 2025 to 2034, driven by increasing RES adoption and the demand for efficient energy storage solutions to support energy security and grid stability [2].

Academic research reinforces this trend. Elalfy et al. (2024) highlight that energy storage enhances power system reliability, supports voltage regulation, and facilitates higher penetration of renewables [3]. Technologies like lithium-ion batteries, pumped hydro, and flywheels are increasingly deployed due to their high efficiency and scalability. Meanwhile, Pamfile (2023) emphasizes energy storage's role in ensuring a stable electricity supply, especially in light of rising electricity demand, climate goals, and the challenges of intermittent RES generation [4].

Furthermore, energy storage is recognized for its transformative impact on power markets. According to Ölmez et al. (2024), ESS enables price stabilization, encourages investment in renewables, and provides critical ancillary services such as frequency regulation and peak

shaving. As storage acts both as a producer and consumer of electricity, it introduces new dynamics and actors in liberalized power markets [5].

ESS also supports grid stability through frequency regulation, voltage control, and congestion management. According to Masaud et al. (2010), ESS helps maintain continuous power flow during demand spikes or generator failures and ensures high-quality power delivery by correcting fluctuations like sags, swells, and harmonics [6]. Li and Deusen (2025) further note that these systems reduce power outages, enhance rural electrification, and contribute significantly to reducing greenhouse gas emissions [7].

From a market efficiency perspective, ESS enables energy arbitrage and participates in ancillary service markets, where it can absorb excess generation at low prices and discharge it when prices are high, smoothing volatility and enhancing the economic operation of the grid. The DOE's Energy Storage Grand Challenge Report (2020) projects that stationary ESS deployments (excluding pumped hydro) will exceed 300 GWh annually by 2030, illustrating their rapid emergence as a mainstream grid asset [8, 9].

In distribution networks, energy storage systems improve local reliability and reduce infrastructure costs. Optimization models, like those developed by Moghimian Hoosh et al. (2023), demonstrate that strategic siting and sizing of ESS can deliver significant grid benefits, including reduced system costs, improved voltage profiles, and better integration of distributed renewables like rooftop photovoltaics [10].

Together, these studies show that ESS is no longer a niche solution but a multi-functional, indispensable pillar of the future power system. It enables greater renewable penetration, stabilizes grid operations, supports competitive energy markets, and ultimately paves the way for a low-carbon, resilient energy landscape.

2.3 Existing Systems Study

2.3.1 Dry Gravity Energy Storage (GES) Systems

Dry GES systems offer a promising alternative to traditional pumped hydroelectricity storage (PHES), particularly in locations where geographical constraints limit PHES feasibility. Dry GES systems utilize the principle of gravitational potential energy by lifting and lowering a solid mass, converting surplus electrical energy into potential energy and back to electricity when needed. Several dry GES system types exist, each with distinct operational mechanisms and advantages:

2.3.1.1 Advanced Rail Energy Storage (ARES)

This system employs rail-mounted shuttles to transport concrete blocks uphill, utilizing surplus electricity to power the shuttles' traction motors. When energy demand arises, the blocks descend along a sloped track under gravity, driving a generator to produce electricity. ARES boasts a claimed roundtrip efficiency of 78-80% [11, 12], experiences minimal standby storage losses (no self-discharge) and has a projected lifespan of 40 years. Its primary

suitability lies in mountainous terrains, leveraging the natural slopes for energy storage and release [13, 14].

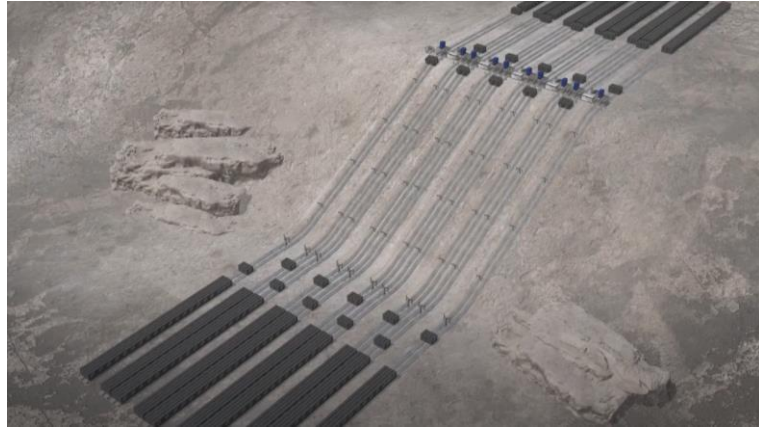


Figure 2.3.1 : ARES

An excellent example of ARES potential is found in West Virginia, where an analysis of the Mammoth Coal Processing Facility revealed an ideal site for implementation. This facility features a significant elevation difference—roughly 560 feet between a mountaintop mine and a lower processing plant—which enables efficient storage and energy generation. The proposed rail system would span approximately 1.5 miles with a slope of 4.5°, generating peak power levels upwards of 700 kW during discharge [12, 14].

2.3.1.2 Gravitricity

This system vertically lifts and lowers a heavy mass, potentially up to 3000 tons [11, 15, 16], within a deep shaft. The lifting mechanism relies on a network of guide cables, winches, and electric motors (Figure 2.3.2 : Gravitricity Mine Shaft). Existing mine shafts or purpose-built shafts up to 1500m deep can accommodate this system. Gravitricity claims an efficiency of 80-90%, a rapid response time of approximately 0.5 seconds, and a design life of 50 years [11]. The system offers flexibility in output duration, ranging from 15 minutes to 8 hours [17]. An innovative enhancement proposed by Gravitricity involves incorporating compressed air energy storage within the sealed shaft. This integration could potentially amplify the energy storage capacity by a factor of three [11, 18].



Figure 2.3.2 : Gravitricity Mine Shaft

2.3.1.3 Energy Vault

Energy Vault is a gravity energy storage technology that uses cranes to stack large composite bricks in a tower to store energy, which can be seen in Figure 2.3.3 : Energy Vault Storage Method [16, 19, 20]. When electricity demand is low, a crane uses surplus power from the grid to lift and stack the bricks. When electricity demand is high, the bricks are lowered, releasing kinetic energy, which is converted back to electricity. Energy Vault claims a cycle efficiency of between 80-90% over an 8–16-hour period [17, 21]. Energy Vault is best used for long-term energy storage applications in systems with relatively small energy storage demand. Energy Vault claims to have an LCOS of \$111/MWh [22]. It is a viable alternative to traditional pumped hydro storage in areas where suitable geography is not available and may be more cost-effective than battery storage for longer-duration applications [16, 23, 24].



Figure 2.3.3 : Energy Vault Storage Method

2.3.1.4 Lithium-Ion

Lithium-ion (Li-ion) batteries have emerged as a dominant force in stationary energy storage applications, attributed to their high specific energy (151-200 Wh/kg) and energy density (200-500 kWh/m³). This high energy capacity allows Li-ion batteries to store more energy per unit weight compared to other battery technologies, making them ideal for scenarios where space and weight are critical constraints. Particularly in urban settings, where space is at a premium, these batteries enable compact energy storage solutions [11, 25-27].

The efficiency of Li-ion batteries is another hallmark, with an average round-trip efficiency of 87.37%. Such high efficiency ensures that a significant portion of the stored energy is usable, minimizing energy loss during storage and retrieval processes. Furthermore, Li-ion batteries are known for their longevity, typically offering a service life of around 12.67 years and capable of enduring between 3000-7000 charge/discharge cycles at a maximum depth of discharge before reaching 80% of their original capacity. This durability makes them particularly suitable for energy storage systems where frequent cycling is expected and long-term reliability is paramount [11, 25-27].



Figure 2.3.4 Lithium-Ion BESS

Although the initial costs of Li-ion battery systems are higher, their long operational life and high efficiency provide a lower Levelized Cost of Energy (LCOE) of about 0.32 €/kWh. The operational costs are further mitigated by the low maintenance needs of Li-ion batteries, which not only reduce ongoing expenses but also enhance system reliability [26].

In summary, the attributes of Li-ion batteries—comprising high energy capacity, superior efficiency, prolonged lifespan, and economic viability—align well with the demands of modern stationary energy storage applications. As these batteries continue to decrease in cost and their technology advances, they stand out as a preferred choice for energy storage solutions, poised to meet the growing demands of both grid-connected and off-grid systems.

2.3.1.5 Flow Batteries

Flow batteries represent a unique class of electrochemical energy storage systems in which the electrolytes containing active chemical species are stored externally in liquid form and pumped through a cell stack during charge and discharge cycles. This design separates the power and energy capacities, allowing each to be independently scaled—making flow batteries especially well-suited for grid-scale storage with long-duration requirements.

Unlike conventional batteries (e.g., lead-acid or nickel-cadmium) where the electrochemical reactions occur directly on solid electrodes and limit storage capacity, flow batteries use dissolved species and membrane-separated compartments to enable high cycle life and continuous operation without significant degradation.

Common chemistries include:

- **Vanadium Redox (VRB)**
- **Zinc–Bromine (ZnBr)**
- **Sodium–Bromine (NaBr)**

The Regenesys Technologies system in the UK, initially developed in 2003, has a storage capacity of 15 MW / 120 MWh and an overall round-trip efficiency of approximately 75%. More recent designs are primarily based on vanadium-based systems due to their robustness and reversibility [28].

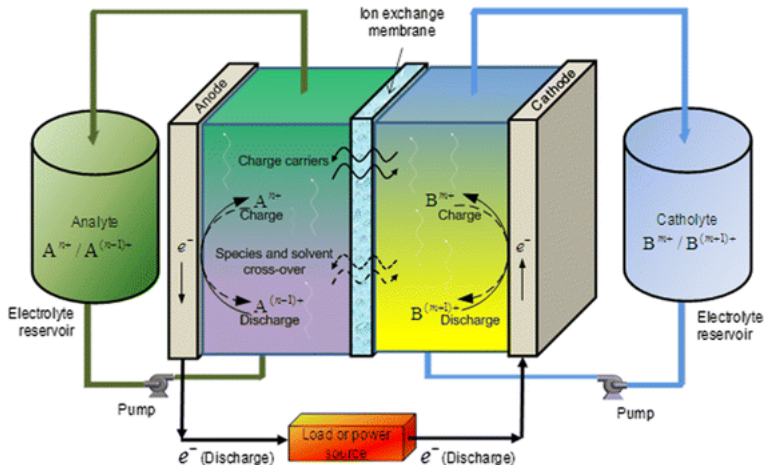


Figure 2.3.5 Flow battery operation [29]

VRFBs offer decoupled energy and power scaling, enabling independent adjustment of power output via stack size and energy capacity via electrolyte volume, ideal for long-duration storage. Scalability to megawatt levels is achieved through modular expansion. They demonstrate long cycle life, exceeding 10,000 cycles, due to minimal electrode wear, and utilize safe, non-flammable aqueous electrolytes. However, VRFBs exhibit lower energy density than lithium-ion, requiring larger installations, and present complex system designs with higher capital costs, particularly for smaller deployments, due to balance-of-system requirements.

2.3.1.6 Lead Acid

Lead-acid batteries have long been the cornerstone of stationary energy storage due to their reliability, low upfront costs, and established technology. These batteries typically feature a specific energy range of 20-50 Wh/kg and an energy density of 50-80 kWh/m³, which, while lower than that of newer technologies like lithium-ion, still suits many applications where high energy density is less critical. This makes lead-acid batteries especially viable for situations where budget constraints are significant, and space is not at a premium [25, 26].

Despite their lower energy density, lead-acid batteries maintain a respectable round-trip efficiency of approximately 76.36%. This efficiency, although not as high as that of lithium-ion batteries, allows for a reasonable return of stored energy for use. The lifespan of lead-acid batteries generally reaches up to 8.75 years with around 800 cycles at a maximum depth of discharge, indicating suitability for less demanding applications that do not require frequent cycling [27].



Figure 2.3.6 : Lead Acid Battery

The economic argument for lead-acid batteries is primarily driven by their low initial investment cost. While their operational and maintenance costs can be higher due to more frequent replacements and upkeep compared to lithium-ion batteries, their simplicity and low cost per unit of capacity continue to make them an attractive option for many stationary storage applications. The LCOE for systems using lead-acid batteries typically hovers around 0.34 €/kWh, slightly higher than for lithium-ion, reflecting the less efficient energy utilization and shorter lifecycle [25, 26].

Maintenance is an important consideration with lead-acid batteries, which require regular checks and servicing to ensure optimal performance and longevity. Their environmental impact is also notable; lead-acid batteries are categorized as having a high environmental impact due to the lead content and the acidity of the electrolyte, which require careful disposal and recycling strategies to mitigate adverse effects [27].

Moreover, lead-acid batteries benefit from a well-established recycling system. Over 90% of the material in lead-acid batteries can be recycled, which can help mitigate the environmental impact associated with their disposal. Despite their limitations in energy density and efficiency, lead-acid batteries remain a robust solution for energy storage needs where high capacity and frequent cycling are not critical. Their ability to provide reliable power at a low initial cost ensures that they remain a practical choice for many stationary applications, including backup power systems and load-levelling operations where long discharge times are not routinely required [27, 30].

As energy storage technology continues to evolve, the role of lead-acid batteries is increasingly focused on niche markets where their characteristics align with specific technical and financial requirements, maintaining their relevance in the global energy storage landscape.

2.3.1.7 Linear Electric Machine Gravity Energy Storage (LEM-GES)

Linear Electric Machine Gravity Energy Storage (LEM-GES) is a dry gravity energy storage system that harnesses the potential energy of solid masses moved vertically within a shaft using linear electric machines (LEMs). It operates by raising multiple piston-like masses up a shaft when excess electricity is available on the grid. This upward movement converts

electrical energy into potential energy stored within the elevated masses. As energy demand rises, the masses are lowered down the shaft under gravity. This downward motion drives the LEM in reverse, acting as a generator to produce electricity that is fed back to the grid through a power converter.

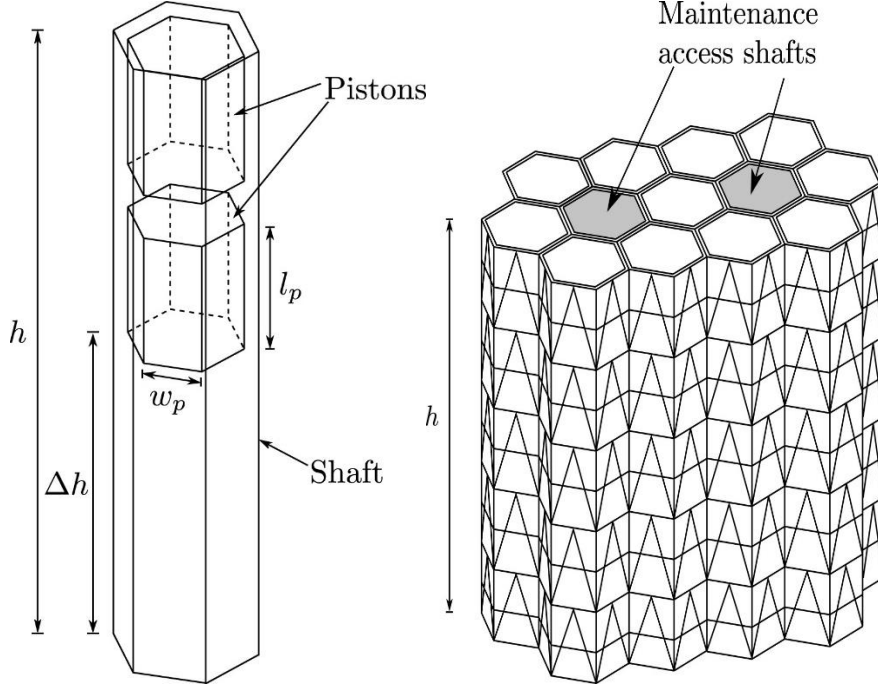


Figure 2.3.7 : Linear Electric Machine Concept

LEM-GES employs a direct-drive mechanism, eliminating gearboxes and ropes for simplified design and potentially enhanced efficiency. Its modular architecture allows for scalable energy capacity by increasing piston numbers or stacking shafts. LEM-GES offers geographical flexibility through above or below-ground implementation, including potential repurposing of existing mine shafts [11, 13, 16].

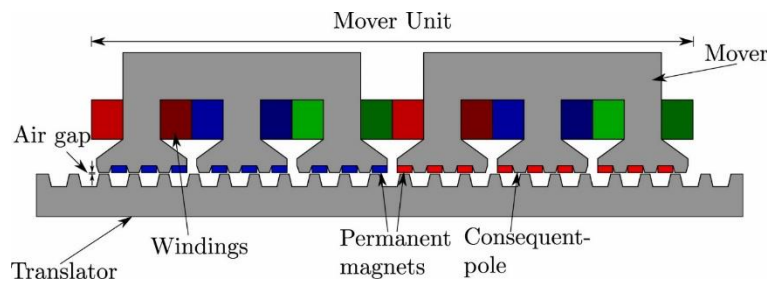


Figure 2.3.8 : LEM Operation

LEM Operation

Compared to traditional pumped hydro, LEM-GES can achieve higher energy and power densities for compact applications and rapid response. This technology is suited for primary grid response, energy arbitrage due to its high roundtrip efficiency (77–91%), and wind farm integration for smoothing power fluctuations [11, 13, 16, 31].

Key specifications include system heights of 100-1000 m, 1 mm air gaps, piston masses of 5,000-20,000 kg, and potential for 50-500 pistons, yielding individual mover power outputs

of 13.6–150 kW. Optimized round-trip efficiency is projected at 85–90%, with energy density estimated at 4–12 kWh/m³ and a 90% depth of discharge. Designed for a 20–40 year lifespan with frequent cycling, the levelized cost of storage is estimated at \$100–\$200 per kWh. LEM-GES presents a technically advanced gravity storage solution with high efficiency and modularity, particularly beneficial for renewable integration, urban storage, and repurposed mine infrastructure [11, 13, 16].

2.3.1.8 Viability of Dry Gravity Energy Storage Technologies

The analysis of various dry GES systems—comprising ARES, Energy Vault, and LEM-GES—reveals a compelling case for their integration into modern, decarbonized power systems. Compared to conventional electrochemical storage solutions such as lithium-ion, flow batteries, and lead-acid technologies, dry GES options offer several unique and advantageous characteristics.

Among the dry GES technologies, ARES exhibits significant scalability in both energy and power, with power ratings between 100–3000 MW and lifetimes exceeding 40 years. With a round-trip efficiency of 78–80%, minimal self-discharge, and a Levelized Cost of Storage (LCOS) between €100–200/MWh, it provides a strong balance of performance and economic viability for large-scale, terrain-suitable deployments.

Energy Vault, which utilizes crane-stacked composite blocks, maintains a high round-trip efficiency (~80%) and full depth-of-discharge (100%) with flexible discharge times ranging from 1 to 24 hours. Its LCOS of €111/MWh positions it competitively for long-duration storage. However, limitations in scalability and footprint may restrict its applicability to certain grid scenarios.

LEM-GES emerges as the most technologically promising dry gravity storage solution, combining very high cycle life, virtually zero self-discharge, and the potential for gigawatt-scale power ratings when deployed across multiple shafts. It offers tailored energy densities (0.115–1.89 kWh/m³) and efficiencies ranging from 77–91%, with a particularly strong showing in deeper systems (e.g., 91% for 1000 m shafts). The LCOS of €166.9/MWh, paired with its modular design and adaptability to urban, industrial, or repurposed mine environments, reinforces its long-term viability.

In contrast, lithium-ion batteries demonstrate high efficiency (85–90%) and energy density (94–300 Wh/kg), making them ideal for short-duration, high-density applications. However, their shorter lifespans (10–15 years) and higher LCOS (€200–400/MWh) reduce their appeal for long-duration bulk storage. Flow batteries offer improved cycle life and safety, but at the cost of lower energy density (10–70 Wh/kg) and modest efficiency (65–80%). Lead-acid batteries, while low-cost upfront, suffer from the lowest efficiency (~75%), shortest cycle life, and limited depth-of-discharge (~50%), making them increasingly outdated for large-scale applications.

In summary, dry gravity energy storage systems, especially **LEM-GES and ARES**, represent highly durable, efficient, and cost-effective options for grid-level energy storage in a

renewable-powered future. Their ability to provide long lifespans, low environmental impact, and scalable architecture places them at the forefront of next-generation energy infrastructure planning—particularly for locations where water-based PHES is infeasible or undesirable.

2.3.2 Wet GES Systems

Wet GES systems, commonly referred to as pumped hydroelectric energy storage (PHES), capitalize on the gravitational potential energy of water. These systems typically consist of two reservoirs at varying elevations, utilizing pumping to store and release energy by transferring water between them.

A diverse range of wet GES systems exists, each with unique characteristics. Among these, PHES stands out as the dominant technology, comprising over 95% of grid-connected energy storage devices worldwide due to its maturity and scalability [32].

To circumvent the geographical constraints of traditional PHES, innovative adaptations have been developed. Underground PHES (UPHES), for example, positions the lower reservoir underground, thereby minimizing the required land area while maintaining a significant vertical displacement. This approach is particularly well-suited for repurposing abandoned mining sites.

Another variant, piston-based PHES, leverages the combined power of water and pistons for energy storage and conversion. Water pressure elevates the pistons, storing potential energy. Conversely, the descent of these pistons drives an electric generator, transforming gravitational potential energy into electricity.

2.3.2.1 Traditional PHES

Traditional PHES represents the most mature and widely deployed form of grid-scale energy storage, accounting for over 95% of global bulk storage capacity [11, 32, 33]. The system operates by pumping water from a lower reservoir to an upper reservoir during periods of low electricity demand, storing energy in the form of potential energy. When energy is needed, water is released from the upper reservoir, flowing through turbines to generate electricity. Traditional PHES typically exhibits a roundtrip efficiency of 65-87% [11, 31, 33-35].

Parameter	Value/Range
Typical Plant Size	100–3000 MW
Round-Trip Efficiency	70–85% (some claim up to 87%)
Cycle Duration	Hours to seasonal
Storage Capacity	Tens of GWh (massive scale)
Typical Discharge Time	6–20 hours
Lifetime	>50 years

Capital Cost	€470–2170/kW (site-specific)
Depth of Discharge (DoD)	Up to 100% (fully reversible)
Global Installed Capacity	~130 GW (as of 2020)

Table 1 PHES Technical Specification

While highly efficient and proven, traditional PHES systems require specific geographical features, such as suitable valleys and water sources, limiting their applicability in certain regions. Traditional PES plants can quickly switch between pumping and generating modes, enabling them to provide ancillary services such as frequency regulation, voltage support, and black start capabilities, contributing to grid stability and reliability [33, 34]. Traditional PHES also plays a crucial role in integrating intermittent renewable energy sources, such as solar and wind power, into the grid by absorbing excess generation during periods of high renewable output and releasing stored energy when renewable generation is low [31, 34, 35].

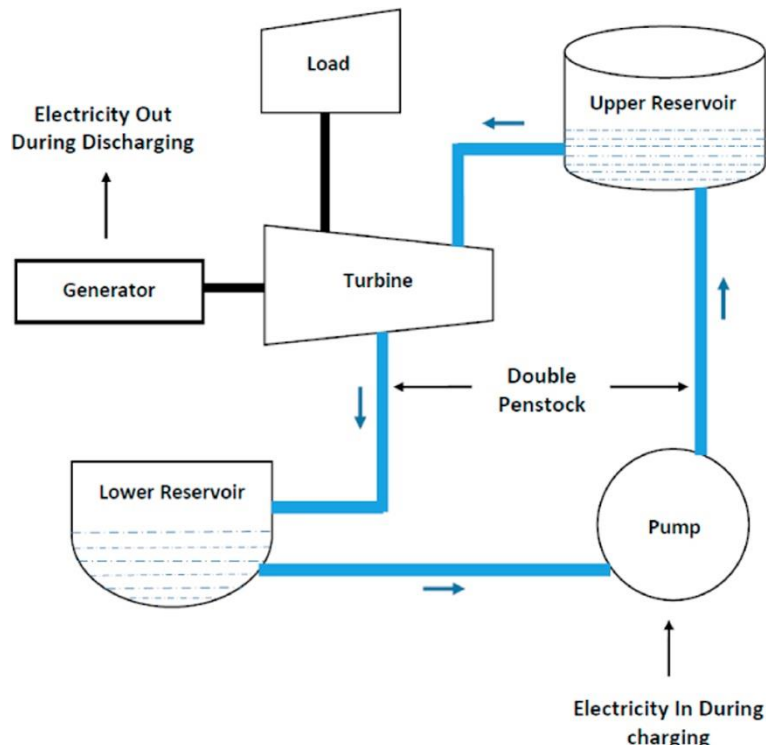


Figure 2.3.9 : Traditional PHES

However, in deregulated markets, PHES operators also face uncertainty in revenue due to volatile energy prices. As Pérez-Díaz et al. (2015) note, PHES operators increasingly participate in ancillary service markets to maintain profitability [36].

2.3.2.2 Underground Pumped Storage Hydropower (UPSH)

Underground Pumped Storage Hydropower (UPSH) is an innovative adaptation of conventional pumped hydro storage, designed specifically for geographies lacking natural elevation. Instead of relying on two surface reservoirs, UPSH systems use an upper surface reservoir and repurpose disused mining infrastructure—such as deep pits or coal mines—as

the underground lower reservoir. This configuration allows for energy storage deployment in flat terrains with minimal surface disruption, offering environmental and siting advantages over traditional PHES systems [34, 37-40].

Technical Characteristics and Operation

UPSH plants typically employ Francis pump turbines for medium-to-high head applications ranging from 100 to 1600 meters. CFD simulations and analytical modelling have demonstrated that such systems can deliver significant power output [37, 39, 40]:

- **Turbine 1:** 124.9 MW generation / 114.8 MW pumping input
- **Turbine 2:** 214.7 MW generation / 199.7 MW pumping input

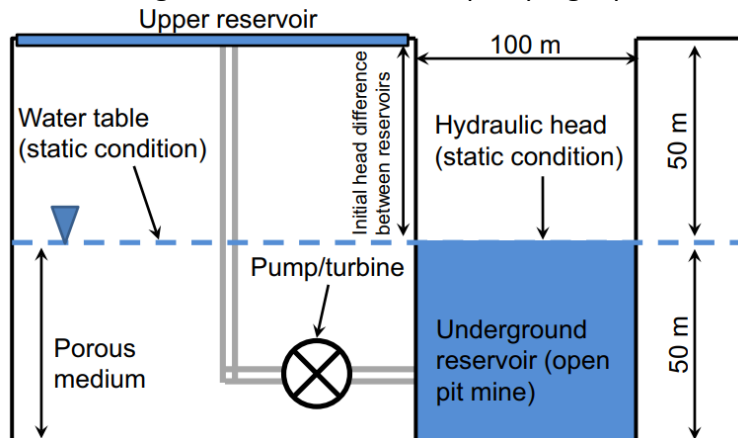


Figure 2.3.10 : Open Pit Mines

System performance is highly sensitive to the air pressure within the underground reservoir. At atmospheric pressure (0 kPa), round-trip efficiencies reach **77.3% for Turbine 1** and **75.8% for Turbine 2**. When pressure drops to -100 kPa, efficiency falls to **73.8%** and **72.7%**, respectively, due to increased flow resistance and compressibility losses in the air ducts.

For heads greater than **700 meters**, **Pelton turbines** are more appropriate due to their ability to handle high-pressure drops efficiently [37-40].

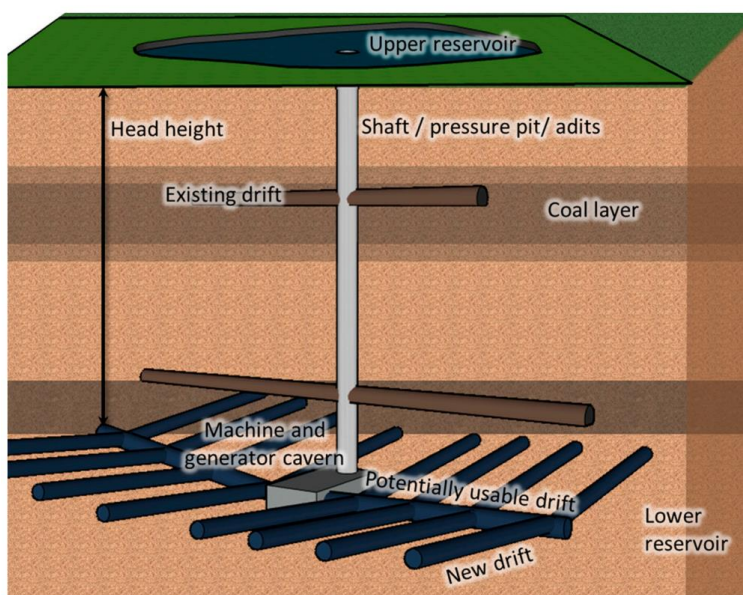


Figure 2.3.11 : Abandoned Coal Mines

Design Considerations

- **Reservoir Pressure:** Maintaining air pressure above **-50 kPa** prevents shock waves and unstable airflow patterns.
- **Air Duct Design:** A **minimum cross-sectional area of 0.4 m²** is recommended to avoid energy loss through compressible flow regimes.
- **Energy Density:** A 1 million m³ reservoir with a 1000 m head can store **~2589 MWh** of energy. Storage cost decreases from **€227/kWh at 500 m** to **€114/kWh at 1000 m**.

Additionally, groundwater interaction plays a role in system performance. High hydraulic conductivity (**10–100 m/d**) helps stabilize pressure differences between reservoirs, enhancing system stability. However, waterproofing the mine walls, while mitigating environmental risks, can constrain natural flow dynamics and increase design complexity [38-40].

Operational and Economic Challenges

UPSH systems must address several transient and economic challenges [37, 39, 40]:

- **Transient Stability:** Switching between pump and turbine modes causes mechanical stress, flow turbulence, and load variations, requiring advanced control strategies.
- **Efficiency Penalties:** At -100 kPa, Turbine 1 is projected to lose **966.9 MWh annually**, resulting in **~€401,000** in economic loss (assuming €70/MWh electricity value).
- **Capital Cost:** Estimated between **€114–253/kWh**, UPSH is competitive with compressed air storage but still higher than conventional surface PHES. However, utilizing brownfield sites (e.g., abandoned mines) can reduce infrastructure costs significantly.

Applications and Grid Role

UPSH systems offer long-duration storage (typically 5–8 hours at full load), ideal for renewable energy integration, frequency regulation, and peak load management. Their low land footprint, scalability, and ability to use pre-existing underground cavities make them particularly suitable for dense or topographically flat regions [34, 37-40].

2.3.3 Buoyancy Energy Storage Technology

Buoyancy Energy Storage Technology (BEST) is an innovative form of gravitational energy storage designed for deployment in deep ocean environments, especially suitable for islands, coastal regions, and offshore wind applications where traditional or dry gravity systems are impractical. It operates by lowering a buoyant compressed gas-filled storage unit (e.g., with hydrogen or air) to great ocean depths using surplus electricity. When energy is needed, the buoyancy recipient rises, driving a generator via a cable-pulley system to produce electricity [20, 41].

Power Rating and Energy Storage Capacity

A representative BEST system described in the study involves:

- **Installed power capacity:** 70 MW

- **Storage capacity:** 7.9 GWh (hydrogen-filled system at 10,000 m depth to 3,000 m)
- **Cycle duration:** Up to 8 days (0.01 m/s rise/fall speed)
- **Annual cycles:** 40 cycles per year
- **Round-trip efficiency:** 80–90%, depending on design specifics and gas used.

The energy storage capacity is strongly dependent on depth. Hydrogen-filled systems maintain a favourable buoyancy difference compared to seawater even at great depths, allowing higher energy recovery than air-filled equivalents (7.9 GWh vs. 4.6 GWh, respectively, for the same volume).

Cost and Economic Performance

- **Energy storage cost:** \$50–100 USD/kWh
- **Installed power cost:** \$4,000–8,000 USD/kW
- **Estimated project cost:** ~\$484 million for a 70 MW / 7.9 GWh system (6,000 m depth)
- **LCOS:** ~\$0.496/kWh
- **Hydrogen compression:** Up to 90% efficiency, compared to 40–50% for conventional compressors.

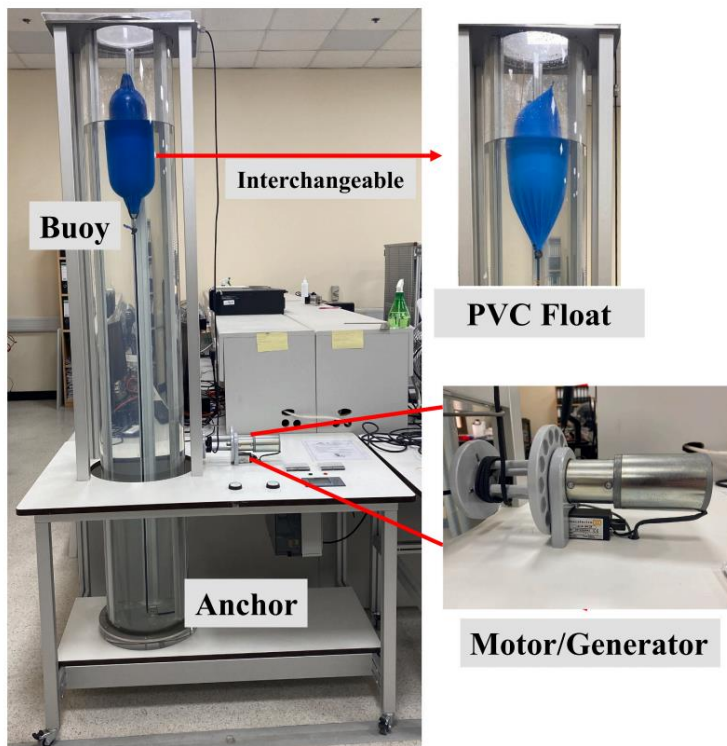


Figure 2.3.12 : Buoyancy Energy Storage Experimental Setup

Compared to other storage technologies, BEST features high storage capacity with low energy cost, but relatively high capital cost for power capacity due to deep-sea construction and long cable systems.

While not widely commercialized yet, BEST fills a gap between short-duration battery systems and seasonal PHES by enabling long-duration, mid-scale storage in marine settings.

Buoyancy Energy Storage Technology represents a promising new entrant in the gravity-based energy storage space. Its high efficiency, scalability, and unique geographic flexibility make it a strong candidate for supplementing renewable energy sources in marine and coastal regions. Although it is still in early stages of deployment, the technology's theoretical foundation and cost trajectory suggest significant long-term potential as part of a hybrid energy storage strategy when paired with faster-cycling systems like batteries.

2.3.4 Evaluating the Role of Wet Gravity Energy Storage (GES) Technologies

Wet gravity energy storage systems—commonly referred to as PHES—remain the most established, scalable, and widely deployed form of bulk energy storage worldwide. With over 95% of global grid-connected storage capacity, traditional PHES systems have long served as the backbone of grid balancing, renewable energy integration, and ancillary service provision.

Traditional PHES demonstrates exceptional durability, with lifespans exceeding 50 years, storage capacities in the tens of gigawatt-hours, and round-trip efficiencies ranging from 70–87%. However, despite these strengths, PHES is geographically constrained, requiring significant elevation changes and suitable terrain, which limits its feasibility in flat or densely populated regions. Additionally, capital costs vary significantly depending on location and infrastructure requirements (€470–2170/kW).

To address these limitations, two innovative adaptations—Underground PHES (UPSH) and BEST—have emerged as promising extensions of the wet gravity storage paradigm.

UPSH reimagines PHES for flat regions by repurposing abandoned mines or underground cavities as the lower reservoir. Systems modelled using Francis turbines have demonstrated power outputs of up to 215 MW, round-trip efficiencies of up to 77.3%, and competitive LCOS figures ranging from €114–253/kWh, particularly when brownfield infrastructure is reused. However, UPSH systems must address challenges such as transient pressure instabilities, air duct design, and annual efficiency penalties from pressure losses—factors which can incur up to €400,000/year in energy losses if poorly managed.

BEST, by contrast, shifts the gravity storage model into the marine environment, using buoyant compressed gas systems submerged at ocean depths (e.g., 3,000–10,000 m). This design enables energy storage in remote or offshore regions, especially suited to islands, coastal grids, or offshore wind farms. A single BEST installation could store up to 7.9 GWh, provide up to 70 MW of power, and operate over 8-day cycles. With round-trip efficiencies of 80–90% and very low energy cost (\$50–100/kWh), BEST offers great long-duration performance. However, it faces high capital costs for power capacity, long cable requirements, and technical complexity in deep-sea deployment.

Key Insights and Strategic Roles

Technology	Power Capacity	Efficiency	Cost (€/kWh)	Duration	Site Suitability
Traditional PHES	100–3000 MW	70–87%	€470–2170/kW	6–20 hrs to seasonal	Hilly/mountainous terrain
UPSH	125–215 MW	72–77%	€114–253/kWh	5–8 hours	Flat land / Abandoned mines
BEST	70 MW (modular)	80–90%	\$50–100/kWh (energy) \$4,000–8,000/kW (power)	Up to 8 days	Offshore / marine environments

Figure 2.3.13 : WGES Comparison

Wet gravity systems offer unique value in the medium- to long-duration storage spectrum, complementing fast-cycling battery systems and enabling a more flexible, resilient, and renewable grid. Traditional PHES remains indispensable where geography permits, while UPSH and BEST offer scalable, site-adaptable alternatives for the next generation of gravity-based storage infrastructure.

Together, these technologies form a **comprehensive wet GES toolkit**, extending the reach of pumped storage beyond its conventional boundaries and into a broader array of applications across the global energy transition.

2.3.5 Piston-Based GES

This category encompasses systems like the Gravity Power Module (GPM), Hydraulic Hydro Storage (HHS), and Ground-Breaking Energy Storage (GBES), which incorporate large pistons within water-filled shafts or excavated chambers. Energy storage occurs by pumping water into the shaft or chamber, raising the piston against gravity. Energy release involves allowing the piston to descend, pushing the pressurized water through turbines to generate electricity. Piston-based PHES systems offer an advantage over traditional PHES in terms of reduced geographical constraints, as they do not rely on natural reservoirs [11, 13, 23].

2.3.5.1 Gravity Power Module (GPM)

The GPM is a type of **piston-based** PHES system that utilizes a large, heavy piston suspended in a deep, water-filled shaft to store energy. Instead of using upper and lower reservoirs like traditional PHES, the GPM system relies on the controlled movement of this piston within the shaft to store and release energy [11, 17, 33, 42].

Operational Principle:

The GPM system comprises a deep shaft filled with water, a massive piston within the shaft, a return pipe connecting the bottom of the shaft to a pump-turbine unit at ground level, and a motor/generator connected to the pump turbine. The piston is typically designed as a series

of "pancakes" made from a combination of concrete and iron ore to achieve high density and low cost.

Charging (Energy Storage):

When there is excess electricity available, the motor drives the pump turbine, forcing water down the return pipe and into the bottom of the shaft. This increases the pressure at the bottom of the shaft, causing the piston to rise. As the piston moves upwards, the potential energy of the system increases, effectively storing the electrical energy used to pump the water.

Discharging (Energy Release):

To release the stored energy, the flow of water is reversed. The piston is allowed to descend, forcing the water back through the return pipe and through the pump turbine, which now acts as a turbine. This rotation drives the motor/generator, producing electricity that is fed back into the grid.

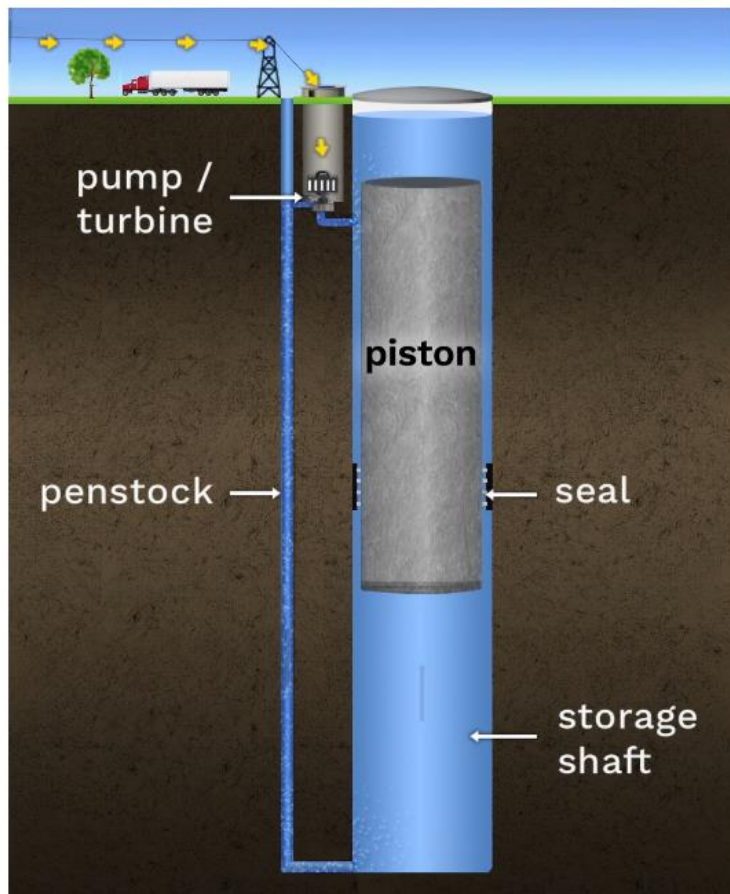


Figure 2.3.14 : Gravity Power Module

Key Features and Advantages:

High Efficiency: The GPM system boasts high efficiency due to minimal friction losses associated with the piston's movement and the inherently low losses of pump turbines.

Enclosed System: Once the shaft is filled with water at the beginning of operation, the system becomes sealed, and no additional water is required. This eliminates concerns about water loss through evaporation or leakage.

Flexible Siting: Unlike traditional PHES, which requires specific topographical features like valleys and mountains, GPM can be implemented in a wider range of locations, as long as suitable geological conditions exist for constructing the shaft.

Best Use Cases:

The GPM system is primarily designed for **grid-scale energy storage**, aiming to provide power and energy in the range of 40 MW/160 MWh to 1.6 GW/6.4 GWh [11, 17, 33, 42]. Its characteristics make it well-suited for:

Long-duration energy storage: GPM can store energy for extended periods, making it ideal for balancing intermittent renewable energy sources like solar and wind power.

Grid stability and reliability: GPM's fast response times enable it to provide ancillary services like frequency regulation and voltage support, enhancing grid stability.

Peak shaving and load shifting: GPM can store energy during periods of low demand and release it during peak hours, reducing peak load stress and improving grid efficiency.

Cost Considerations:

The economic viability of GPM depends heavily on the construction cost of the deep shaft. However, the sources suggest that the excavation costs for GPM are surprisingly low compared to some existing pumped storage hydro facilities, as the excavation can be automated.

Future Developments:

GPM technology is still under development, and ongoing research focuses on optimizing system design, exploring new materials for piston construction, and improving overall efficiency. As the technology matures and construction costs decline, GPM is poised to play a significant role in addressing the growing demand for grid-scale energy storage solutions.

2.3.5.2 HHS & GBES

Hydraulic Hydro Storage (HHS)

Hydraulic Hydro Storage (HHS) is a piston-based gravitational energy storage system designed for urban and flat terrains where traditional pumped hydro systems are not feasible. The concept, proposed by Eduard Heindl, involves using surplus renewable energy to **pump water beneath a massive cylindrical rock piston**, elevating it vertically. During discharge, the descending piston forces water through a turbine, generating electricity [13, 43, 44].

Technical Specifications (Based on a 50 m radius system):

- **Energy Density:** 11–18 kWh/m² depending on piston radius (scaling with r⁴)
- **Power Rating:** 28 MW pumping / 11 MW discharge for 50 m radius system
- **Discharge Duration:** 16 hours (typical night load supply)

- **Round-Trip Efficiency:** 80% (cycle-based)
- **Storage Capacity:** 198 MWh for a 50 m radius x 50 m height piston
- **Levelized Cost of Storage:** €150/kWh for a 50 m radius (excluding pump-turbine); decreasing to €51/kWh for an 80 m radius
- **Land Use:** Very compact – 11 kWh/m² energy density for a 40 m radius system
- **Lifetime:** Not explicitly stated, but inferred to be very long due to the use of rock and passive mechanical components

Construction Considerations: HHS systems can be constructed using open earthworks or mining techniques, depending on geology. A key engineering feature is the O-ring seal, which must remain below ground level but above the centre of gravity to maintain hydraulic stability. Sealing is done using geomembranes and stainless-steel panels.

HHS is particularly suited to **self-sufficient cities** aiming for energy autonomy through local storage of intermittent renewable energy. Its scalability and low land use requirements make it a strong candidate for integration into densely populated environments [13, 43-45].

Ground-Breaking Energy Storage (GBES)

GBES is a large-scale gravitational storage concept that uses an excavated rock piston suspended in a cylindrical cavity to store and discharge energy via hydraulic action. Unlike HHS, GBES is designed for very large utility-scale deployments and aims to compete with or surpass conventional PHES in both cost and performance [13, 44, 45].

Key Technical and Economic Features:

- **Power Rating:** 100 MW to several GW (e.g., 2 GW in base scenario)
- **Energy Capacity:** 20–40 GWh possible, depending on piston mass and lift height
- **Round-Trip Efficiency:** 80% (comparable or slightly better than PHES)
- **Discharge Time:** 20–40 hours standard, scalable to 100+ hours with minimal cost increase
- **LCOS:** Targeting **low tens of €/MWh**, enabled by high annual utilisation (up to 4000 hours/year)
- **Depth-of-Discharge:** 100% (hydraulic systems allow full cycling without degradation)
- **Cycle Life and Lifetime:** >10,000 cycles and 50+ years (same as PHES)

Design and Operational Highlights:

- GBES operates by raising a massive geological piston through water injection, storing gravitational potential energy.
- Discharge occurs by allowing the piston to descend, pushing water through turbines.
- The system is modular and site-flexible, suitable for flat, coastal, inland, or even underwater locations.
- It offers a much smaller land footprint than PHES and can double as flood control or water supply infrastructure in multi-purpose projects.

Market Viability and Challenges: The technology is still in the conceptual stage, requiring extensive proof-of-concept investment (est. >\$100 million). However, it shows high potential

for locations where PHES is infeasible, offering a low-impact, scalable solution for long-duration storage needed in **renewable-dominant grids**.

Parameter	HHS	GBES
Power Rating	3.6–184 MW (based on piston radius)	100 MW – multi-GW
Energy Storage Capacity	Up to 1.3 GWh (80 m radius)	20–40 GWh (base case), scalable to 100+ GWh
Round-Trip Efficiency	~80%	~80%
Discharge Time	8–16 hours	20–40+ hours
Energy Density	11–48 kWh/m ²	Very high (function of piston volume & lift)
Cost of Storage (€/kWh)	€51-149/kWh (larger is cheaper)	Lower than PHES; low tens of €/MWh (target)
Lifetime	Long (not limited by cycles)	>50 years
Depth-of-Discharge	100%	100%
Environmental Impact	Low, compact footprint	Very low; can be submerged or integrated
Construction Complexity	Medium – mining/earthworks	High – large-scale excavation and sealing

Table 2 HHS vs GBES

These technologies offer promising alternatives to conventional energy storage solutions, particularly in locations where mountainous terrain or large surface reservoirs are not feasible. While HHS is closer to realisation, GBES could reshape grid-scale storage economics if its large-scale deployment challenges are overcome.

2.3.5.3 Deep Ocean Gravity Energy Storage (DOGES)

Deep Ocean Gravity Energy Storage (DOGES) represents a novel concept in gravity-based energy storage that leverages the natural pressure differential and bathymetry of the deep ocean to achieve large-scale, long-duration seasonal energy storage. The system works by transporting high-density materials such as granite or mine waste between an upper storage site located at the edge of a continental shelf and a lower site situated several kilometres deeper on the ocean floor. During energy surplus, materials are transported upward, storing potential energy; during energy demand, they are lowered to generate electricity.

Technical Design and Operation

A typical DOGES plant, as proposed by Hunt et al., involves a closed-loop system comprising:

- Gravity generation ships at both shallow and deep sites,
- Cargo ships for lateral transportation,
- Container vessels attached to cables for vertical lifting and lowering,
- Underwater bucketwheel excavators, and
- Subsea transmission lines for power flow to shore.

Each container is $12 \times 6 \times 6$ metres with a volume of 438 m^3 . The system is capable of moving 350 million tonnes of material per year using 400,000 container movements. The lifting/lowering speed is optimised at 0.87 m/s, with negligible energy losses from hydrodynamic drag (drag force <0.4% of total weight) [13, 32, 34, 46].



Figure 2.3.15 : Deep Ocean Gravity Energy Storage Plan

The DOGES plant's performance is strongly influenced by storage depth:

- At 2000 m depth: 941 GWh capacity, 309 MW power
- At 4000 m depth: 1947 GWh capacity, 639 MW power
- At 6000 m depth: 2954 GWh capacity, 969 MW power

Each of these configurations assumes six months of continuous generation, translating into seasonal energy cycling with 40 full cycles per year [32, 46].

The system has an estimated round-trip efficiency of 60–70%, taking into account the energy used during cargo ship operation and energy recovery during descent. For instance, the efficiency of energy generation alone from the shallow gravity generation ship is 90%.

The levelized cost of energy storage is reported at approximately \$1.30 USD/kWh ($\approx \$1.21/\text{kWh}$), while the power cost is around \$3947 USD/kW ($\approx \$3683/\text{kW}$) at 4,000 m depth [32, 46].

Environmental and Logistical Considerations

DOGES offers unique advantages in terms of environmental footprint and location flexibility:

- Minimal landscape impact, unlike traditional hydro storage
- Reuse of mining waste as weight material
- No large reservoirs or significant land acquisition needed

The technology is particularly well-suited for island nations, coastal regions, offshore wind integration, and deep-sea mining operations. Its decoupling from terrestrial topography also provides energy storage potential in locations not suitable for traditional pumped hydro.

Parameter	Value / Range
Lifetime	Not specified; expected to be long due to low wear on components
Energy Density	~1947 GWh @ 350 Mt and 4000 m depth
Power Rating	309–969 MW depending on depth
Daily Self-Discharge (%)	Negligible
Discharge Duration	Seasonal (up to 6 months)
Levelized Cost of Storage	~€1.21/kWh
Cycles per Year	~40
Round-Trip Efficiency	60–70%
Depth-of-Discharge	100% (full material transfer)

Table 3 Key Parameters

DOGES offers an innovative, scalable solution for addressing long-duration, seasonal energy storage needs, especially where topographical or water constraints hinder conventional options. Though still in the conceptual stage, DOGES presents strong theoretical foundations and a compelling case for future deployment in the transition to a renewable-powered energy system. Its relatively low energy cost, minimal environmental impact, and synergy with maritime logistics make it a strong candidate for commercialisation with further development and investment.

2.3.6 Other Types of Energy Storage

2.3.6.1 Superconducting Magnetic Energy Storage (SMES)

Superconducting Magnetic Energy Storage (SMES) systems store energy in the magnetic field generated by a direct current circulating through a superconducting coil. Unlike electrochemical batteries, SMES stores electrical energy directly and can discharge and recharge almost instantaneously. This makes SMES highly suitable for grid support applications requiring very fast response times such as voltage regulation, frequency control, and mitigating power quality issues.

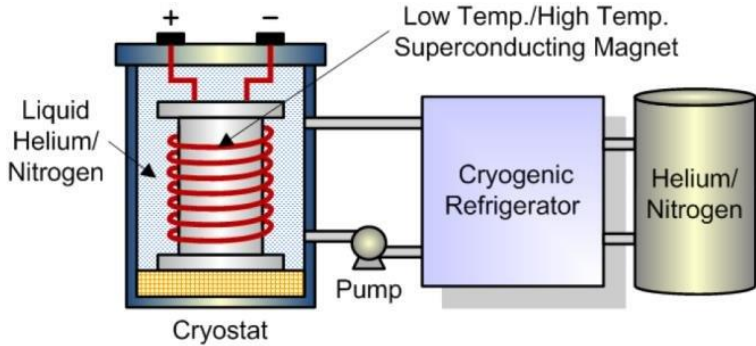


Figure 2.3.16 : SMES System Operation

Technical Specifications

- **Lifetime:** SMES systems typically exceed 20 years of operational life, supported by their minimal wear and tear due to the lack of electrochemical reactions [3].
- **Energy Density:** Energy densities range from 0.5–5 Wh/kg, which is comparatively low. This makes SMES better suited for short-duration, high-power applications rather than bulk energy storage [3, 33, 47].
- **Power Rating:** Commercial systems typically range from 100 kW to 10 MW. Experimental systems are being developed for power outputs of up to 30 MW [3, 6, 9].
- **Daily Self-Discharge:** One major limitation of SMES is its high self-discharge rate, between 10–40% per day, due to energy losses from persistent magnetic field maintenance even with superconducting materials [3, 48].
- **Discharge Time:** Discharge durations are typically in the range of milliseconds to a few seconds, although newer designs aim to extend this up to several minutes [3, 33, 48].
- **LCOS:** Although exact LCOS values vary widely, one source places the capital cost at €8974/kWh, making it one of the most expensive technologies for energy storage [3, 6, 47].
- **Cycles:** SMES systems have extraordinarily high cycle life, capable of over 20,000 cycles, which is ideal for continuous cycling in industrial settings [3, 9, 48].
- **Round-Trip Efficiency:** One of the highest among energy storage technologies, SMES typically achieves round-trip efficiencies above 97%, due to the absence of resistive losses in the superconducting coil [3, 6, 9, 33, 48].
- **DoD:** Since SMES does not suffer from electrochemical degradation, the DoD is effectively 100%, allowing the system to fully discharge without harming its longevity [35].

SMES systems, engineered for rapid energy delivery and grid integration, fundamentally consist of a superconducting coil (typically niobium-titanium), a cryogenic system maintaining ultra-low temperatures (e.g., 4.2 K with liquid helium), and a power conversion system. The superconducting coil, the energy storage core, is configured as either lower-cost solenoidal coils, which produce significant stray magnetic fields, or more complex and expensive toroidal coils, which emit minimal external fields, suiting magnetically sensitive environments.

While SMES offers unrivalled efficiency and cycle life, its current utility is limited to niche, high-frequency, high-power grid stabilization tasks due to its low energy density, short discharge durations, and very high capital cost, precluding its use in long-duration or bulk energy storage applications. Future advancements in superconducting materials and cryogenic technologies hold the potential to overcome cost barriers and expand the deployment scope of SMES in power systems.

2.3.7 Advantages and Disadvantages of Dry, Wet, and Piston-Based GES Systems

This literature review has examined various GES systems, highlighting their potential to address the growing need for large-scale energy storage solutions to support the transition to renewable energy sources. The analysed GES systems can be broadly categorized into dry GES, wet GES (also known as pumped hydroelectric energy storage, or PHES), and piston-based GES, a subset of both dry and wet systems. Each category presents distinct advantages and disadvantages, influencing their suitability for specific applications and geographical contexts.

Dry GES systems, which store energy by elevating a solid mass, offer several advantages:

- Reduced Geographical Constraints: Unlike traditional PHES, which relies on specific topographical features like valleys and water sources, dry GES systems can be implemented in a wider range of locations, including relatively flat terrain [11].
- Environmental Friendliness: Dry GES systems typically have minimal environmental impact, as they do not require large reservoirs or dams, reducing the potential for habitat disruption and water resource depletion [11, 17].
- High Efficiency and Durability: Many dry GES systems demonstrate high roundtrip efficiencies, exceeding 80% in some cases, and boast long lifespans, exceeding 40 years, with minimal self-discharge losses [11, 16].

However, dry GES systems also face challenges:

- Technological Maturity: Some dry GES technologies, such as LEM-GES, are still in the early stages of development, requiring further research and engineering advancements to achieve commercial viability [11, 16].
- Scalability: Scaling up dry GES systems to meet grid-level storage demands can be challenging, potentially requiring large land areas or significant infrastructure investments [11, 17].

Wet GES systems, or PHES, represent the most established form of large-scale energy storage, offering benefits such as:

- Proven Technology and High Efficiency: Traditional PHES boasts decades of operational experience and has demonstrated high roundtrip efficiencies, making it a reliable and efficient storage solution [33, 34].

- Large Storage Capacity: PHES plants can be constructed to accommodate vast amounts of energy storage, making them suitable for grid-level applications and supporting renewable energy integration [34].

Despite these strengths, wet GES systems face limitations:

- Strict Geographical Requirements: Traditional PHES necessitates specific topographical features, such as suitable valleys for reservoir construction, limiting their applicability in many regions.
- Environmental Concerns: The construction of large reservoirs and dams associated with traditional PHES can lead to significant environmental impacts, including habitat alteration, water flow disruption, and potential seismic risks [33, 34].

Piston-based GES systems, which can be either dry or wet, combine aspects of both categories, offering advantages such as:

- Reduced Geographical Dependence: Compared to traditional PHES, piston-based systems exhibit greater flexibility in siting, as they do not rely on natural reservoirs.
- Potential for Higher Efficiency: Certain piston-based systems, particularly those incorporating compressed air energy storage, can achieve high efficiencies exceeding those of traditional PHES [11, 13].

However, piston-based GES systems also encounter limitations:

- Complexity and Cost: The design and construction of piston-based systems can be complex and expensive, involving large-scale engineering projects and specialized equipment.
- Limited Operational Experience: While promising, piston-based GES systems, especially those utilizing large-scale pistons, have limited real-world deployment and require further testing and refinement to optimize their performance and reliability [11, 13, 23].

In conclusion, the optimal choice among dry, wet, and piston-based GES systems hinges on a careful evaluation of project-specific factors, including geographical suitability, desired storage capacity, environmental considerations, cost constraints, and technological maturity. As research and development efforts progress, and as the demand for large-scale energy storage intensifies, continued innovation and refinement of GES technologies across all three categories will be crucial to facilitate the successful integration of renewable energy sources and pave the way for a sustainable energy future.

2.4 Academic Research Papers

Recent research into energy storage technologies reflects the urgent need for robust, scalable, and efficient systems to support the transition to low-carbon power systems. The variability of renewable energy sources, the increasing electrification of demand, and the need for grid flexibility have led to the exploration of a broad range of storage technologies,

both established and emerging. This section synthesises findings from current literature and technical reports covering dry and wet gravity storage systems, electrochemical batteries, SMES, and novel concepts such as buoyancy-based and underwater ocean storage systems. The discussion centres around core performance parameters including efficiency, cost, scalability, lifetime, and environmental impact.

2.4.1 Dry Gravity Energy Storage Systems

Dry GES systems convert surplus electricity into potential energy by lifting heavy masses, which are later lowered to regenerate electricity. These systems are characterised by long lifespans, minimal environmental impact, and scalability for a range of applications.

Advanced Rail Energy Storage (ARES) uses electric locomotives to move heavy blocks uphill on tracks. Studies report round-trip efficiencies of 78–80% and service lifetimes exceeding 40 years. ARES is particularly effective in mountainous regions, where terrain can be naturally leveraged for storage operations.

Gravitricity employs vertical shafts to raise and lower weights of up to 3,000 tonnes. The system achieves rapid discharge response (<0.5 seconds), an efficiency of 80–90%, and can be co-located with decommissioned mine infrastructure. Cycles can range from 15 minutes to 8 hours, making it versatile for both frequency regulation and reserve power.

Energy Vault uses cranes to stack modular blocks, storing energy through gravitational elevation. Its round-trip efficiency is estimated between 80–90%, with discharge durations ranging from 1 to 24 hours. Energy Vault is suitable for long-duration, low-cycling applications, and benefits from modular deployment potential on flat terrain.

LEM-GES uses linear motors to move multiple pistons vertically in a shaft. Studies report energy densities up to 1.89 kWh/m³, high efficiencies of 77–91%, and full depth-of-discharge capabilities. LEM-GES is site-flexible and particularly well-suited to urban and industrial energy storage needs.

Piston-based Systems, including **HHS** and **GBES**, utilise pressurised water to raise rock pistons or geological masses. HHS offers a round-trip efficiency of 80%, with costs ranging from €51–150/kWh depending on system scale. GBES targets utility-scale storage with capacities of 20–40 GWh, 100% DoD, and projected costs in the low tens of €/MWh, comparable to pumped hydro.

2.4.2 Wet Gravity Energy Storage Systems

Wet gravity systems rely on the movement of water to store energy, often requiring elevation differences between two reservoirs.

Traditional PHES remains the most mature and widely deployed storage technology, accounting for over 95% of global installed capacity. It features power ratings between 100–3000 MW, round-trip efficiencies of 70–87%, and operational lifetimes exceeding 50 years. However, deployment is geographically constrained due to terrain and water availability requirements.

Underground PHES addresses these limitations by repurposing mine shafts or deep cavities as lower reservoirs. Simulated systems using Francis turbines have demonstrated efficiencies of 72.7–77.3%. UPSH is particularly effective for flat or densely populated areas and offers LCOS values between €114–253/kWh when brownfield sites are used.

Buoyancy Energy Storage Technology (BEST) stores energy by submerging gas-filled tanks in deep ocean waters. Hydrogen-filled tanks at 3,000–10,000 metres depth can provide storage capacities of 7.9 GWh and discharge durations up to 8 days. BEST systems offer high efficiency (80–90%) and low energy storage costs (\$50–100/kWh), though power costs are high due to marine infrastructure requirements.

Underwater Ocean Gravity Energy Storage (DOGES) moves dense materials vertically across deep ocean elevations. At 4000 m depth, DOGES can store nearly 2,000 GWh with power ratings over 600 MW. Although still conceptual, DOGES offers low environmental impact and a levelized cost of €1.21/kWh for energy, with seasonal discharge capabilities.

2.4.3 Electrochemical Energy Storage

Electrochemical storage technologies dominate short-duration, high-efficiency applications but differ significantly in cycle life, cost, and environmental footprint.

Lithium-Ion Batteries (Li-ion) are widely used due to their high energy density (94–300 Wh/kg), round-trip efficiencies of 85–90%, and lifespan of up to 15 years (3,000–7,000 cycles). Despite their widespread use, cost (LCOS of €200–400/MWh), degradation, and material sourcing remain concerns.

Lead-Acid Batteries offer low capital costs and high recyclability but are limited by low energy density (50–80 Wh/kg), modest efficiency (~76%), and short lifespans (~800 cycles, ~~9 years~~). ~~Their LCOS (€340/MWh)~~ is higher than that of Li-ion when total system costs are considered.

Flow Batteries, particularly vanadium redox systems, separate energy and power scaling, providing long-duration storage with efficiencies of 65–80%. Though energy-dense compared to lead-acid, they are bulkier than Li-ion and have LCOS values around €200–300/MWh.

2.4.4 Other and Emerging Technologies

Superconducting Magnetic Energy Storage (SMES) offers ultra-fast response times and extremely high efficiency (>97%), with unlimited cycle potential. However, its energy density is very low (0.5–5 Wh/kg), and capital costs are prohibitively high (~€8,974/kWh), limiting its use to power quality applications and niche markets.

Gravity Power Module (GPM) systems store energy by elevating large underground pistons. The system offers a long operational life (over 50 years), high round-trip efficiency, and levelized energy costs as low as €34/MWh—lower than lithium-ion storage. However, deep vertical shaft construction remains a barrier to adoption.

2.4.5 Comparative Insights and Research Gaps

The analysis reveals that no single energy storage technology meets all operational, economic, and environmental criteria. Instead, each technology fills a unique role in the evolving energy landscape:

- **Gravity-based storage systems** (dry and wet) offer long life, sustainability, and economic advantages in long-duration storage, particularly in regions with suitable topography or underground infrastructure.
- **Electrochemical systems** excel in short-term flexibility and urban settings but are constrained by degradation and material sustainability.
- **Emerging solutions** such as BEST, DOGES, GBES, and SMES expand the storage toolkit into marine and high-response grid services but require further technological development and cost reductions.

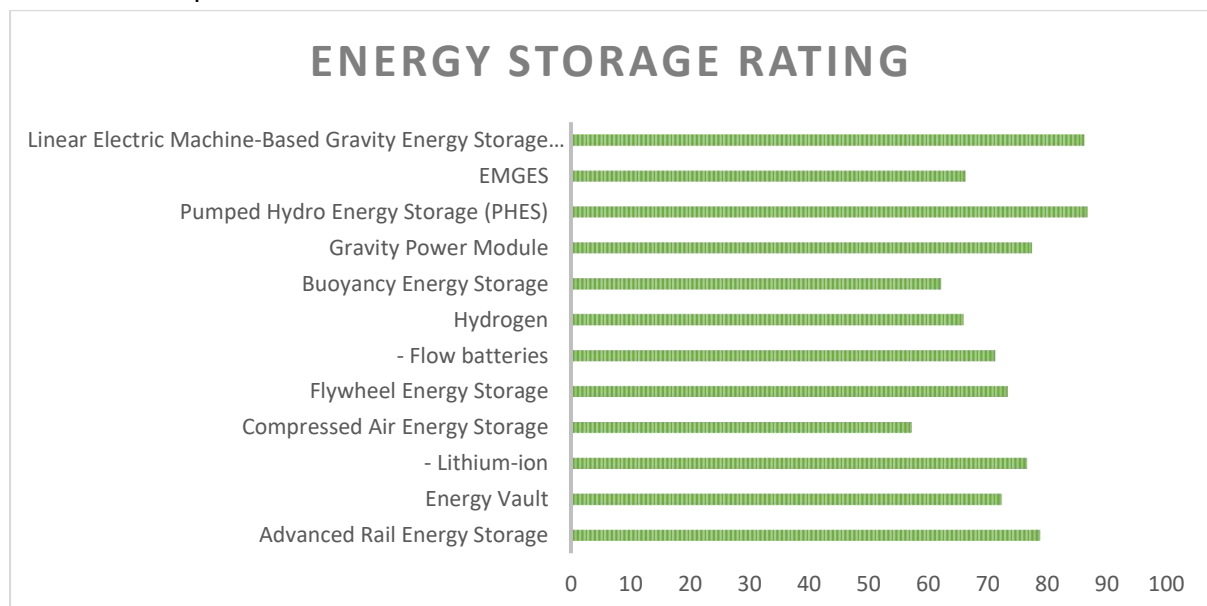


Figure 2.4.1 : Energy Storage Rating Comparison

Key research priorities include:

- Integrating hybrid systems that combine fast-response and long-duration technologies.
- Reducing the lifecycle costs and environmental footprint of emerging technologies.
- Conducting real-world pilot demonstrations of large-scale systems like GBES and DOGES.
- Advancing control systems to manage dynamic loads in multi-technology storage portfolios.

2.5 Gap Analysis

This section identifies and discusses the critical gaps in current gravity-based energy storage systems, highlighting areas where potential improvements could enhance their viability, scalability, and integration into modern energy systems.

Despite significant advances in energy storage technologies over the past two decades, a number of critical gaps remain that limit the universal deployment, economic viability, and operational effectiveness of storage solutions. These gaps are particularly evident when evaluating the diverse array of technologies discussed in this review, from mature systems like pumped hydro to emerging concepts such as LEM-GES and deep underwater gravity storage. This section identifies and discusses the key technical, economic, environmental, and infrastructural limitations of current energy storage solutions, highlighting areas that require targeted innovation and policy support.

2.5.1 Geographical and Infrastructure Limitations

Topographical Dependence: A significant limitation of several gravity-based systems, including PHES, ARES, and Gravitricity, is their reliance on specific geographic features. PHES, which currently dominates global storage capacity, requires significant elevation differences and access to large volumes of water. ARES depends on sloped terrain for track installation, while Gravitricity requires disused or purpose-built vertical mine shafts. These geographical constraints limit deployment flexibility and restrict these technologies to a narrow subset of suitable sites.

Infrastructure Barriers: Many storage technologies require extensive civil engineering works. Systems like LEM-GES and piston-based solutions (HHS and GBES) demand deep shaft construction, precision sealing, and heavy lifting systems. While theoretically scalable, these systems face high construction costs, long permitting timelines, and complex logistical challenges, particularly in urban or environmentally sensitive areas.

2.5.2 Environmental and Ecological Impact

Land Use and Visual Intrusion: Systems such as Energy Vault, which rely on large-scale structural installations, can result in substantial land use and visual disruption. This makes them less suitable for deployment near residential zones or in environmentally protected areas. In contrast, underground and ocean-based systems (e.g. UPSH, LEM-GES, BEST, and DOGES) offer lower surface impact but still involve significant environmental considerations during excavation or subsea deployment.

Resource and Material Intensity: Several gravity-based technologies require the movement or construction of large masses using concrete, steel, or rock. The environmental footprint associated with material extraction, transport, and system fabrication is often under-examined. This concern is particularly acute for lead-acid batteries, which involve hazardous materials and pose end-of-life recycling challenges, and Li-ion systems, which depend on rare and geopolitically sensitive minerals like lithium, cobalt, and nickel.

2.5.3 Economic Feasibility and Cost Efficiency

High Capital Expenditure (CAPEX): Technologies such as **PHES**, **LEM-GES**, and **BEST** require significant upfront investment due to infrastructure demands, marine engineering, or deep

shaft construction. This poses a barrier for widespread deployment, especially in developing regions or smaller energy markets.

Lifecycle Costs and Uncertainty: While some systems (e.g. **GPM** and **Li-ion**) may exhibit low levelized costs of energy (LCOE) over their operational lifespan, uncertainties around maintenance, replacement, degradation, and disposal often erode these benefits. For instance, **Li-ion systems** degrade with use and typically require battery replacement every 7–15 years, increasing total cost of ownership. **Lead-acid batteries**, though inexpensive upfront, exhibit short lifespans (~800 cycles) and high maintenance demands, making them unsuitable for frequent cycling applications.

2.5.4 Operational Flexibility and System Efficiency

Limited Discharge Flexibility: Systems like **PHES** and **Gravitricity** are efficient for full-load or continuous operation but less suited to variable or partial discharge, which is increasingly required in grids with high renewable penetration. Conversely, technologies such as **SMES** and **Li-ion** offer fine-tuned, rapid discharge, but may lack storage depth or duration.

Efficiency Losses in Emerging Systems: While systems such as LEM-GES and BEST claim efficiencies above 80%, newer or conceptual systems like DOGES still exhibit moderate round-trip efficiencies (60–70%) due to mechanical or hydrodynamic losses. These must be improved to ensure energy security and economic competitiveness in long-duration storage applications.

2.5.5 Scalability and Modularity

Challenges in Downscaling: Many gravity and hydro-based systems are inherently large-scale and difficult to downscale for modular or distributed use. PHES, GBES, and DOGES are designed for utility-scale operation and are not viable for community or residential-scale deployment. This presents a gap in the mid-range energy storage market, where flexible, modular, and compact systems are needed.

Technological Adaptability: While systems such as LEM-GES and flow batteries offer modularity in theory, practical deployment still requires bespoke engineering, which can be cost-prohibitive. Bridging the gap between standardised design and site-specific customisation remains a pressing challenge.

2.5.6 Technological Integration and Grid Compatibility

Grid Integration Barriers: Technologies such as SMES, flow batteries, and some gravity systems face challenges in real-time integration with variable renewables. This is especially critical in regions pursuing aggressive decarbonisation targets, where fluctuating solar and wind outputs require responsive and intelligent storage solutions.

Smart Grid Compatibility: The shift toward digitised and automated energy networks requires that storage systems include advanced control, sensing, and communication capabilities. However, many existing and emerging systems do not yet fully support real-time

data exchange or remote monitoring, limiting their participation in smart grid and virtual power plant frameworks.

2.5.7 Regulatory, Market, and Policy Gaps

Lack of Standardisation and Policy Support: Many emerging technologies lack established design standards, safety protocols, or policy incentives. This is particularly true for deep ocean systems (BEST, DOGES), underground gravity storage, and piston-based GES, which remain largely at the proof-of-concept or pilot stage.

Revenue Model Uncertainty: In liberalised electricity markets, storage technologies must compete not only on cost but also on revenue predictability. Market structures that reward frequency regulation or capacity services may favour certain technologies over others, skewing investment. This presents challenges for long-duration and seasonal storage systems that do not align with short-term pricing models.

2.5.8 Gap Analysis Conclusion

This gap analysis highlights that while significant progress has been made in energy storage system development, substantial challenges persist across technological, economic, and integration domains. Gravity-based storage systems offer long-term promise due to their longevity, environmental resilience, and cost trajectory. However, deployment limitations, infrastructure costs, and system rigidity remain key barriers.

Emerging concepts such as BEST, DOGES, and EMGES have the potential to overcome many of these limitations through modularity, environmental minimalism, and smart integration. Yet these systems require further development, demonstration, and regulatory support to transition from conceptual promise to market-ready solutions.

Ultimately, a diverse portfolio of storage technologies will be essential to meet the temporal, spatial, and economic demands of a decarbonised and decentralised energy future. Closing these identified gaps through research, innovation, and policy alignment will be critical to achieving global energy and climate goals.

2.6 Chapter summary

This chapter has reviewed a wide spectrum of existing and emerging energy storage technologies, evaluating their technical, economic, environmental, and operational characteristics. It has highlighted key trends in the development of gravity-based, electrochemical, and marine-based storage systems, while identifying significant gaps in areas such as modularity, scalability, site adaptability, and long-duration performance. A detailed gap analysis demonstrated that while many technologies serve specific market niches effectively, none fully address the combined need for cost-effective, high-efficiency, and flexible storage across diverse grid contexts. These insights form the basis for exploring new solutions that can overcome the limitations of current systems.

The next chapter presents the methodology used to investigate EMGES as a novel solution designed to address the gaps identified in the current energy storage landscape.

3 METHODS

3.1 Chapter overview

This chapter outlines the methodology employed to design, simulate, and evaluate the Electro-Magnetic Gravity Energy Storage System (EMGES) as a novel approach to renewable energy storage. It details the development of a small-scale prototype using electromagnetic coils and permanent magnets, with simulations conducted in Ansys Maxwell to optimise the system's storage and generation mechanics, complemented by LTSpice analysis of the power electronics. The chapter also describes the experimental testing of coil configurations to assess performance, alongside a simulated integration with solar photovoltaic systems to demonstrate energy flow management. Together, these methods provide a comprehensive framework for validating the technical feasibility and efficiency of EMGES under controlled conditions.

3.2 Principle of Operation and Background of EMGES

The Principle of Operation of the EMGES integrated with renewable energy sources illustrates the functional mechanism by which the system stores and retrieves energy. This description provides a clear understanding of the energy transformation processes involved and the technological innovations that underpin the system's operational efficiency.

3.2.1 Energy Storage and Generation

During periods of high solar irradiance or when wind speeds are optimal, excess electricity generated by these renewable sources is harnessed to power an electromagnetic lifting mechanism. This mechanism is central to converting the surplus electrical energy first into mechanical energy and subsequently into potential energy. The process involves the activation of electromagnets that generate a magnetic force potent enough to elevate a substantial weight. This weight, consisting of bronze and encased between two powerful neodymium magnets, is strategically positioned on the periphery of a cylindrical iron core. The ascent of the weight is meticulously regulated to control the speed and ensure that it reaches the top of the structure both safely and efficiently, where its potential energy is maximized.

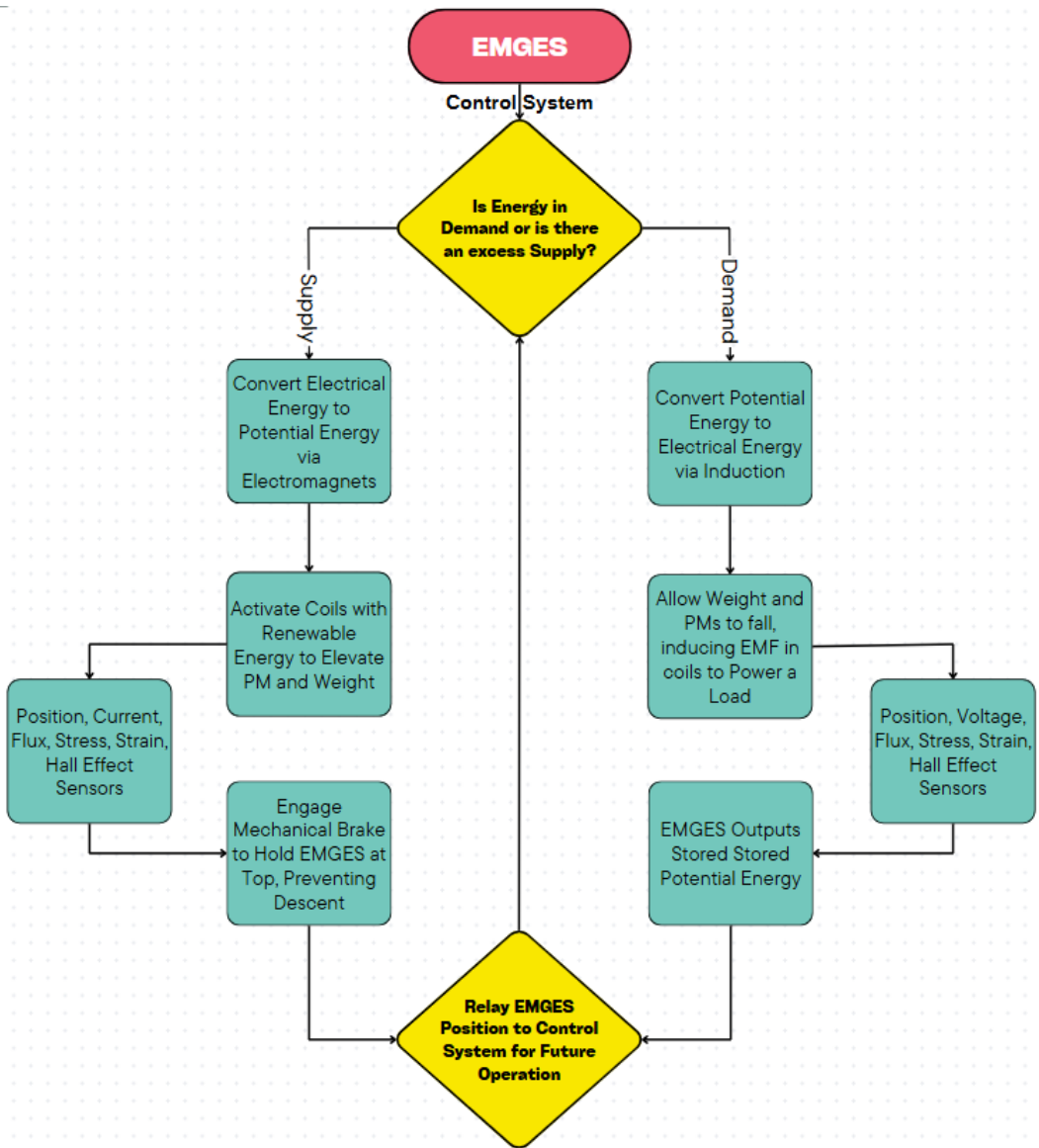


Figure 3.2.1 : EMGES Operation Flow chart

The release of energy is triggered when there is a peak in energy demand or a dip in renewable energy production, such as during night-time or on calm, windless days. The stored potential energy is then converted back into electrical energy through a carefully orchestrated process. The bronze weight is gradually lowered, moving through the magnetic field of the descending neodymium magnets. As it descends, it interacts with copper coils arrayed along the length of the iron core cylinder. This interaction induces a current in the coils through electromagnetic induction. The electric current generated in this manner is subsequently captured and converted into usable electrical energy, ready to be fed back into the grid or directed to where it is needed most.

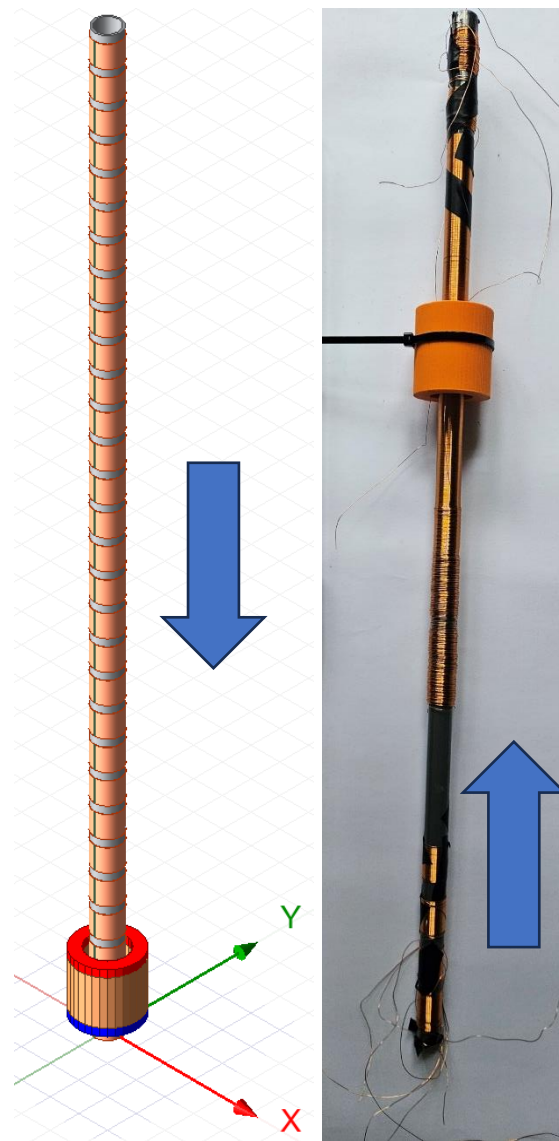


Figure 3.2.2 : Ansys Maxwell Design Setup fully Depleted from Generation Mode, Real Setup Operating in Storage Mode

This mechanism underscores the EMGES's capability to store energy efficiently and release it on demand, providing a reliable, sustainable solution that complements the intermittent nature of solar and wind energy sources. By leveraging the principles of electromagnetic induction and gravity, this system not only enhances the stability of the energy grid but also contributes significantly to the adoption of renewable energy technologies.

3.2.2 Operation Features

Regenerative Braking System

A key component of the EMGES is its regenerative braking system, which plays a dual role in enhancing energy capture efficiency and improving system safety. As the heavyweight descends, kinetic energy that would otherwise be lost as heat through conventional braking is instead captured. This process not only increases the overall energy efficiency of the system but also controls the descent speed of the weight. By modulating the speed at which the

weight falls, the system ensures a safer operation, particularly during periods of rapid energy discharge when the potential for mechanical stress is higher.

Magnetic Levitation

To further enhance the operational efficiency and durability of the EMGES, magnetic levitation technology is incorporated. This innovative feature reduces contact between the heavyweight and any physical guide structures, thereby minimizing friction and mechanical wear. Specifically, the heavyweight, encased between two powerful neodymium magnets, is levitated above the inner surface of the cylindrical iron core which is wrapped by copper coils. This levitation is crucial in extending the lifespan of the system by reducing the physical wear on the guide rails and the interior surfaces, ensuring that the system remains efficient and less prone to maintenance issues over long periods.

3.2.3 Grid Scale Smart Control System

While the primary focus of this project was on the design and validation of a scaled prototype, consideration was also given to control strategies suitable for full-scale deployment. A Grid-Scale Smart Control System (**SCS**) is envisioned as a vital enhancement for managing the EMGES in practical applications, particularly in optimizing energy efficiency, operational safety, and system longevity.

Prospective Sensor Integration

A full-scale SCS would incorporate a network of sensors designed to monitor critical parameters in real-time, feeding data into adaptive control algorithms. Although not implemented in the current prototype, the following sensor types are identified for future integration:

- **Position & Speed Monitoring:** Linear encoders and laser distance sensors for tracking the vertical displacement of the moving mass, along with tachometers for velocity feedback.
- **Magnetic Field Sensing:** Hall effect sensors or fluxgate magnetometers for assessing local magnetic flux density, helping to modulate electromagnetic forces dynamically.
- **Electrical Parameter Monitoring:** Ammeters and voltmeters to verify current and voltage levels across the electromagnets and power circuitry.
- **Thermal Management:** Thermocouples and infrared sensors to monitor the core, magnets, and coils, providing early warnings for thermal overload conditions.

Control Logic and Safety Framework

At the core of the SCS would be predictive and feedback-based control algorithms. These algorithms, informed by sensor data, would regulate the lifting and lowering cycles of the heavy mass based on grid demand, system status, and safety constraints. Key features include:

- **Real-Time Adaptive Control:** Dynamic modulation of the electromagnet actuation profile to align energy input/output with real-time grid requirements.

- **Predictive Maintenance:** Leveraging historical and live sensor data to anticipate failure points and schedule maintenance proactively.
- **Safety Protocols:** Automated shutdowns, emergency braking, and thermal regulation measures triggered by fault detection systems to ensure operational integrity.

Role in System Evolution

Although outside the scope of the present prototype testing, the SCS represents a critical step toward enabling EMGES deployment at a grid-relevant scale. Its integration would ensure precise motion control, protect key components from operational stress, and improve the system's responsiveness to fluctuating energy demands. As such, it is identified as a key area for future development in transitioning the EMGES from a conceptual prototype to a reliable, industrial-scale energy storage solution.

3.2.4 Proposed Integration Architecture and DC Power Compatibility

The grid-scale EMGES is conceptually designed to integrate with on-site renewable generation, particularly solar photovoltaic (PV) systems, using a DC-coupled architecture. This approach aims to enhance system efficiency, minimise conversion losses, and simplify control by leveraging the natural DC output of PV systems. At grid scale, this architecture is envisioned to support not only efficient energy storage but also real-time grid services such as frequency regulation and demand balancing.

DC Power Usage in Storage Mode

The EMGES relies on DC electricity during storage mode, wherein electrical energy is used to activate a linear electric machine operating in motor mode. This drives the upward movement of a heavy mass embedded with permanent magnets within a vertical shaft, converting electrical energy into gravitational potential energy. DC power is particularly well-suited for this application due to its ability to maintain a constant current, which is critical for generating a stable magnetic field required for precise and controlled lifting.

DC also enables simplified polarity reversal, allowing for directional control over the electromagnetic forces that raise or lower the mass. This facilitates fine-tuned system operation and improves the longevity of components by reducing electrical stress commonly associated with AC systems. Moreover, the simplicity of DC circuit design contributes to lower system complexity, increased reliability, and reduced maintenance.

AC Power Output in Generation Mode

During generation mode, the mass descends under gravity, and the linear electric machine acts as a generator. This motion produces **AC** electricity, which can be directly fed into the grid via a grid-tied inverter. The inverter plays a vital role in synchronising the generated AC output with grid voltage, frequency, and phase. In addition to frequency and phase matching, the inverter may also provide power quality management features such as voltage regulation and harmonic filtering, ensuring compatibility with grid standards.

Integration with Solar PV and Grid Interaction

A key advantage of the EMGES design lies in its seamless compatibility with DC-coupled solar PV systems. Because solar panels inherently generate DC electricity, their output can be directly utilised to power the EMGES in storage mode, bypassing intermediate conversions to AC and back to DC. This direct integration minimises conversion losses, maximising the utilisation of solar energy and enhancing the round-trip efficiency of the overall system.

In grid-connected applications, the EMGES system can act as both a controllable load and a dispatchable generator. When the grid is oversupplied with power (typically during times of low demand and high renewable generation), the EMGES can absorb energy from the grid, converting it into stored gravitational energy by raising the mass. Conversely, during periods of high demand or frequency dips, the EMGES can rapidly discharge by lowering the mass and injecting AC power into the grid. This bidirectional interaction makes EMGES particularly suitable for ancillary services such as frequency regulation, spinning reserve, and load following.

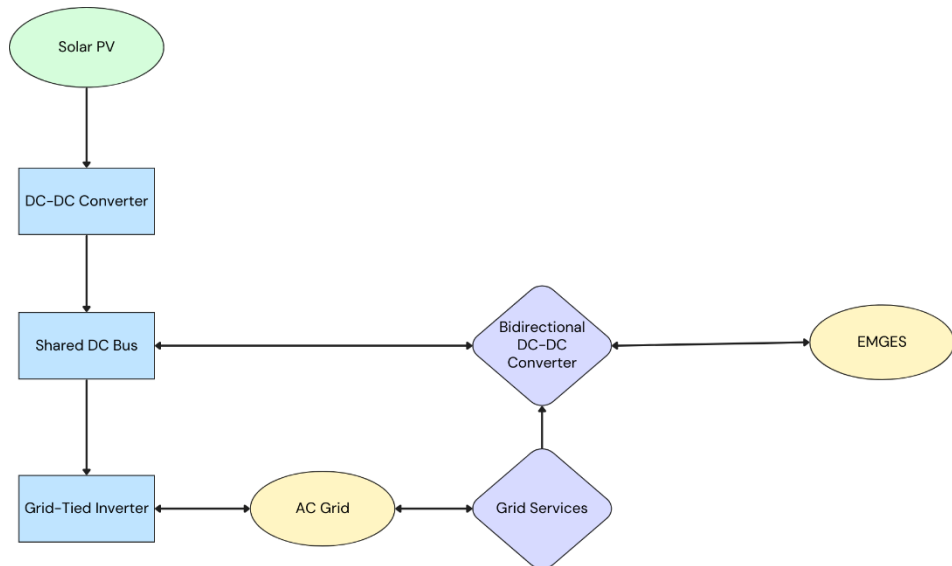


Figure 3.2.3 : Conceptual flow diagram of the proposed EMGES integration with a DC-coupled solar PV system and the AC grid

The proposed integration of the EMGES within a DC-coupled renewable generation framework offers significant technical and operational advantages. By drawing DC from solar PV in storage mode and delivering AC during generation, the system bridges the gap between modern renewable generation and traditional AC grid infrastructure. Its compatibility with DC power enhances system simplicity, efficiency, and responsiveness, while its AC output and smart control enable seamless grid participation. Though still in the conceptual stage, this integration model presents a promising pathway for flexible, scalable, and high-performance energy storage aligned with the needs of future power systems.

3.2.5 Frequency Regulation Capabilities

In AC power systems such as Ireland's 50 Hz grid, maintaining frequency within a narrow tolerance band is critical for grid stability and equipment safety. Deviations beyond $\pm 1\%$ —

specifically below 49.5 Hz or above 50.5 Hz—can lead to equipment malfunction, disconnection of generation assets, or even widespread blackouts. These imbalances often result from mismatches between supply and demand, which are becoming more common with the growing share of intermittent renewable generation.

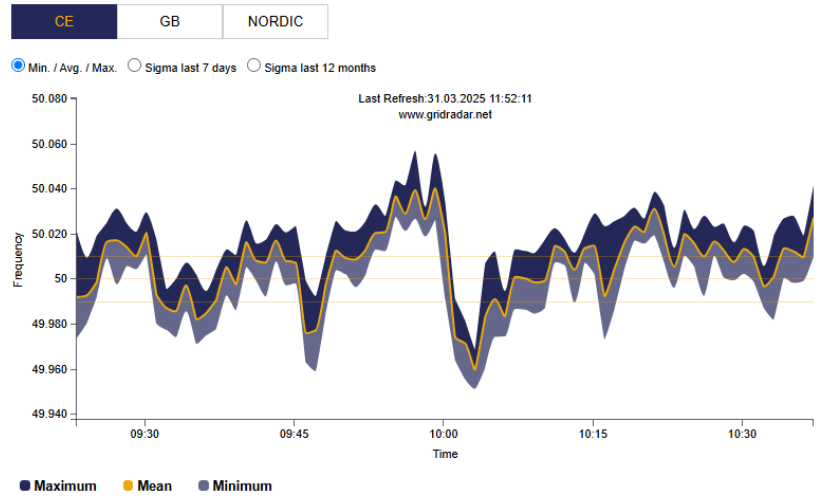


Figure 3.2.4 : Central European Live Grid [49]

The EMGES offers a fast, controllable means of frequency regulation by dynamically adjusting its power input or output in response to grid conditions. When the frequency drops (indicating a shortfall in supply), EMGES can immediately release power by lowering its internal mass and converting gravitational energy into electrical energy. When frequency rises (due to excess generation), the system can absorb surplus energy by using it to lift the mass, effectively acting as a controllable load.

This rapid response is enabled by the electromagnetic drive system, which allows fine control over the speed and direction of the mass movement. Combined with real-time frequency monitoring and inverter synchronisation, EMGES can provide sub-second adjustments to support grid frequency, acting similarly to traditional spinning reserve but without fuel or mechanical inertia.

In this way, EMGES provides a clean, efficient, and responsive solution to help maintain the grid within its safe operating frequency band—contributing to both system resilience and the reliable integration of renewable energy. Further work will focus on modelling and testing these capabilities under simulated and real grid conditions.

3.2.6 Conceptual Configuration for Modularity

The EMGES has been conceptually developed with a modular configuration at its core, not only across multiple units but also within a single vertical shaft. This inherent modularity enables flexible operation, system customisation, and optimised utilisation of vertical space in large-scale installations.

Electrical Modularity: Series and Parallel Configurations

Each EMGES unit can operate independently or in coordination with other units through configurable electrical arrangements:

- **Series Configuration:** When connected in series, the voltages of multiple EMGES units add together, while the current remains constant. For example, four units each generating 5 V could produce a total of 20 V when combined in series. This configuration is useful where higher voltage is needed, such as for interfacing with centralised inverters or medium-voltage DC buses.
- **Parallel Configuration:** When connected in parallel, the currents of the EMGES units combine, while the voltage remains the same. For instance, four units supplying 2 A each would provide a total of 8 A. This is advantageous when higher current capacity is required, such as in low-voltage, high-power applications or where redundancy is essential.

These configurations enable tailored system design based on specific voltage or current requirements, and are capable of dynamically adjusting interconnections in response to load profiles or generation targets.

Mechanical Modularity Within a Single Shaft

A unique advantage of the EMGES concept is the ability to operate multiple independent masses within the same shaft, made possible by its ropeless, linear motor design. This allows for separate weights—each capable of moving independently—to be actuated or discharged based on real-time energy requirements. The primary constraint is vertical space management, as multiple masses cannot occupy the same maximum height simultaneously. Instead, each must be allocated a specific vertical range, which reduces the maximum stroke length per mass but increases the flexibility and responsiveness of the system as a whole.

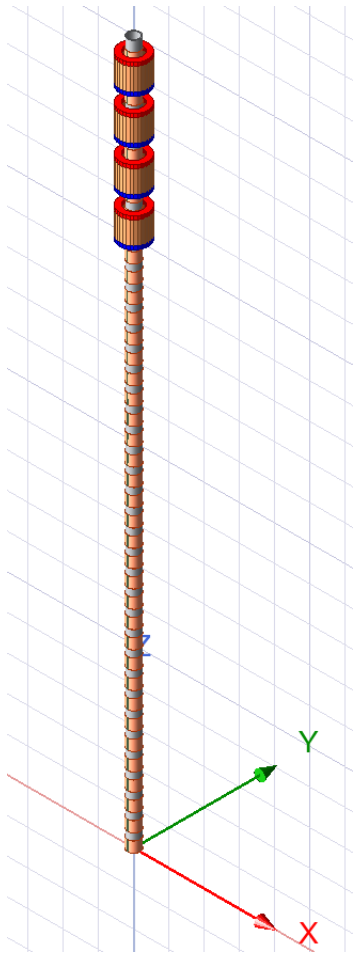


Figure 3.2.5 : Multiple PMs and Mass Configuration for Increased Energy Capacity

This feature introduces granular control over power output, enabling partial discharge, fast ramp-up, and simultaneous multi-level operation, all from a single shaft structure. It is especially beneficial for grid-scale systems where power demand can fluctuate rapidly and where full discharge of the entire stored mass may not always be required.

Comparison to Existing Technologies

This modular, multi-mass approach represents a notable advancement over existing gravity storage technologies such as Gravitricity, which rely on traditional hoisting mechanisms and are thus limited to operating a single suspended mass per shaft. In such systems, introducing additional masses would require separate shafts or complex mechanical interventions. The ropeless nature of EMGES, using linear electromagnetic drives, eliminates these constraints and allows for independent vertical positioning and movement, offering a higher degree of functional flexibility.

This architectural difference addresses a current gap in the gravity energy storage market—namely, the lack of systems capable of multi-mass, variable-output operation within a compact footprint. EMGES provides a conceptual solution to this problem by enabling stacked, decoupled energy storage and generation events, which enhances both energy density and dispatch control.

The modularity of EMGES extends beyond scalable unit deployment to include intelligent multi-mass operation within a single shaft, setting it apart from traditional gravity energy storage designs. This enables finely tuned power delivery, optimised use of shaft infrastructure, and a greater range of control over discharge profiles—features that support the dynamic needs of modern power systems. By addressing current mechanical and operational limitations found in competing technologies, EMGES introduces a promising advancement in the evolution of gravity-based energy storage.

3.3 Fundamental Principles and Governing Equations

The EMGES operates at the intersection of electromagnetic theory, classical mechanics, and energy conversion principles. This section rigorously defines the theoretical foundations governing its operation, with emphasis on electromagnetic induction, magnetic flux linkage, reluctance, and force generation. The equations presented in this sub-chapter are either directly sourced from or derived based on the principles outlined in the following references: [50-64]

The EMGES relies on **Faraday's Law of Induction** and **Lenz's Law** to convert mechanical energy into electrical energy during the discharge phase3.3.1.

Faraday's Law of Induction (Integral form):

$$E = \oint_{\partial\Sigma} E \cdot dl = -\frac{d}{dt} \int_{\Sigma} B \cdot dA \quad 3.3.1$$

Where E is the electric field, B is the magnetic flux density, and Σ is any surface bounded by the loop $\partial\Sigma$.

Faraday's Law (Coil):

The electromotive force (EMF) induced in a coil is proportional to the rate of change of magnetic flux linkage:

$$\varepsilon = -N \frac{d\phi}{dt} = -N \frac{d\phi}{dx} v \quad 3.3.2$$

where N is the number of coil turns, and ϕ is the magnetic flux (Weber, Wb). The negative sign reflects Lenz's Law.

Lenz's Law:

The induced current in a conductor due to a changing magnetic field will flow in a direction that **opposes the change in magnetic flux** that produced it.

Magnetic Flux

The flux ϕ through a coil is defined as:

$$\phi = \int_S B \cdot dA \quad 3.3.3$$

For uniform fields and perpendicular alignment:

$$\phi = BA \cos(\theta) \quad 3.3.4$$

Where B is magnetic flux density (Tesla, T),
 A is the cross-sectional area (m^2),
 θ is the angle between B and the normal to A .

Magnetic Field Generation (Biot-Savart and Coil Expressions)

Biot-Savart Law

The magnetic flux density B generated by a current-carrying conductor is given by the Biot-Savart Law General Statement:

$$B = \frac{\mu}{4\pi} \int \frac{I dl \times \hat{r}}{r^2} \quad 3.3.5$$

Where:

I = current (A)

dl = infinitesimal length of the conductor (m)

\hat{r} = unit vector from the conductor to the observation point

r = distance from the conductor to the point (m)

$\mu = \mu_0 \mu_r$ is the material's permeability (H/m),

$\mu_0 = 4\pi \times 10^{-7} \text{ H/m}$,

μ_r is relative permeability of the material.

For a circular coil of radius R with N turns, the axial magnetic field at distance z from the centre is:

$$B_z = \frac{\mu N I R^2}{2 \sqrt[3]{(R^2 + z^2)}} \quad 3.3.6$$

Where z is the vertical distance from the centre of the coil to a point of interest along its central axis.

Solenoid field with a core (Approx):

$$B = \mu_0 \mu_r \frac{NI}{L} \quad 3.3.7$$

Finite Solenoid (Approx):

$$B = \mu_0 \mu_r \frac{NI}{\sqrt{L^2 + R^2}} \quad 3.3.8$$

Combined formula for exact Magnetic Flux Density:

$$B_{exact} = \frac{\mu NI}{2L} \left[\frac{\frac{L}{2} + z}{\sqrt{R^2 + \left(\frac{L}{2} - z\right)^2}} + \frac{\frac{L}{2} - z}{\sqrt{R^2 + \left(\frac{L}{2} - z\right)^2}} \right] \quad 3.3.9$$

Where L is the total axial length of the solenoid

3.3.1.1 Force Generation

General Force Formula (For a Permanent Magnet and Ferromagnetic Material)

The force F at a distance z is derived from the energy gradient of the magnetic field:

$$F(z) = \frac{\partial}{\partial z} \left(\frac{B^2(z)A}{2\mu_0} \right) \quad 3.3.10$$

Where:

- $B(z)$ = Magnetic flux density at distance z (Tesla).

Magnet Force on Magnets or Ferromagnetic materials

$$F \approx \frac{B^2 A}{2\mu_0} \quad 3.3.11$$

Larger surface area = Stronger force (for a given B).

If B^2 is fixed, which is it for most magnets, the force of attraction is proportional to the surface area of the magnet ($F \propto A$).

Axial force between two identical cylindrical PMs

$$F = \left(\frac{\pi}{2}\right) B_r^2 R^4 \left[\frac{1}{z^2} - \frac{1}{(z+t)^2} \right] \quad 3.3.12$$

Where

R = radius

B_r = remanent flux density

t = thickness

z = distance of separation

The Lorentz force and Maxwell's stress tensor govern the electromagnetic forces acting on the PM.

1. Lorentz Force:

The force on a current-carrying conductor in a magnetic field:

$$F = I \int dl \times B \quad 3.3.13$$

Magnetic Circuits and Reluctance

The interaction between the PM and coils is modelled using magnetic circuit theory, analogous to electric circuits.

Magnetic Field Intensity (H)

Linear Material:

$$B = \mu_0 \mu_r H \quad 3.3.14$$

Magnetized Medium (PM):

$$B = \mu_0 (H + M) \quad 3.3.15$$

Reluctance (\mathcal{R}):

The opposition to magnetic flux in a material is quantified as:

$$\mathcal{R} = \frac{l}{\mu_0 \mu_r A} \quad 3.3.16$$

Where:

l is the magnetic path length (m),

1. Ohm's Law for Magnetic Circuits:

$$\phi = \frac{\mathcal{F}}{\mathcal{R}} \quad 3.3.17$$

where \mathcal{F} is the magnetomotive force (MMF, ampere-turns). For a permanent magnet, $\mathcal{F}_{PM} = H_c \cdot l_m$, where H_c is coercivity (A/m) and l_m is magnet length (m). For coils, $\mathcal{F}_{coil} = NI$.

Composite Magnetic Circuit:

The total MMF driving flux through the PM and coils is:

$$\mathcal{F}_{total} = \mathcal{F}_{PM} + \mathcal{F}_{coil} = H_c l_m + NI \quad 3.3.18$$

The flux ϕ is shared across reluctances of the PM (\mathcal{R}_m) and air gap (\mathcal{R}_g):

$$\phi = \frac{\mathcal{F}_{total}}{\mathcal{R}_m + \mathcal{R}_g} \quad 3.3.19$$

Magnetic Moment of an Axially Magnetized Ring Magnet

The magnetic moment m of the ring magnet is:

$$m = M \cdot V \cdot \hat{z} \quad 3.3.20$$

Where:

M = magnetization (A/m) of the magnet material (e.g., neodymium: $M \approx 1 \times 10^6$ A/m),

V = volume of the ring (m^3)

3.4 Prototype Component Options and Selection

The EMGES utilizes a series of engineered components, each chosen to meet specific performance, efficiency, and durability requirements. The selection of these components is integral to the overall functionality and success of the system. This section outlines the criteria used to select key components within the EMGES, ensuring each part aligns with the system's objectives to provide reliable, efficient, and sustainable energy storage solutions.

Key considerations in the selection process include the materials' physical and chemical properties, cost-effectiveness, availability, environmental impact, and compatibility with other system components. Each choice is backed by rigorous analysis and calculations to verify that it meets the operational demands of the EMGES. These criteria help in optimizing the design for both performance and scalability, making it viable for a range of applications from industrial to residential energy storage.

3.4.1 Core Material Options

The choice of core material in the EMGES is pivotal due to its central role in facilitating efficient magnetic flux conduction and energy conversion. The core's material properties directly influence the system's overall performance, particularly its energy efficiency, operational reliability, and durability. This section evaluates potential core materials, primarily focusing on their electrical and magnetic properties to determine the most suitable option for the EMGES.

Two primary materials considered for the core are **iron** and **silicon steel**. Each material offers distinct advantages and is evaluated based on criteria such as magnetic permeability, saturation magnetization, electrical resistivity, and overall impact on the system's magnetic reluctance.

Iron:

- **Magnetic Permeability:** Iron has high magnetic permeability, which facilitates a significant enhancement in the magnetic flux density within the core. This property is crucial for achieving efficient magnetic field interaction with the surrounding copper coils.
- **Saturation Magnetization:** Iron can handle relatively high magnetic flux densities before reaching saturation. This characteristic is vital for ensuring that the core does not become a limiting factor in the system's performance under high operational demands.
- **Electrical Resistivity:** Pure iron has a relatively low resistivity, which can lead to higher eddy current losses. These losses are detrimental as they reduce overall energy efficiency and can cause overheating issues.

Silicon Steel:

- **Magnetic Permeability:** Silicon steel also exhibits high magnetic permeability but with better control over eddy currents due to its increased electrical resistivity.
- **Saturation Magnetization:** Similar to iron, silicon steel supports high levels of magnetic flux but generally offers better performance in avoiding saturation under equivalent conditions.
- **Electrical Resistivity:** The addition of silicon improves the resistivity of the steel, significantly reducing eddy current losses compared to pure iron. This reduction is crucial for enhancing the efficiency of energy conversion processes within the EMGES.

Reluctance and Efficiency:

- **Reluctance:** The reluctance of the core material is a central factor that influences the efficiency of the magnetic circuit (3.3.16). Lower reluctance in the core material facilitates easier magnetic flux flow, which is essential for efficient operation. Silicon steel, with its superior properties for controlling eddy currents, presents lower effective reluctance compared to iron.

- **Efficiency:** The efficiency of magnetic energy conversion is directly impacted by how well the core material handles magnetic flux without significant losses. Silicon steel, due to its higher resistivity and reduced eddy current formation, offers higher overall efficiency in energy conversion processes.

Property	Pure Iron	Silicon Steel
Magnetic Permeability	Higher	High
Saturation Magnetization	Higher	High
Electrical Resistivity	Low (→ more eddy losses)	High (→ fewer eddy losses)
Eddy Current Losses	Higher	Lower
Thermal Stability	Moderate	High
Mechanical Strength	Moderate	High
Cost	Low	Higher

Table 4 Iron v Silicon Steel Comparison

Thermal and Mechanical Properties: Both materials need to withstand operational stresses without significant deformation or loss of magnetic properties. Silicon steel's alloy composition provides enhanced thermal stability and mechanical strength, making it more suitable for applications where the core might experience fluctuating temperatures and mechanical loads.

Cost Considerations: While silicon steel is generally more expensive than pure iron due to its alloying elements and manufacturing processes, the long-term benefits of reduced energy losses and lower maintenance requirements can offset the initial higher cost.

After evaluating both iron and silicon steel, silicon steel emerges as the superior choice for the core material in the EMGES due to its lower reluctance, higher efficiency in managing eddy currents, and better thermal and mechanical properties. These advantages make it particularly suitable for enhancing the overall performance and reliability of the EMGES, ensuring that the system can operate efficiently and sustainably under varying load conditions and over extended periods.

3.4.2 Copper Coils

The selection of copper coils for the EMGES is governed by a set of critical criteria that ensure optimal performance, efficiency, and durability of the energy storage process. Copper coils play a pivotal role in the electromagnetic function of the EMGES, where their main task is to convert the kinetic energy of a descending weight into electrical energy through electromagnetic induction.

Material Conductivity and Efficiency: Copper is chosen primarily for its high electrical conductivity, which is second only to silver among commercial metals. This high conductivity ensures minimal energy loss in the form of heat, thus maximizing the efficiency of the energy conversion process.

AWG	OD (mm)	CSA (mm ²)	Resistance (W/km)	Normal Current (A)	Maximum Current (A)
16	1.29	1.318	13.5	5.161	5.885
17	1.15	1.026	16.3	4.104	4.68
18	1.02	0.8107	21.4	3.248	3.704
19	0.912	0.5667	26.9	2.578	2.939
20	0.813	0.5189	33.9	2.048	2.335
21	0.724	0.4116	42.7	1.625	1.852
22	0.643	0.3247	54.3	1.28	1.46
23	0.574	0.2588	48.5	1.022	1.165
24	0.511	0.2047	89.4	0.808	0.921
25	0.44	0.1624	79.6	0.641	0.731
26	0.404	0.1281	143	0.506	0.577
27	0.361	0.1021	128	0.403	0.46
28	0.32	0.0804	227	0.318	0.362
29	0.287	0.0647	289	0.255	0.291
30	0.254	0.0507	361	0.2	0.228
31	0.226	0.0401	321	0.158	0.181

Table 5 AWG Comparison [65]

Thermal Considerations: Copper's excellent thermal conductivity also plays a crucial role in managing the heat generated during operation. The ability to dissipate heat efficiently is pivotal in preventing overheating and potential damage to the coils and surrounding components, especially under high current loads.

Mechanical Properties: The mechanical strength and flexibility of copper allow for the coils to be wound tightly around the core without the risk of breaking. This is essential for creating compact, efficient magnetic circuits within the EMGES structure.

Cost and Availability: While copper is more expensive than some alternatives like aluminium, its superior electrical properties and availability justify its cost. The long-term reliability and efficiency gains from using copper significantly offset the initial higher material cost.

Environmental and Durability Factors: Copper coils are resistant to corrosion, which is a crucial consideration given the potential exposure to harsh environments within an EMGES. Moreover, copper's durability under mechanical and thermal stress ensures a long service life, reducing the need for frequent replacements and maintenance.

Calculations and Considerations

The design and specification of copper coils involve detailed calculations to ensure that they meet the required electrical characteristics for efficient energy conversion. These calculations

include determining the wire gauge, number of turns, coil resistance, and inductance, which directly impact the voltage induced in the coils by the moving magnetic field.

- **Wire Gauge:** The gauge of the wire affects both the total resistance and the physical size of the coils. Thicker wires (lower gauge numbers) have lower resistance but occupy more space, which may not be optimal for the design constraints of the EMGES.
- **Number of Turns:** The number of turns in the coil directly affects the magnitude of the induced voltage. More turns typically result in higher voltage but also increase the resistance and inductive reactance, which can influence the coil's performance at different frequencies.
- **Coil Resistance and Inductance:** These parameters are crucial for designing the coil to match the system's operational frequency and power requirements. They are determined based on the wire type, diameter, number of turns, and the core material around which the coil is wound.

The selection of copper coils for the EMGES is based on a careful balance of electrical, thermal, mechanical, and cost considerations. Their critical role in the energy conversion process, coupled with their influence on the system's overall efficiency and reliability, underscores the importance of meticulous planning and calculation in their design. The chosen coil parameters ensure that the EMGES can operate efficiently and reliably, providing a scalable solution to energy storage challenges.

3.4.3 Neodymium Magnets

The selection of Neodymium magnets for the EMGES is a vital process that hinges on their magnetic properties, shapes, magnetization orientation, and compatibility with the system's design and operational requirements. Neodymium magnets, known for their superior magnetic strength among rare earth magnets, are essential for the EMGES due to their role in the energy conversion mechanism involving magnetic induction.

Magnetic Properties

Neodymium magnets are selected for their high magnetic field strength and energy product, which enable efficient and effective conversion of mechanical energy into electrical energy through the process of electromagnetic induction. The key magnetic properties considered include:

- **Remanence (B_r):** This is the residual magnetism of the magnet, which dictates the strength of the magnetic field in absence of an external magnetic force. Higher remanence enhances the magnet's ability to induce a strong magnetic field necessary for optimal coil interaction.
- **Coercivity (H_{ci}):** The resistance to demagnetization is crucial for maintaining magnet performance under varying thermal and mechanical stress conditions within the EMGES.

Shape and Magnetization Orientation

The shape of the magnet affects the distribution of the magnetic field and its interaction with copper coils. The selection process involves considering various shapes (e.g., disc, ring, or block) to optimize the flux path and maximize the efficiency of the electromagnetic induction process:

- **Ring Magnets:** Often preferred for their ability to provide a uniform magnetic field that is ideal for coaxial alignment with cylindrical copper coils.
- **Magnetization Direction:** Axially magnetized magnets are typically chosen to align the magnetic poles along the axis of movement, which is critical for maximizing the interaction with the coil's magnetic field.



Figure 3.4.1 : Possible Magnet Shapes [66]

Strength and Grade

The grade of the Neodymium magnet indicates the maximum energy product (BH_{max}) the magnet can support. Higher grades (for example, N42 compared to N35, or N52 compared to N42) typically exhibit stronger pull forces for the same physical dimensions, although they may be more expensive or increasingly sensitive to heat. Temperature ratings—denoted by suffixes such as “H,” “SH,” or “UH”—further distinguish magnets capable of sustaining higher operating temperatures without performance loss. When selecting a magnet grade for the EMGES, therefore, it is necessary to balance the need for a robust magnetic field (to drive sufficient electromagnetic induction) with considerations of cost, availability, and temperature tolerance.

Durability and Corrosion Resistance

Neodymium magnets are prone to corrosion when exposed to environmental elements such as moisture and chemicals. Therefore, the selection includes considerations for protective coatings (such as nickel plating) that enhance durability and reduce the risk of degradation over time.

Cost and Availability

While Neodymium magnets are more expensive than other magnetic materials like ferrite, their superior magnetic properties justify the cost in applications like the EMGES where high performance is essential. The availability of different grades and custom shapes also plays a

role in the selection process, ensuring that the magnets can be sourced reliably and efficiently.

Environmental Impact

The production of Neodymium magnets involves rare earth elements, which have significant environmental implications due to mining and processing. The selection process thus also considers the environmental policies of the magnet suppliers and opportunities to minimize the ecological footprint through responsible sourcing practices.

In summary, the selection of Neodymium magnets for the EMGES is a multifaceted process that balances magnetic performance with physical and environmental considerations. The ultimate goal is to ensure that the magnets contribute effectively to the system's overall efficiency, durability, and operational reliability.

3.4.4 Selection of Weights

The selection of appropriate weights for the EMGES is pivotal to its functional efficacy, particularly in converting gravitational potential energy into kinetic energy. For a proof-of-concept demonstration that necessitates a compact and efficient design, the material, shape, and properties of the weight are selected with meticulous consideration. This subsection explores the criteria used to select suitable materials for the weights, highlighting why materials like tungsten, brass, and bronze are preferable for small-scale, high-density applications.

Material Density and Efficiency

The primary criterion for selecting a weight material is its density. Higher density materials allow for more energy to be stored in a smaller volume, enhancing the system's overall efficiency by maximizing the gravitational potential energy per unit volume.

- **Tungsten:** Known for its exceptionally high density (about 19.25 g/cm^3), tungsten is an excellent material for weights in EMGES applications. Its high density enables the storage of substantial energy even in smaller weights, making it ideal for compact systems.
- **Brass and Bronze:** While not as dense as tungsten (brass approx. 8.73 g/cm^3 and bronze approx. 8.9 g/cm^3), offer a good balance of density, machinability, and cost. These materials are easier to work with compared to tungsten and provide sufficient density for effective energy storage and conversion in a proof-of-concept model.



Figure 3.4.2 : Bronze Weight

Shape and Compatibility

The shape of the weight is designed to optimize the gravitational force and ensure smooth operation within the EMGES's mechanical structure.

- **Cylindrical or Disc Shapes:** These shapes are commonly used as they facilitate easy vertical movement and can be efficiently integrated with the guide mechanisms and magnetic levitation systems of the EMGES.

Magnetization Properties

For weights that interact with magnetic fields, such as in systems where magnetic levitation or guidance is employed, the magnetic properties of the weight material are also considered.

- **Non-magnetic Materials:** Materials like tungsten, brass, and bronze are typically non-magnetic, which prevents interference with the magnetic fields generated by the neodymium magnets used for levitation and energy conversion.

Cost and Availability

Cost is a crucial factor, especially for prototype and proof-of-concept systems where budget constraints are often more stringent.

- **Cost-Effectiveness:** Brass and bronze offer a cost-effective alternative to tungsten, providing a reasonable compromise between density and expense. These materials are widely available and can be sourced economically, making them suitable for initial experimental setups.

Alternative Materials

Other materials like wet sand or water have also been considered for their simplicity and low cost.

- **Wet Sand:** Offers variable density and is easy to shape but lacks the mechanical stability and consistency needed for precise energy storage applications.
- **Water:** Commonly used in large-scale pumped hydro storage but is less suitable for small-scale applications due to its low density and the complexity of containerizing it effectively in a small system.

The selection of weights for the EMGES involves a comprehensive evaluation of material properties, cost, environmental impact, and compatibility with the system's design. Tungsten, brass, and bronze emerge as leading choices for a small-scale proof-of-concept system due to their density, machinability, and minimal impact on the system's magnetic fields, providing an efficient and practical solution for demonstrating the EMGES's capabilities.

3.4.5 PVC Plastic Housing/Guide Rails

The selection of appropriate housing and guide rails is crucial for the functionality and durability of the System EMGES. This subsystem not only protects the core components but also ensures smooth and efficient operation of the moving parts. PVC plastic has been identified as a suitable material for both housing and guide rails, due to its advantageous properties and performance in similar applications.

PVC Plastic Characteristics

- **Durability:** Polyvinyl Chloride (PVC) is renowned for its strength and durability, making it resistant to environmental factors such as moisture, corrosion, and chemical erosion. These properties ensure the long-term integrity of the housing and guide rails, protecting the internal components of the EMGES.
- **Insulation:** PVC provides great electrical insulation. This characteristic is crucial for preventing electrical hazards, especially considering the proximity of the guide rails to the electromagnetic components of the system.
- **Low Cost:** PVC is relatively inexpensive compared to metals and other polymers, which makes it an economical choice for large-scale applications or prototypes where cost containment is essential.
- **Ease of Fabrication:** PVC can be easily machined and moulded into complex shapes, allowing for the precise geometries required for guide rails and housings in the EMGES.

Shape and Configuration

The design of the guide rails and housing must accommodate the movement of the weighted assembly with minimal friction and resistance. The shape of the PVC components is optimized to ensure smooth operation, integrating features that support the magnetic levitation and alignment of the moving weights.

Compatibility with System Dynamics

PVC's non-magnetic nature ensures that there is no unwanted magnetic interference with the system's operation, particularly the function of neodymium magnets and electromagnetic coils.

Environmental and Operational Advantages

Thermal Stability:

PVC possesses good thermal stability, which is essential for maintaining structural integrity under the varying temperatures that the system might encounter during operation.

Chemical Resistance

The chemical inertness of PVC is beneficial in environments where corrosive substances might be present, ensuring that the housing and guide rails do not degrade or emit harmful substances over time.

Pros and Cons of Alternative Materials

Metallic Alternatives

- **Pros:** Higher mechanical strength and potential for better precision in manufacturing.
- **Cons:** Higher cost, susceptibility to corrosion, heavier weight, and potential magnetic interference with system components.

Composite Materials

- **Pros:** Can be engineered to specific properties, potentially offering better performance in certain parameters such as strength-to-weight ratio.
- **Cons:** Generally more expensive than PVC, more complex to manufacture, and may require more sophisticated maintenance.

Wood and Other Polymers

- **Pros:** Lower cost and easy to work with.
- **Cons:** Lower durability, potential for moisture absorption, and less predictable performance under mechanical stress and environmental exposure.

The selection of PVC for the housing and guide rails in the EMGES is justified based on its mechanical properties, cost-effectiveness, chemical and thermal resistance, and ease of fabrication. These characteristics make PVC an ideal choice for ensuring the protection and smooth operation of the system, while also aligning with budgetary and performance objectives. This analysis demonstrates a careful consideration of various material options, with PVC emerging as the most suitable given the specific requirements and constraints of the EMGES.

3.5 Electromagnetic Prototype Design

In order to thoroughly investigate the electromagnetic interactions underpinning the prototype's performance, Ansys Maxwell was employed as the principal finite element analysis (FEA) tool. This software package provided critical insights into the distribution of magnetic flux, the resulting forces on the moving components, and the overall system response under various operating conditions. By comparing results from theoretical calculations, Ansys Maxwell simulations, and the subsequent experimental measurements, it

was possible to validate assumptions made during the design phase and refine the system's geometry, material selection, and energisation strategy. The following subsections detail the FEA setup, key flux distribution findings, iterative refinements based on individual component tests, and the overarching validation of analytical models at the system level.

3.5.1 Component Testing

Individual Component Testing, e.g. iron core, coil, coil with core, coil AWG

During the initial phase of this project, Ansys Maxwell (Student Version) was utilised to perform finite element analyses on individual components of the proposed electromagnetic-gravity apparatus. Although the student edition allowed basic setup and visualisation of magnetic fields, it came with inherent limitations—most notably in element size, mesh refinement, and solver capabilities. As a result, a 28-day trial of the full Ansys Maxwell suite was subsequently employed for more complex simulations and higher-fidelity results. Nevertheless, the majority of the early design iterations and component-level assessments were carried out using the student edition, providing valuable insights into the core interactions within the system.

3.5.1.1 Magnet Characterisation

The first step in understanding and optimising the electromagnetic behaviour of the system was to model the permanent ring-shaped NdFeB Grade 42 magnet. *Image 1* illustrates the magnet's dimensions (outer radius, inner radius, and thickness), sourced from a commercial supplier's datasheet. By importing the supplier's material properties—including the relevant **B-H curve**—into Ansys Maxwell, the simulation accurately captured the magnet's remanent flux density and relative permeability.

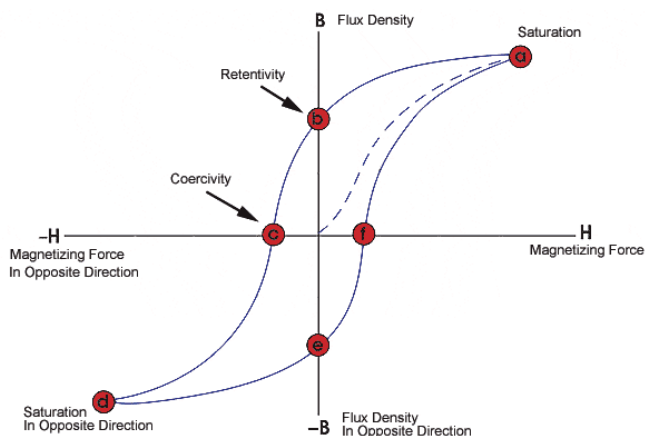


Figure 3.5.1 : B-H Loop of Magnetic Material [67]

- **Remanent Flux Density (Br):** The datasheet specifies a remanent flux density $B_r = 1.316 \text{ T}$ for Grade 42 NdFeB. However, simulations indicated a maximum flux density in the magnet of approximately 1.143T . This discrepancy can arise from several factors:

- Mesh Limitations:** Particularly when using the student version of Ansys Maxwell, the mesh refinement may not fully capture localised hotspots of high flux density, leading to slightly conservative estimates.
- Real-World Conditions:** Imperfections in manufacturing or material characteristics can also influence the measured or simulated flux density, making it somewhat lower than the idealised B_r value.

Ultimately, the 1.143 T result is still within a reasonable range for this magnet grade, illustrating that the simulation closely approximates the real magnet's performance, if not matching the absolute theoretical maximum.

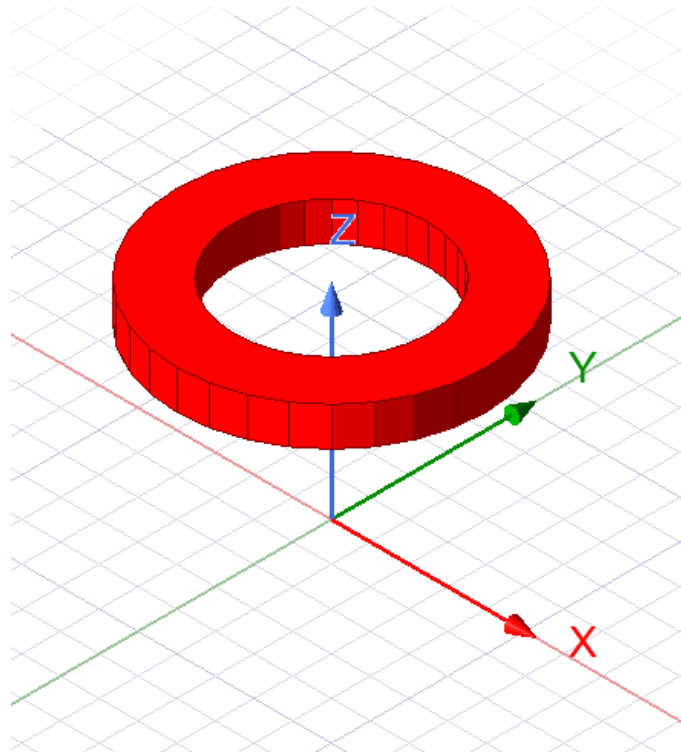


Figure 3.5.2 : Ring Magnet Ansys Maxwell

As the magnet is cylindrical in shape, the coordinate system used to define its magnetisation is crucial for ensuring accurate analysis. The default Cartesian system (X, Y, Z) can sometimes be less intuitive or lead to complications in defining radial or axial magnetisations for cylindrical geometries. Consequently, the magnet's coordinate system was switched to a cylindrical basis—defined by (R, ϕ, Z) .

Axial Magnetisation Setup:

By assigning a +1 in the Z-direction and 0 in the R and ϕ directions, the simulation interprets the magnet as being magnetised along the Z-axis (i.e., axially). This corresponds to a “through-thickness” magnetisation, where the north pole is on one flat face and the south pole on the opposite face of the ring magnet. Such a configuration precisely reflects the real-life orientation of the magnet in the prototype, ensuring that the simulated field aligns with physical expectations.

This attention to both the magnet's material properties and its coordinate system underpins the fidelity of the simulation. Establishing accurate definitions for remanent flux density, spatial orientation, and magnetisation direction is vital before integrating the magnet with other components (such as iron cores and coils).

Figure below detail the parameters used for defining the magnet's material properties within Ansys Maxwell, including the demagnetisation curve and the maximum energy product. These data points ensured that the simulation accurately reflected the magnet's real-world performance, especially under varying operating conditions.

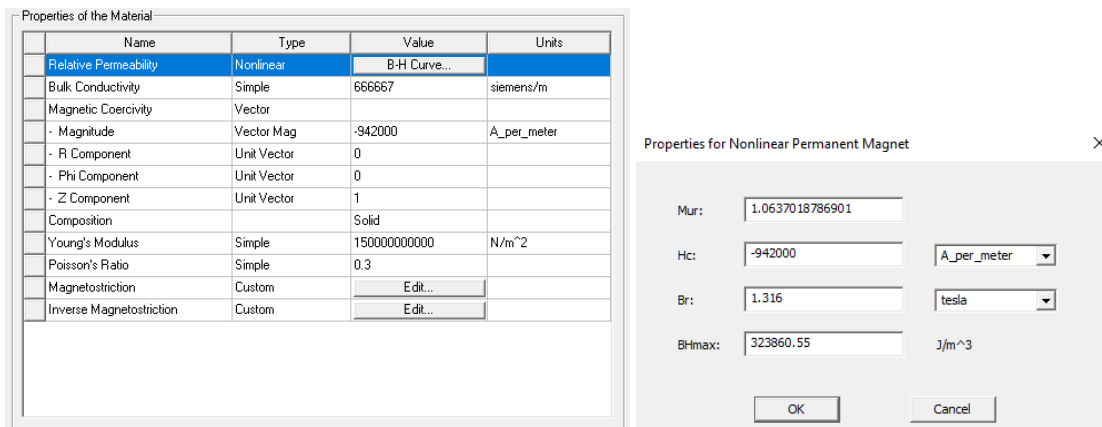


Figure 3.5.3 : Material Properties of PM

Subsequent magnetic field plots reveal the magnet's flux density (**B**) and magnetic field strength (**H**), confirming the strong field characteristics expected from Grade 42 NdFeB.

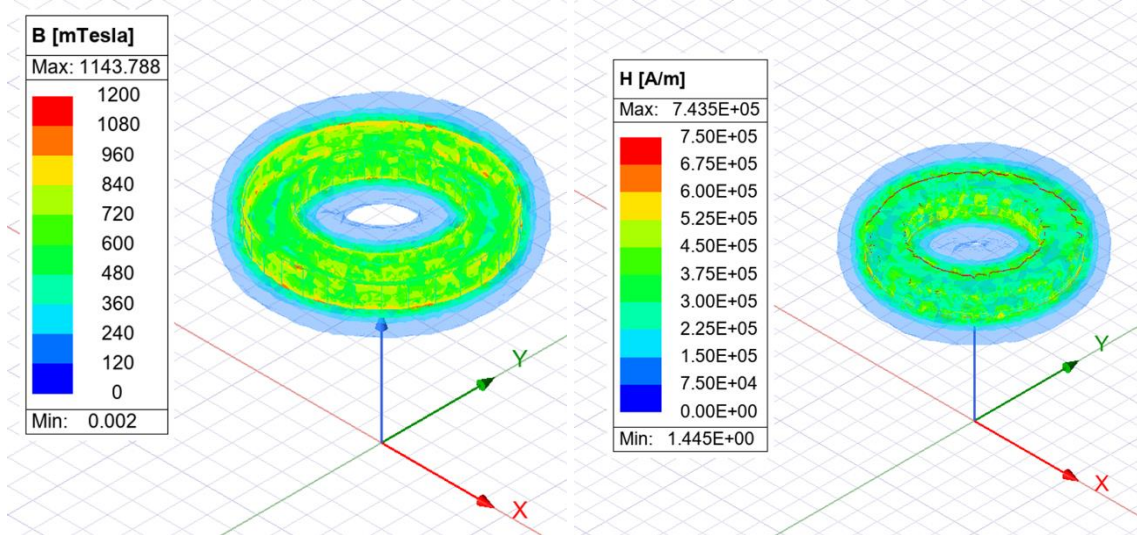


Figure 3.5.4 : Magnetic Flux Density and Field Strength

By isolating and studying the permanent magnet as an individual component, it was possible to validate that the magnet's specifications matched both the manufacturer's claims and the software's theoretical predictions. This step laid a solid foundation for subsequent integrations with other components, such as iron cores, coils, and the moving mass, as discussed in the following sections.

3.5.1.2 Core Characterisation

Following the permanent magnet assessments, attention turned to the iron core—an integral element for concentrating flux and enhancing electromagnetic interactions within the proposed electromagnetic-gravity system. As with the magnets, preliminary finite element analyses were conducted using the student edition of Ansys Maxwell to establish basic field interactions and loss characteristics. The initial studies provided critical insights into core geometry and performance before transitioning to higher-fidelity simulations.

Core Geometry and Material Properties

The iron core was designed as a hollow cylinder with a total height of 600 mm, an outer radius of 8 mm, and an inner radius of 6.75 mm. This geometry was selected to accommodate the permanent magnets and moving weight within the core's central bore, as illustrated in Image X. In early conceptual designs, the intention was to wind the coils on the **inside** of the hollow core to keep the magnetic circuit compact. Practical considerations, however, prompted a design revision that placed the coils on the **outside** of the core, simplifying the fabrication process while retaining a high-permeability path for the magnetic flux.

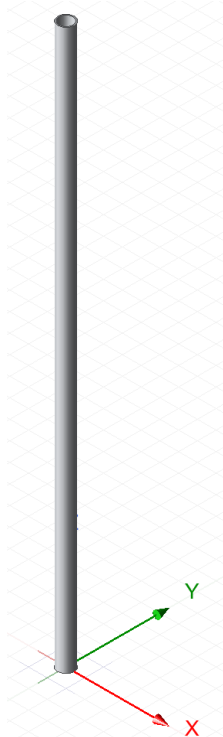


Figure 3.5.5 : Iron Core in Ansys Maxwell

The chosen material, an iron grade with an assumed relative permeability (μ_r) of 4000 and a saturation flux density of 1.5 T, was imported into Ansys Maxwell's material library. These properties ensure strong magnetic coupling between the electromagnets and the permanent magnets, thereby increasing the net force of attraction or repulsion during the energy storage (lifting) phase. Figure 3.5.6 below provide a summary of the assigned material data of the iron core.

The screenshot shows a software interface for material properties. On the left is a table with columns for Name, Type, Value, and Units. The table includes entries for Relative Permittivity (Simple, 1), Relative Permeability (Simple, 4000), Bulk Conductivity (Simple, 10300000, siemens/m), Dielectric Loss Tangent (Simple, 0), Magnetic Loss Tangent (Simple, 0.005), Core Loss Model (w/m^3), - Kh (Simple, 0.25), - Kc (Simple, 0.15), - Ke (Simple, 0.015), - Y (Simple, 2), Mass Density (Simple, 7870, kg/m^3), and Composition (Solid). To the right are several configuration panels: 'Active Design' (radio button selected), 'Active Project' (radio button unselected), 'All Properties' (radio button unselected), 'Physics:' (checkboxes for Electromagnetic, Thermal, Structural all checked), 'View/Edit Modifier for' (checkboxes for Thermal Modifier and Spatial Modifier both unselected), 'Material Appearance' (checkbox checked, 'Use Material Appearance'), and 'Color' (a color swatch).

Name	Type	Value	Units
Relative Permittivity	Simple	1	
Relative Permeability	Simple	4000	
Bulk Conductivity	Simple	10300000	siemens/m
Dielectric Loss Tangent	Simple	0	
Magnetic Loss Tangent	Simple	0.005	
Core Loss Model			w/m ³
- Kh	Simple	0.25	
- Kc	Simple	0.15	
- Ke	Simple	0.015	
- Y	Simple	2	
Mass Density	Simple	7870	kg/m ³
Composition		Solid	

Figure 3.5.6 : Summary of Iron Core Properties

Rationale for Core Loss Analysis

Given the system's reliance on time-varying electromagnetic fields, accurately predicting core losses was deemed paramount for estimating thermal effects and overall energy efficiency. Early simulations in the student edition enabled basic visualisation of eddy current distributions, but were constrained by mesh refinement and solver limitations. Once migrated to the full Ansys Maxwell suite, these constraints were lifted, allowing finer-resolution modelling of:

1. **Hysteresis Losses (K_h)** – Arising from the intrinsic resistance of iron to changes in magnetisation, dependent on the coercivity and operating frequency.
2. **Classical Eddy Current Losses (K_c)** – Generated by currents induced within the solid (non-laminated) core, influenced heavily by the square of the frequency and the conductivity of the iron.
3. **Excess Eddy Current Losses (K_e)** – Representing anomalous phenomena not captured by standard hysteresis or classical eddy current models, often becoming significant at higher operating frequencies or with certain core geometries.
4. **Steinmetz Exponent (γ)** – This exponent defines how hysteresis losses scale with flux density, shaping the non-linear relationship between the magnetic field and the energy dissipated in each magnetisation cycle. Typical values for iron-based materials range between 1.8 and 2.5, with higher numbers indicating a more pronounced rise in losses as flux density increases.

To quantify these losses, the system was operated at representative frequencies consistent with the pulsed current profile (0.5 A pulses) used to drive the electromagnets. By incorporating the relevant Steinmetz parameters (e.g., K_h , K_c , and K_e) within the Ansys Maxwell environment, core loss predictions were refined to reflect realistic operational conditions.

By integrating the above geometry, material properties, and Steinmetz-based loss calculations, the final simulations offer a refined understanding of how the iron core behaves under both lifting and generation scenarios. The approach ensures that thermal effects, eddy current distributions, and hysteresis characteristics are accounted for, thus improving confidence in overall EMGES performance predictions. Any subsequent prototype design modifications—such as adopting laminated cores or alternative alloys—could similarly be evaluated by adjusting these material parameters and re-running the simulations.

3.5.1.3 Practical Observations and Future Considerations

Most of the prototype development and early integration tests were performed with a solid core, acknowledging that classical eddy current losses tend to be higher in non-laminated materials. In larger-scale or high-frequency applications, substituting a laminated or powdered iron core would likely mitigate eddy currents, reduce heat generation, and improve overall efficiency. Nonetheless, for the present proof-of-concept system, the solid iron core offered sufficient magnetic performance, mechanical robustness, and ease of manufacturing—albeit at the expense of some additional thermal and loss considerations.

By conducting this iterative core analysis in both the student and full versions of Ansys Maxwell, it was possible to balance early design simplifications against the need for more accurate, mesh-intensive simulations. As such, the iron core's dimensions, high-permeability characteristics, and hollow geometry were validated, confirming their suitability for effectively coupling the magnetic field with the permanent magnets and supporting the broader operational goals of the electromagnetic-gravity apparatus.

3.5.1.4 Coil Characterisation

An essential aspect of this project involved accurately representing the copper coils that drive the electromagnetic interactions in the system. Initially, user-defined spiral helix geometries were employed within Ansys Maxwell to capture the full complexity of the coil windings, including wire diameter, helix radius, pitch, and spiral shape. This level of detail facilitated quick adjustments based on different AWG specifications, but it also led to significant computational overhead. The student version of Ansys Maxwell limits simulations to a maximum of 64,000 mesh elements, and highly detailed helical models approached or exceeded this threshold, causing lengthy run times and limited mesh fidelity.

To overcome these computational constraints, a simplified coil geometry was developed. This approach entailed subtracting a smaller cylinder from a larger one, effectively leaving an annular region corresponding to the coil's outer and inner diameters. A coil terminal was then applied within Ansys Maxwell, allowing direct specification of the number of turns (N) and the winding current (A). This simplified representation continued to reflect the correct physical dimensions—height, inner/outer radii, and approximate wire diameter—while drastically reducing computational complexity and mesh-element demand.

Validation of Simplified Geometry

To ensure the simplified geometry remained valid, **comparative simulations** were run against the more complex spiral-helix model. Results showed that:

- **Magnetic Flux Density (B):** The complex model reached approximately 430 μT , whereas the simplified model measured around 425 μT .
- **Magnetic Field Strength (H):** The complex geometry produced 342 A/m, while the simplified geometry gave 338 A/m.

These discrepancies (about 5 μT and 4 A/m, respectively) were deemed negligible for design and performance considerations. Moreover, both geometries showed the same regions of maximum **B** and **H**, further substantiating the simpler coil geometry's accuracy. Consequently, the simplified model was adopted for all subsequent analyses, striking a balance between simulation speed and physical realism.

Thermal Degradation Model

A thermal degradation model was also integrated into Ansys Maxwell to account for the change in copper's conductivity above 22 °C. Building upon a method demonstrated in an Ansys Maxwell tutorial, the temperature coefficient for copper of 0.0039 $^{\circ}\text{C}^{-1}$ was applied. This reflects the well-known increase in copper's electrical resistivity with temperature. In practical terms, as the coil's temperature rises, atomic vibrations impede electron flow, reducing conductivity. Incorporating this model allowed for a more realistic assessment of the coil's performance under various thermal conditions, anticipating potential efficiency losses and heat-related constraints when operating at higher currents or for prolonged periods.

Overall, these coil modelling strategies—ranging from complex spiral helix to simplified annular representation—enabled efficient parametric studies and reliable electromagnetic analyses, even under the mesh limitations of the student version of Ansys Maxwell. The final approach delivers an accurate yet computationally manageable framework, ensuring that the copper coils remain a well-characterised component in the broader electromagnetic-gravity system.

3.5.1.5 Bronze Weight Characterisation

A bronze weight was introduced into the system to serve as the mass for gravitational energy storage. Since bronze typically consists of copper (diamagnetic) and tin (paramagnetic), it was expected to exhibit minimal interaction with magnetic fields. To confirm this assumption, a series of simulations compared the PMs flux distribution both with and without the bronze weight present.

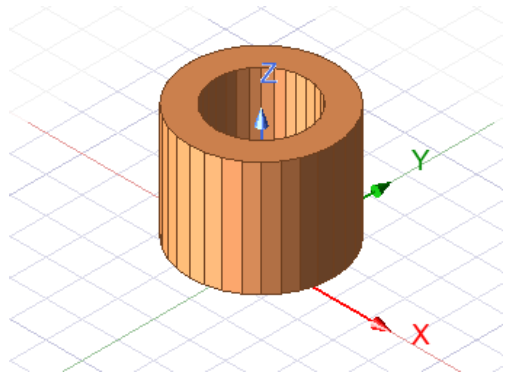


Figure 3.5.7 : Bronze Weight Ansys Maxwell

Results indicated that the overall magnetic flux density (B) and field vector distribution remained effectively unchanged when the bronze weight was introduced. This outcome verifies that the bronze component does not distort or attenuate the PM's field, making it suitable for use as a non-magnetic mass. In addition, because the weight moves in tandem with the magnets through the core housing, it experiences minimal or zero relative change in magnetic flux. This significantly reduces the likelihood of induced eddy currents, resistive heating, or thermal expansion in the bronze mass.

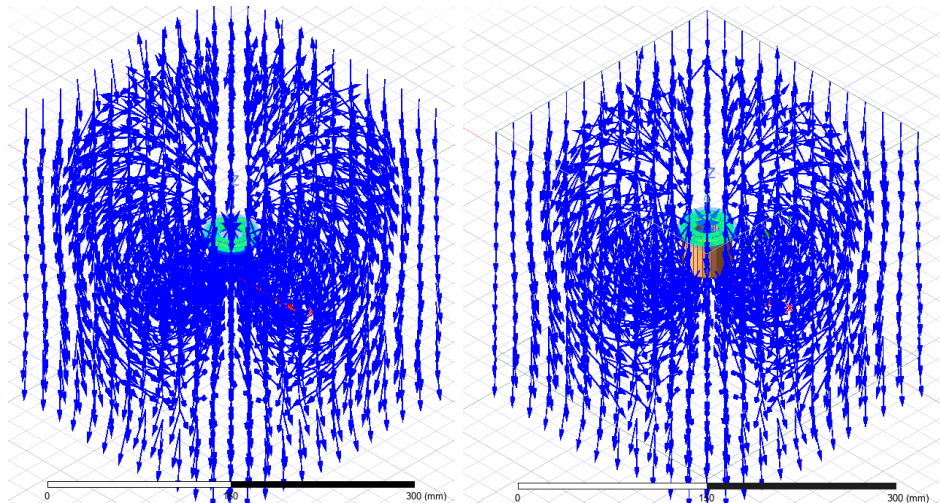


Figure 3.5.8 : Permanent Magnet vs. Magnet with Bronze Weight Flux Density

The only notable magnetic field variations arise from the eddy currents induced in the copper coils wound around the iron core, where the potential for resistive heating and thermal effects is higher but still minimal. Although these phenomena were accounted for in the simulation setup—by enabling eddy current calculations for relevant components—the bronze weight itself was confirmed to remain electrically and magnetically inactive throughout its motion. Consequently, bronze was deemed an appropriate, low-interference choice for providing the gravitational mass required by the electromagnetic-gravity system.

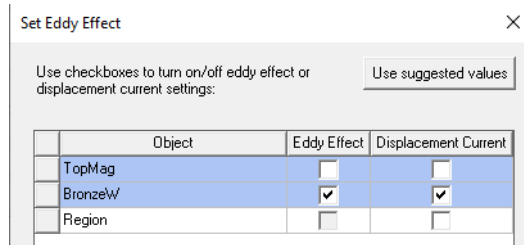


Figure 3.5.9 : Set Eddy Effects

3.5.1.6 Guiderail Characterisation

In addition to the iron core and magnetic components, PVC guiderails were incorporated into the simulation model to replicate the physical constraints present in the prototype. Ansys Maxwell offers a pre-loaded material library for PVC plastic, featuring near-unity relative permeability and negligible electrical conductivity. By assigning these properties to the guiderails, the software could precisely evaluate any potential interactions between the rails and both the permanent magnet and the electromagnetic field.

The simulation results indicated minimal interference from the PVC guiderails. Owing to PVC's negligible magnetic and conductive characteristics, flux lines traversed the guiderails with negligible distortion, and eddy current formation was effectively absent. These findings validate the assumption that PVC acts primarily as a structural and guiding component without adversely affecting the magnetic circuit or the system's overall efficiency.

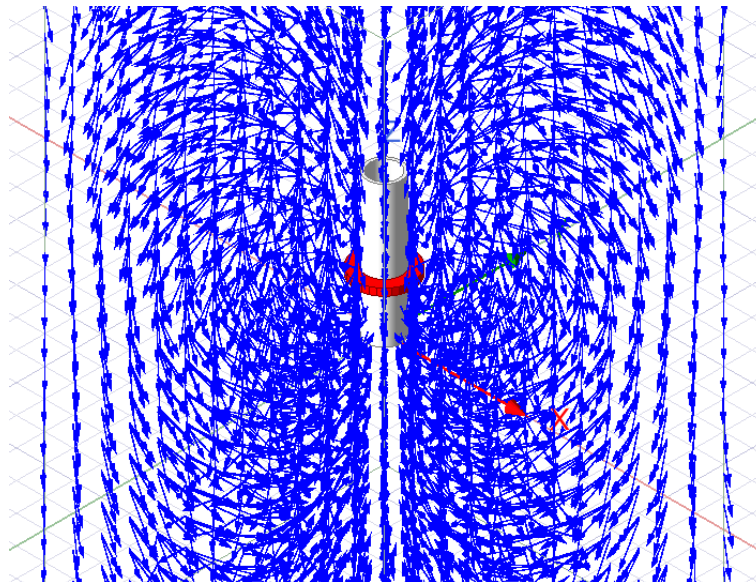


Figure 3.5.10 : Magnetic Flux Density with PVC

Moreover, PVC's smooth, low-friction surface facilitates the free movement of the magnet-weight assembly within the guide. Following the simulation phase, a transparent PVC pipe was selected for the physical prototype. This decision offered the benefit of direct observation of the permanent magnets' position relative to the electromagnet coils during testing as no position sensor was used for the used or the prototype model. The use of smooth PVC also minimised frictional forces that could otherwise distort the results or impede the assembly's vertical motion.

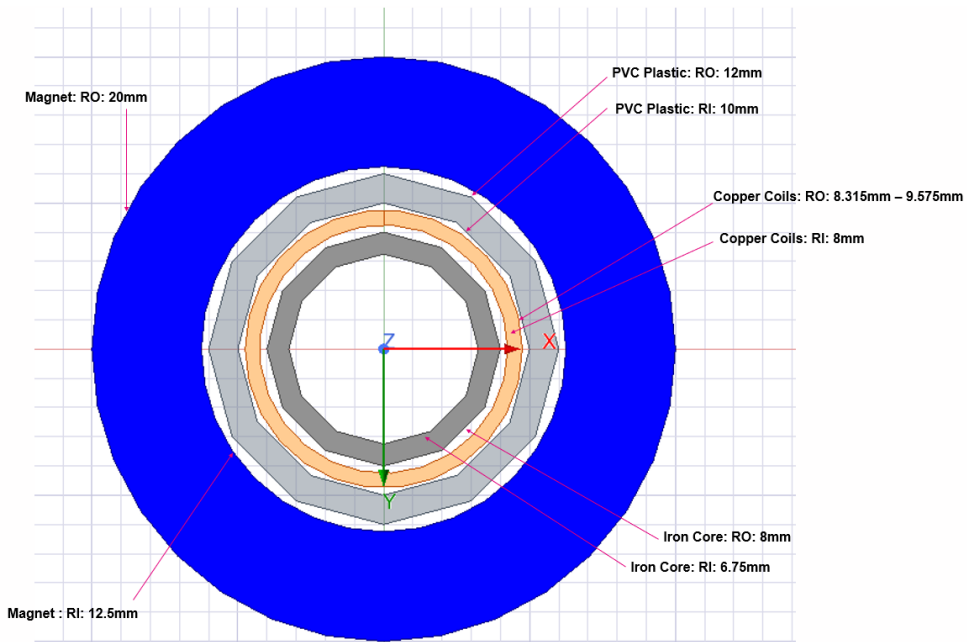


Figure 3.5.11 : EMGES Cross Section with Radii

3.5.2 Flux Distribution and Gradient Analysis

The determination of optimal coil length in this study was guided by the need to balance electromagnetic coupling efficiency with the functional requirements of storing mode, where the EMGES system must generate sufficient force to lift a weight vertically. Central to this evaluation was a detailed analysis of the **magnetic flux gradient** around a ring-shaped PM positioned externally around the iron core and surrounding coils.

The magnetic flux gradient, expressed in Wb/mm, represents the rate of change of magnetic flux with respect to distance along the magnet's axis. This gradient plays a direct role in the generation of EMF in accordance with Faraday's Law of Induction (Equation 3.3.2), which states that EMF is proportional to the rate of change of magnetic flux and the relative velocity between the coil and the moving magnet. Figure 3.5.12 illustrates the magnetic flux gradient as a function of axial position for the ring magnet configuration.

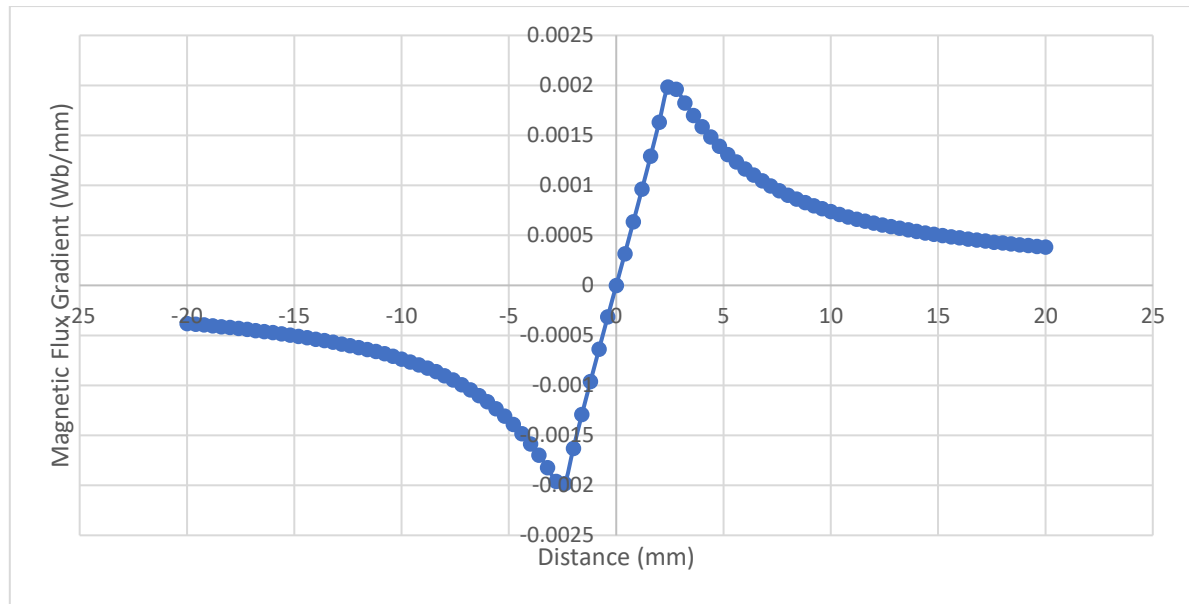


Figure 3.5.12 : Magnetic Flux Gradient vs Distance

This curve exhibits a symmetrical profile centred around the magnet's mid-plane, with steep opposing gradients that change sign at the centre. The zero-crossing point, where the direction of the magnetic flux gradient changes due to the magnets polarity, located at 0 mm, represents the magnet's axial midpoint, and the steepest regions on either side define the zones of greatest flux variation—key regions for maximising EMF.

A critical step in determining the coil length was inspired by Dr Damien Carroll's work, in which a threshold of 10% of the maximum flux density was used to optimise coil placement for miniaturised electromagnetic generators [68]. Carroll's lower threshold allowed material savings and greater efficiency for small-scale harvesters. By contrast, the present study required a higher threshold of 50% to meet the demands of storing mode in the EMGES, where a stronger magnetic response is essential for lifting the weight.

Subsequent simulations in Ansys Maxwell showed that a 15 mm coil length, aligned with the 50% threshold, captured a significant portion of the peak flux gradient without unnecessarily complicating the winding process. Shorter coils tended to miss portions of the most active flux region, resulting in lower potential coupling, while longer coils did not proportionally increase performance and risked inefficient use of materials. The design included a 3.5 mm stand-off distance from the magnet, which accommodates a realistic copper fill factor of 0.8, reflecting the practical stacking of multiple wire turns within a limited radial space.

These findings were systematically applied during the prototype design phase, where the coil's dimensions and placement were refined to ensure optimal overlap with the magnet's most intense flux region. By linking the practical coil manufacturing requirements (such as copper winding, fill factor, and spool dimensions) to the flux gradient insights, the resulting coil arrangement meets the dual objectives of high electromagnetic coupling and reliable mechanical operation. This integrated approach builds upon Carroll's earlier research while addressing the specific mechanical and performance demands of the EMGES in its storing mode.

Evaluation of Internal Disc Magnet Configuration

To explore alternative geometries for electromagnetic coupling, a second magnetic arrangement was simulated using Ansys Maxwell. This involved replacing the external ring magnet with a solid disc-shaped N42-grade NdFeB permanent magnet, axially magnetised and positioned inside the hollow iron core. Coils were also placed internally, surrounding the central shaft in close proximity to the disc magnet's poles. The objective was to examine whether this configuration offered improved flux gradients and, by extension, greater induced EMF in storing and generation modes.

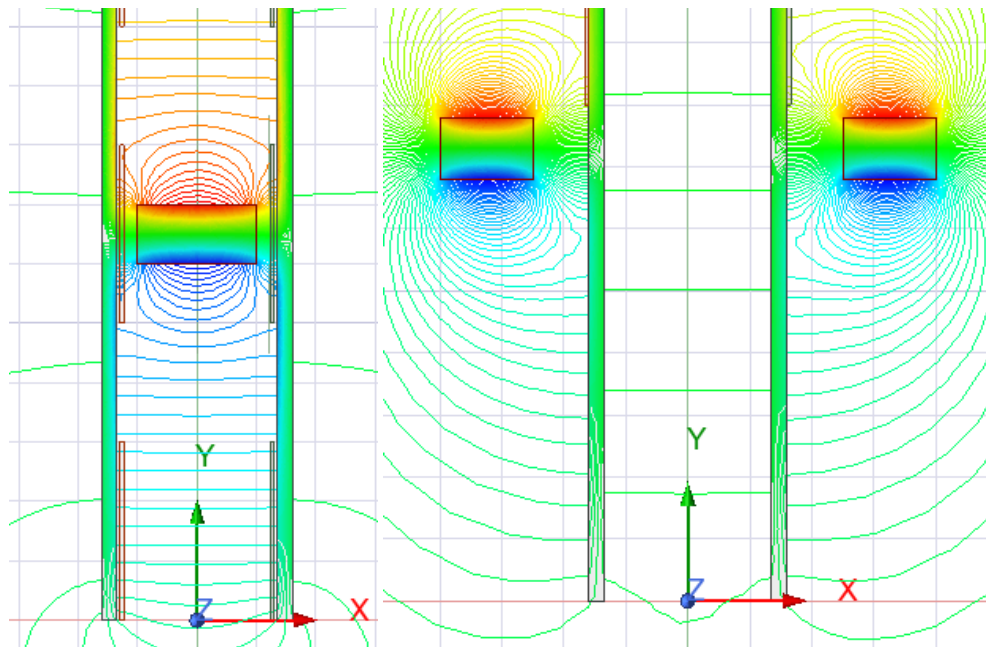


Figure 3.5.13 : Flux Gradient Comparison

The simulation results showed a substantial increase in the magnetic flux gradient within the coil region compared to the ring magnet setup. As visualised in Figure 3.5.13, the internal disc magnet produced a flux gradient nearly three times greater than that observed in the external ring magnet configuration. This steeper gradient occurred across a more concentrated distance around the magnet's mid-plane, indicating stronger electromagnetic coupling within the same coil length.

According to Faraday's Law of Induction, the EMF induced in a coil is proportional to the rate of change of magnetic flux ($d\phi/dt$). Therefore, if the number of turns remains the same, a threefold increase in the flux gradient would result in an approximately threefold increase in induced EMF, assuming the same relative velocity between the magnet and the coil. This improvement directly translates to higher instantaneous power output for generation mode or increased lifting force in storing mode, provided that current delivery is sufficient.

Despite its promising magnetic characteristics, this internal disc magnet configuration was deemed impractical for physical implementation in the current prototype. The iron core used in the prototype had an inner radius of just 8 mm, leaving insufficient space to wind a meaningful number of turns inside the core. Achieving high coil density within such a confined

volume would require extremely fine wire gauges, which introduce high resistance and are challenging to manage mechanically.

Furthermore, this configuration introduces an additional complication: strong magnetic attraction between the disc magnet and the surrounding iron core. While the iron enhances magnetic permeability and improves flux channelling, it also acts as an attractive path for the magnet, potentially distorting its motion or requiring additional force to overcome this attraction during operation. This effect was not observed in the ring magnet design, where the magnets remained external to the iron structure. A detailed force analysis of this interaction will be presented later in the report to assess its impact on system efficiency and control requirements.

In conclusion, while the internal disc magnet setup offers clear magnetic performance advantages in simulation, practical limitations—particularly spatial constraints and magnetic adhesion—currently outweigh these benefits in a small-scale prototype. However, this geometry remains a promising candidate for future scaled-up implementations, where core diameters allow more flexible winding strategies and better management of magnetic forces.

3.5.3 Coil Placement Location

A critical aspect of designing the EMGES involves determining the optimal placement of the coils relative to the PM to ensure there is always amount force to raise the system in storing mode. The main driver for this calculation is the force of attraction between two magnets, represented by equations 3.3.10 and 3.3.11. In these formulations, the interaction parameters between the EM and PM are considered, including B, radial offsets, and axial distances.

Superposition of Magnetic Fields

The principle of superposition is invoked by expressing the total magnetic flux density as the square of the sum of the individual fields from the PM and EM at a given position. Specifically, B^2 from 3.3.10 and 3.3.11 is taken as $(B \text{ from PM} + B \text{ from EM})^2$, capturing the combined effect of both fields on the force. Equation 3.3.9, in conjunction with Ansys Maxwell simulations, was employed to predict how the EM's magnetic field would vary with different coil turn counts and currents. This provided a range of B values arising from the EM alone, which were subsequently superimposed onto the PM's field.

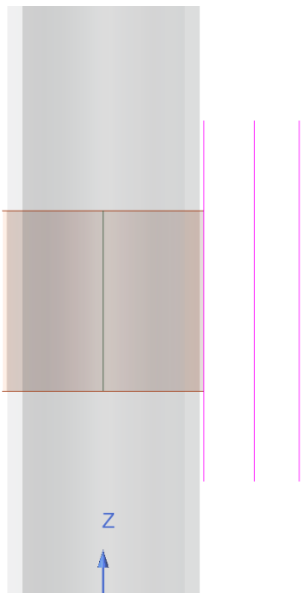


Figure 3.5.14 : EM and Lengths of Analysis at Different Coordinates

Non-Overlapping Magnet Surfaces

Since the PM and EM do not share overlapping surface areas, it was necessary to extract the (B) from Maxwell along specific paths in the z-direction. Figure 3.5.14 shows three different lines in the x-z plane, each reflecting a unique offset in the x direction of 0mm, 4mm and 8mm. The solver provided the B values along these lines, enabling the calculation of axial force in discrete intervals of the PM's motion assuming a conservative area of interaction of that of the iron core. This approach allowed for low, yet realistic, values of force of interaction to be calculated. This line-based approach was essential in determining how variations in x-offset might affect total force and identifying optimal coil placements for both lifting and generating modes.

Analysis of Force vs. Position Maxwell 3D

To compare the theoretical results, a 3D model was designed in the Magnetostatic solver. The purpose of this was to evaluate the force distribution throughout the PM's travel along the z-axis. To simulate this PM was moved axially at 1mm intervals, while the EM was kept stationary. At each incremental position of the PM, the axial force was calculated by Ansys Maxwell's solver to 0.6% error. Figure 3.5.15 and Figure 3.5.16 illustrate these force profiles and directions.

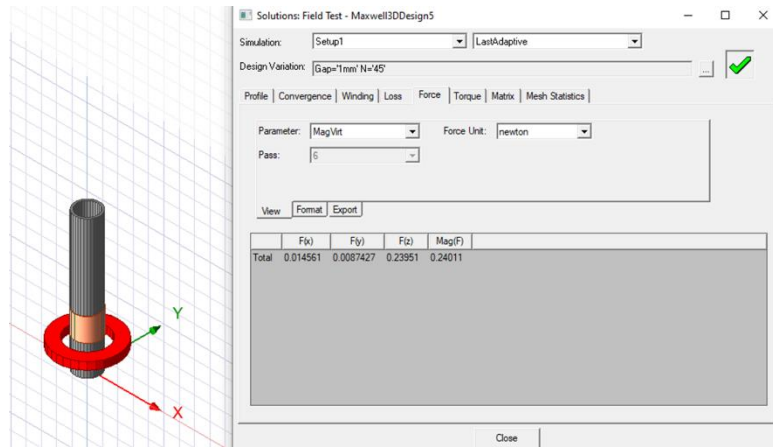


Figure 3.5.15 : Force Analysis of Components

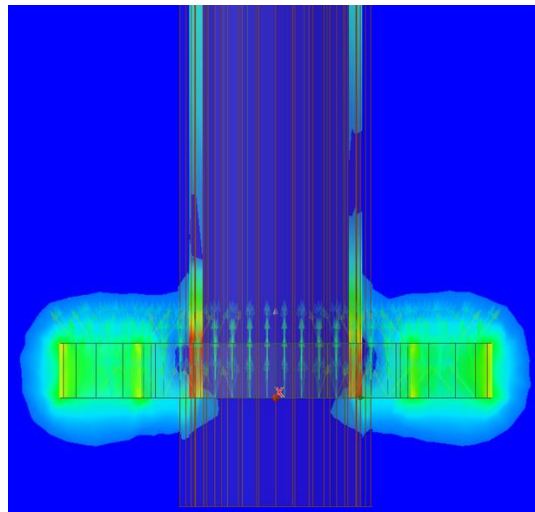


Figure 3.5.16 : Force Direction

Overall, this combination of analytical equations (Equations 3.3.9, 3.3.10, 3.3.11) and numerical simulations in Ansys Maxwell allowed for a systematic examination of force as a function of PM location relative to the coils location. By correlating the discrete B profiles with the known PM behaviour at different z positions, the design of the coil placement was refined to balance mechanical feasibility, magnetic performance, and energy conversion efficiency.

3.5.4 Finite Element Analysis (FEA)

The EMGES model was created and analysed in Ansys Maxwell, a FEA software focused on electromagnetic field simulations. The Magnetostatic solver was employed because it offers three-dimensional, stationary simulations suitable for evaluating the steady-state behaviour of the integrated system. Initially, each component (copper coils, iron core, and permanent magnets) was tested and verified independently. These components were then combined into a unified three-dimensional assembly to examine the electromagnetic interactions and forces within the EMGES.

When access to the full Ansys Maxwell Electronics Suite was available, the Transient solver was investigated in order to capture the dynamic aspects of the design. However, the software was unable to correctly interpret a configuration in which the permanent magnets

and weight—located on the “outside” of some “other components”, being the iron core and coils setup—were the only parts in motion. Various attempts were made to overcome this by assigning the moving attribute to the core and coils instead, but these strategies also failed to resolve the limitation. Discussions with Ansys Maxwell employees confirmed that this issue reflects a newly discovered constraint in the software, which currently does not permit the precise configuration required for the EMGES’s external moving magnet arrangement.

Zero tangential H-field boundary conditions were applied to the simulation domain, which was set to air. These boundary conditions ensure that magnetic field lines do not escape tangentially, effectively replicating an open environment. This approach is essential for avoiding unnatural reflections or distortions at the domain boundaries, thus preserving the accuracy of the modelled magnetic fields.

To capture the interaction between the coils and the iron core, each coil was placed concentrically around the core with a shared radius of 8 mm. Since the coils must not conduct current into the core, an insulating boundary was imposed at the coil-core interface. These conditions maintain electrical isolation between coil and core while still permitting accurate modelling of their magnetic coupling, ensuring that current paths are confined to the intended conductors.

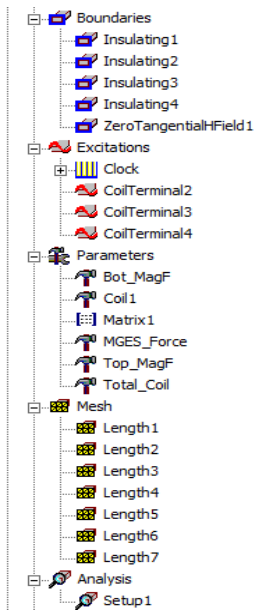


Figure 3.5.17 : Ansys Maxwell Simulation Setup

During the simulations, the input current direction for the coils was adjusted according to the permanent magnets’ position relative to each coil. This method provided the correct orientation of magnetic poles for achieving the desired mechanical and electromagnetic effects, where opposite poles attract and like poles repel.

Virtual force parameters were assigned to the system’s components in Ansys Maxwell, allowing force calculations to be performed without tangible movement. These parameters are vital for investigating how electromagnetic forces affect system alignment, motion, and stress.

Where suitable, selection length-based meshing was implemented—particularly around the copper coils—to produce finer mesh elements in areas of high importance or complexity. This approach assigns a target element size to selected geometric features, improving accuracy in regions most critical to electromagnetic calculations. However, owing to the element count limitations of the Ansys Maxwell Student Version, this detailed meshing strategy was only used where it was most beneficial, striking a balance between computational feasibility and model accuracy.

Finally, the electromagnetic transient solver was configured with a convergence target of 0.6%, meaning the solver would iterate until the change in simulated values fell below that threshold. In practice, certain simulations—especially those with finer meshes or complex geometries—required this convergence criterion to be eased to 1.0% to remain within the imposed element limit, while still delivering satisfactory accuracy.

3.5.5 Description of final choices

The selection of components for the EMGES proof of concept model was based on a combination of performance, cost, availability, and practicality considerations. This section elaborates on the rationale behind the final choices of materials and configurations for the key components of the EMGES.

Iron Core

For the core of the EMGES, iron was selected over silicon steel despite the latter's superior performance in terms of efficiency and eddy current reduction. The primary factors influencing this decision were:

- **Cost-Effectiveness:** Iron is significantly less expensive than silicon steel, making it a more viable option for a proof of concept where budget constraints are critical.
- **Material Availability:** Iron is more readily available and accessible, facilitating easier sourcing and quicker assembly for the prototype.
- **Simplicity in Handling and Processing:** Iron is easier to machine and handle compared to silicon steel, which requires more specialized processes due to its higher silicon content.

These factors made iron a practical choice for the initial model, allowing for a cost-effective and timely exploration of the EMGES concept.

18 to 28 Gauge Copper Coils

The copper coils were selected based on their electrical properties and physical suitability for the design:

- **Resistance Characteristics and Current Load Capacity:** 18 to 28 gauge copper wire offers an optimal balance between resistance and current-carrying capacity, ensuring efficient energy transfer without excessive heat generation.

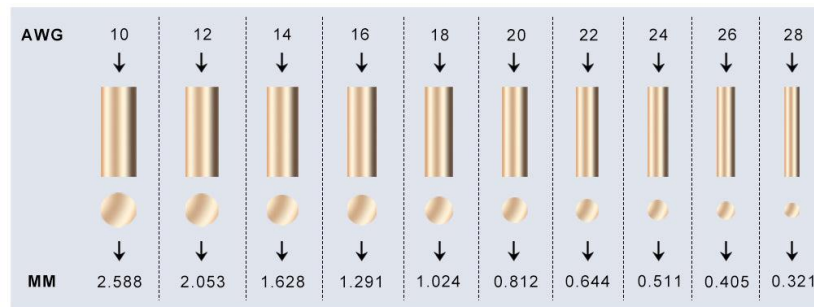


Figure 3.5.18 : AWG Size Comparison [69]

- **Optimal Number of Turns:** This gauge allows for the necessary number of turns to be wound along the iron core, maximizing the magnetic field interaction without overly increasing the coil resistance, which is crucial for maintaining high efficiency in energy conversion.

Ring-Shaped Neodymium Magnets

Ring-shaped Neodymium magnets, axially magnetized, were chosen for several reasons.

- **Magnetic Field Concentration:** The ring shape helps focus the magnetic field across the gap where interaction with the coils occurs, enhancing the efficiency of the magnetic flux linkage.
- **Axial Magnetization:** This orientation aligns the magnetic poles along the axis of movement, optimizing the interaction with the electromagnetic field generated by the coils, which is crucial for maximizing the output during the energy conversion process.

Bronze Weight

Bronze was selected as the material for the weight, configured into a ring shape to match the dimensions of the neodymium magnets:

- **Density and Mechanical Properties:** Bronze offers a good balance of density and mechanical strength, which is essential for effective gravitational energy storage within the compact design of the EMGES.
- **Cost and Availability:** Similar to the selection of iron, bronze provides a cost-effective alternative with greater availability compared to denser metals like tungsten, which may be considered in more advanced versions of the system.

PVC Plastic Housing/Guide Rails

PVC plastic was chosen for the housing and guide rails due to its:

- **Insulating Properties:** PVC offers excellent electrical insulation, which is vital for safety and efficiency.
- **Durability and Cost-Effectiveness:** It combines strength and resistance to environmental factors with low cost, making it ideal for the prototype stage where cost considerations are significant.

- **Ease of Fabrication:** PVC can be easily shaped and fitted around the system's components, facilitating smooth operation and integration.

These material choices reflect a strategic approach to developing a functional and efficient EMGES prototype, balancing performance with practical project constraints. Each component was selected to contribute optimally to the system's overall functionality while adhering to budgetary limits and availability constraints.

3.6 Prototype Implementation

3.6.1 Prototype Fabrication

To translate the theoretical EMGES design into a functional prototype, each component was acquired or fabricated with the goal of minimising the air gap between the PMs and the EMs. While the ideal configuration would have placed both PMs and EMs inside the iron core to maximise magnetic coupling and flux linkage, the size constraints of the prototype made it impractical to build such a design at this stage. A more detailed analysis of these trade-offs is presented in the *Results and Analysis* and *Discussion* sections of this report.

Component Acquisition and Fitting

Iron Core

Due to material availability and machining constraints, a hollow cylindrical iron core of the requisite dimensions was sourced from standard piping. Its exterior surface was smoothed to reduce friction and unintentional air gaps.

Permanent Magnets and Electromagnets

The chosen neodymium magnets and copper windings for the electromagnets were selected based on size compatibility with the iron core and desired magnetic properties (e.g. magnet grade, coil turn count).

Every effort was made to position the magnets and coils so their radial offset was minimal.

Housing, Base, and Roof Structure

To secure the PMs and weight within a stable, vertical enclosure, and to provide a mounting platform for the electromagnets, a housing assembly was modelled in Autodesk Inventor. This included:



Figure 3.6.1 : PM and Weight Housing

Base of the Structure

Designed to provide a rigid foundation, capable of supporting the mass of the PMs, iron core, and attached weights.

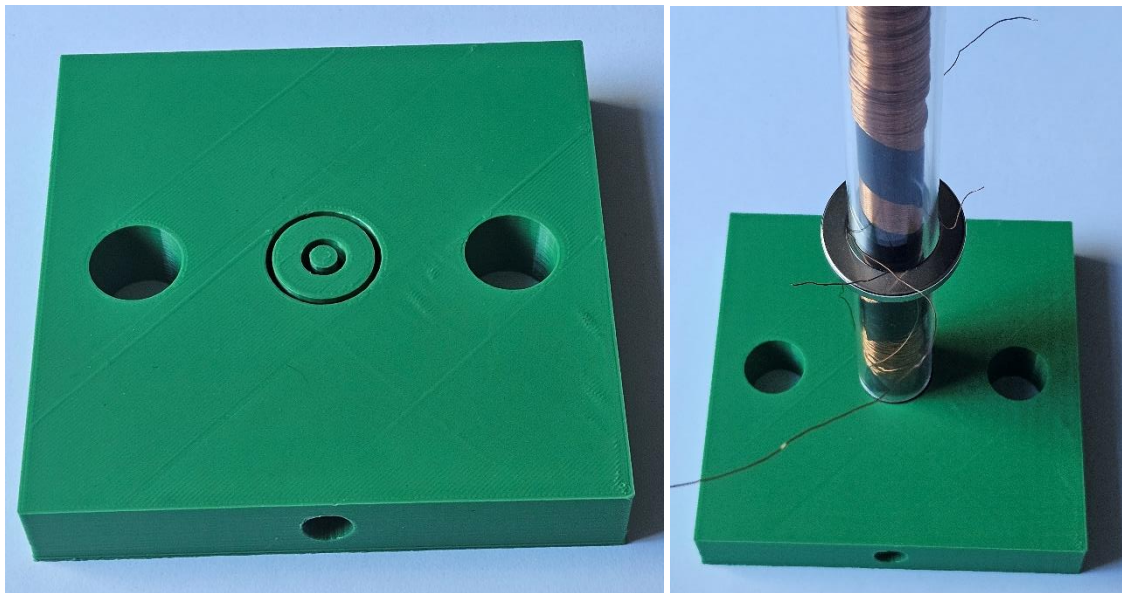


Figure 3.6.2 : EMGES Base Assembly (a) The bare structural base serving as the foundation; (b) The fully assembled base with the integrated system installed

Incorporated mounting points for the iron core, ensuring consistent and straight alignment.

Roof Assembly

Provided an anchoring point for the holding mechanism and allowed for easy access to the top of the iron core.

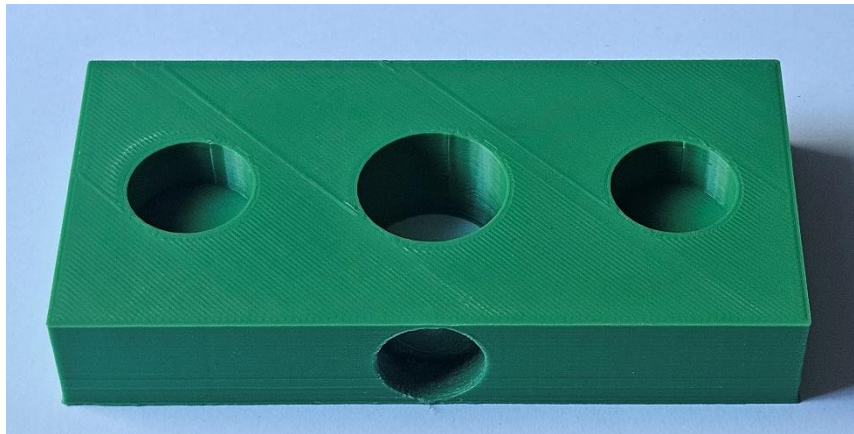


Figure 3.6.3 : EMGES Top Mount for Stability and Cable Management

Reinforced beams in the roof section added rigidity, preventing undesirable vibrations or shifting under load.

Mechanical Hold

A mechanical hold mechanism was designed to secure the PMs and weight upon reaching their maximum travel height. By physically latching at the apex, the system maintains the stored gravitational potential energy without incurring additional electrical power costs, thus improving overall energy efficiency.

All these structural components were 3D printed at the University of Galway. Where possible, tolerances and infill densities were optimised to balance strength with minimal printing material. The plastic parts were subsequently inspected and lightly sanded to ensure accurate fits.

Limitations and Planned Improvements

Size Constraints: The prototype's overall scale limited the possibility of placing both PMs and EMs inside the iron core. A larger Iron core would have been required and was simply not available.

Future Adjustments: A full-scale or improved prototype would employ finer machining and additive manufacturing processes with tighter tolerances, potentially enabling a near-zero radial gap for enhanced magnetic performance.

In sum, the fabricated prototype successfully embodies the core design principles of the EMGES, despite certain concessions made for material availability and manufacturing practicality. These compromises and their impacts on performance are further examined in the following sections.

3.7 Experimental Validation

A laboratory environment was established to evaluate both the generation and storing modes of the EMGES prototype. This setup integrated electrical measurement equipment, a controllable DC power supply, and ancillary tools for secure and accurate data collection. The

primary objectives were to record open-circuit voltages during the generation phase and to measure the force of attraction between the PM and EM when energised.

Measurement Apparatus

Oscilloscope

Utilised for capturing the open-circuit voltage generated by the EMGES in its downward (generation) mode. The oscilloscope provided time-resolved voltage waveforms, allowing detailed characterisation of the induced EMF over the course of each test run.

Test leads were connected to the coil outputs using crocodile clips, ensuring stable electrical contact with minimal signal loss. Care was taken to avoid short circuits or cable damage by stripping back only the necessary length of insulation.

DC Power Supply

Employed to power the coils in the lifting (storage) mode. The power supply enabled precise adjustment of both voltage and current, facilitating tests of electromagnetic force at various operational points.

By gradually increasing the current, researchers were able to quantify how strongly the EM could attract or repel the PM, thereby validating coil design parameters derived from simulation.

Minor Equipment

Wire Strippers: Used to remove insulation around the coil leads without damaging the underlying copper.

Crocodile Clips: Provided reliable clamp connections to the oscilloscope and power supply leads.

Multimeter: Occasionally employed to verify continuity and approximate resistance before connecting to higher-powered devices.

Safety Measures and Risk Mitigation

All work in the laboratory was conducted under the guidelines outlined in the risk assessment document (see “Risk Assessment: Construction and Operation of Magnetic Gravity Energy Storage (MGES) Prototype”). Key safety practices included:

Electrical Safety

Regular inspection of cables for insulation damage.

Strict compliance with recommended voltage and current limits.

Emergency shutdown procedures were in place, ensuring rapid de-energisation if abnormal readings were observed.

Magnet Handling

Maintaining a safe working distance from strong neodymium magnets, especially around sensitive electronic devices or individuals with implanted medical equipment (as highlighted in the risk assessment).

Use of protective barriers around the moving mass and magnets to prevent injuries from sudden attraction or repulsion.

Thermal and Fire Precautions

Continuous monitoring of coil temperature, especially during extended tests at higher currents, to mitigate fire hazards or thermal damage.

Accessible fire extinguishers and clear evacuation routes, consistent with the laboratory's general safety protocols.

Mechanical Movements

Securing the EMGES assembly on a stable surface to prevent tipping or unexpected shifting when the weight was raised.

Ensuring hands and loose clothing were kept clear of moving parts and pinch points.

By adhering to these procedures, the team maintained a safe environment for systematically evaluating the EMGES prototype's electrical outputs in generation mode and its lifting capabilities in storage mode.

3.8 System Modelling and Simulation

In the development of the EMGES, precise control over electromagnetic forces is paramount to ensure efficient and reliable operation. The design and optimization of the electromagnetic control system necessitate sophisticated simulation tools that can model complex electrical behaviours and interactions under various operational scenarios. LTSpice, a powerful and widely used SPICE-based software simulation tool, was selected for this purpose due to its robust capabilities in handling complex electronic circuits and its efficiency in simulating the dynamic behaviours of electrical systems [70].

The primary objective of using LTSpice in this research is to validate the electromagnetic control strategy developed for the EMGES. This involves simulating the electrical circuits responsible for the activation, control, and deactivation of electromagnets within the system. These simulations help in assessing the feasibility of the control logic, timing accuracy, and overall impact of electrical parameters on the system's performance. Moreover, LTSpice enables the detailed visualization of current flows, voltage levels, and power dissipation across the circuit, providing invaluable insights into potential improvements and optimizations.

This section outlines the setup and execution of simulations in LTSpice, detailing the configuration of circuit components, the implementation of control logic, and the interpretation of results. These simulations not only underscore the practical applicability of theoretical designs but also play a crucial role in iterative design refinement, ensuring that

the EMGES meets its designed specifications with high efficiency and reliability. The following subsections will describe the simulation setup, operational logic, and key findings, thus highlighting the integral role of LTSpice in the system's development process.

3.8.1 Simulation Setup

Circuit Design

The LTSpice simulation setup for the EMGES project is designed to closely mimic the electrical system that controls the operation of electromagnets when in storage mode. The circuit mainly consists of two coils, each controlled by a set of transistors that allow for the precise control of current direction through the coils. These coils are essential for creating the necessary magnetic fields to manipulate the movement of the PM and attached weight in the EMGES.

The circuit incorporates Pulse Width Modulation (PWM) sources that govern the timing and intensity of the current through each coil. This control is critical for the synchronization of magnetic field generation with the physical movement of the PM and weight. Power sources are configured to deliver stable and sufficient voltage to ensure continuous operation under varying load conditions.

Component Selection

The selection of components for the simulation was guided by several criteria:

- **Transistors:** Chosen for their fast-switching capabilities and ability to handle the high current required by the electromagnets. Their reliability and efficiency in switching operations under the expected operational frequencies were also key factors.
- **Resistors:** Used to limit the current and adjust the voltage levels within the circuit to safe and efficient operating conditions. Their power ratings and tolerance levels were selected based on the maximum expected current flow.
- **Voltage Sources:** Designed to provide the necessary voltage for coil excitation and to maintain stable circuit operations. The voltage levels were chosen based on the required magnetic field strength for the effective operation of the EMGES.

Control Logic Implementation

Timing control within the circuit is managed using Piecewise Linear (PWL) sources in LTSpice. These sources are configured to output a sequence of voltage levels at predefined times, effectively dictating the operation schedule of the coils. The PWL sources ensure that the current through each coil is activated, reversed, or deactivated at precise moments to synchronize the magnetic forces with the desired motion of the PM and weight.

Gate control for the transistors is implemented using behavioural expressions in LTSpice. These expressions evaluate the voltage from the PWL sources and control the gates of the transistors accordingly. For example, if a specific voltage threshold is exceeded, a transistor may be triggered to conduct, allowing current to flow through one of the coils.

3.8.2 Operational Phases of EMGES

To evaluate the electromagnetic control strategy of the EMGES system during energy storage mode, an H-bridge circuit was developed and simulated in LTSpice. The goal of this simulation was to validate the coil switching behaviour, control logic, and energy transfer dynamics during the coil energisation phase—specifically, as the system simulates lifting a permanent magnet and mass assembly using electromagnetic force. The complete circuit diagram is shown in Figure 3.8.1.

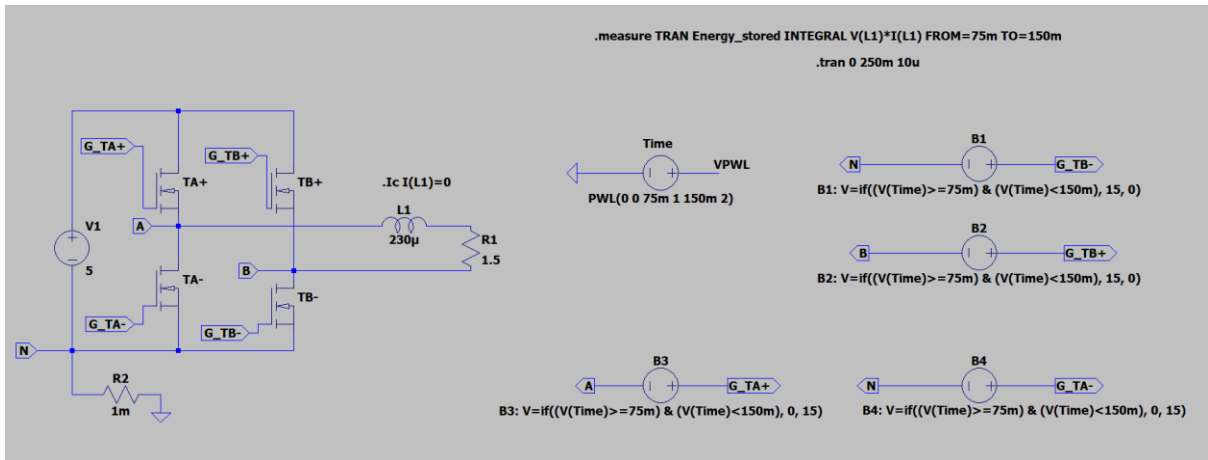


Figure 3.8.1 : LTSpice simulation of an H-bridge controlling coil energisation for EMGES storage mode

The model comprises five core elements:

1. DC Voltage Source (V1)

A constant-voltage supply is used to drive the H-bridge. In practice, this would represent a regulated DC source providing power to the coils during storing mode. The precise voltage level was selected for simulation purposes and is not representative of final hardware specifications.

2. Electromagnetic Coil and Series Resistor (L1 and R1)

The electromagnetic coil is represented as an inductor (L1) in series with a resistive element (R1), modelling both the magnetic storage characteristics and internal winding resistance. These component values are preliminary placeholders and serve to model the system response dynamically during energisation.

3. Switching Transistors

The coil is driven via an H-bridge composed of four ideal MOSFET switches:

- **TA+** and **TB-** control forward current,
- **TB+** and **TA-** enable reverse current flow.

The arrangement allows bidirectional current control and precise pulse delivery through the coil.

4. Pulse Timing Control – PWL Source (VPWL)

A piecewise linear (PWL) voltage source labelled VPWL provides a timed control signal to all gate drivers. The switching behaviour is governed by the following sequence:

- **0 to 75 ms:** No gates are activated (system idle).
- **75 to 150 ms:** All gates receive activation logic to energise the coil.
- **Post 150 ms:** All gates are disabled, representing system shutdown or transition.

5. Gate Logic Control – Behavioural Sources (B1–B4)

Behavioural voltage sources (labelled B1–B4) interpret the VPWL control voltage and deliver appropriate gate drive voltages (15 V) to the four MOSFETs:

- **B1** drives G_TB–,
- **B2** drives G_TB+,
- **B3** drives G_TA+,
- **B4** drives G_TA–.

The logic used ensures that switching only occurs during the active energisation window between 75 and 150 ms: $V=\text{if}((V(\text{Time})\geq 75\text{m}) \& (V(\text{Time})<150\text{m}), 15, 0)$

Simulation Objective

The primary objective of this simulation is to assess:

- The ability of the H-bridge to deliver bidirectional current to the coil during the active pulse window,
- The energy is stored in the coil's magnetic field during energisation.

To this end, a measurement directive is included in the netlist:

```
.measure TRAN Energy_stored INTEGRAL V(L1)*I(L1) FROM=75m TO=150m
```

This computes the total energy delivered to the inductor over the energisation period.

Control Sequence and Operation

Initial Activation (0–75 ms)

During this phase, all gates remain off, and no current flows through the coil. This models the coil in an idle or standby state.

Active Energisation (75–150 ms)

Once VPWL rises to 1 V, the behavioural gate drivers activate the H-bridge. Current flows through the coil in a defined direction, building up magnetic energy. The exact force output and current profile will be analysed in the Results section.

Deactivation Phase (After 150 ms)

At 150 ms, the VPWL voltage shifts to 2 V. This disables all gate drivers simultaneously, ceasing current flow and ending the energisation cycle. In practice, this models the release or transition to the next coil in a multi-stage lifting system.

This LTSpice simulation establishes the foundational control logic for managing coil energisation during the storing mode of EMGES. The model enables controlled pulse delivery through an H-bridge configuration, allowing bidirectional current flow and dynamic energy

input to the coil. The results obtained from this simulation will support further analysis of energy transfer, timing accuracy, and performance under scaled-up system parameters.

3.9 Chapter summary

This chapter outlined the methodology used in developing the EMGES prototype, incorporating both theoretical and simulation-based approaches to evaluate electromagnetic force generation, circuit control, and energy transfer. Key modelling efforts included the use of Ansys Maxwell to simulate force responses for 45-turn and 135-turn coil configurations, and LTSpice to model coil activation logic using a bidirectional H-bridge circuit. Coil geometry and placement were determined based on a 50% magnetic flux threshold, resulting in a 15 mm coil length to optimise coupling in storage mode. Practical constraints such as a copper fill factor of 0.8 and wire gauge limitations were also considered.

The next chapter presents the experimental results and simulation outputs, analysing system efficiency, generation-mode performance, and the impact of scaling to larger applications.

4 RESULTS, ANALYSIS & DISCUSSION

4.1 Chapter overview

This chapter details the experimental outcomes, simulations, and analytical evaluations of the EMGES prototype. It covers the results from storage mode testing at different coil locations, generation mode voltage and power outputs for both 45-turn and 135-turn coil configurations, and the validation of these results through electromagnetic simulations. Additional analysis is provided using LTSpice to explore coil activation logic and power flow behaviour. Together, these findings highlight the system's performance limitations and inform design considerations for future scaling.

4.2 Flux Distribution (Generation mode)

4.2.1 FEA Setup in Ansys Maxwell

This section presents how the finite element model in Ansys Maxwell was used to examine the magnetic flux distribution around the ring-shaped permanent magnet and coil assembly. Building on the methodology outlined previously, the model incorporated boundary conditions, mesh parameters, and a 50% flux threshold for coil height. By setting a 15 mm coil length near this threshold, it became possible to capture the most dynamic portions of the magnet's flux gradient while balancing practical constraints such as the copper fill factor.

Within this model, Ansys Maxwell generated detailed flux line visualisations and numeric outputs describing how the flux changes with distance (expressed in Wb/m) as seen in Figure 3.5.12. These flux gradient values were then used to predict the EMF through the coil, drawing on Faraday's Law of Induction as given in 3.3.2. Adopting an approach inspired by Carroll's earlier work, but adapted for the higher field intensities required in storing mode, helped ensure that the chosen coil dimensions would provide the robust electromagnetic coupling necessary for lifting the PM and weight assembly against gravity.

Preliminary Drop-Time Measurements

Prior to laboratory work, the prototype was tested in order to determine an approximate velocity for the magnets and mass as they dropped through a 0.6 m structure. Repeated trials indicated an average drop time of approximately 0.3 seconds, corresponding to a velocity of around 0.2 m/s. These values were incorporated into the theoretical model to estimate how quickly the flux through the coil would change during the magnet's descent.

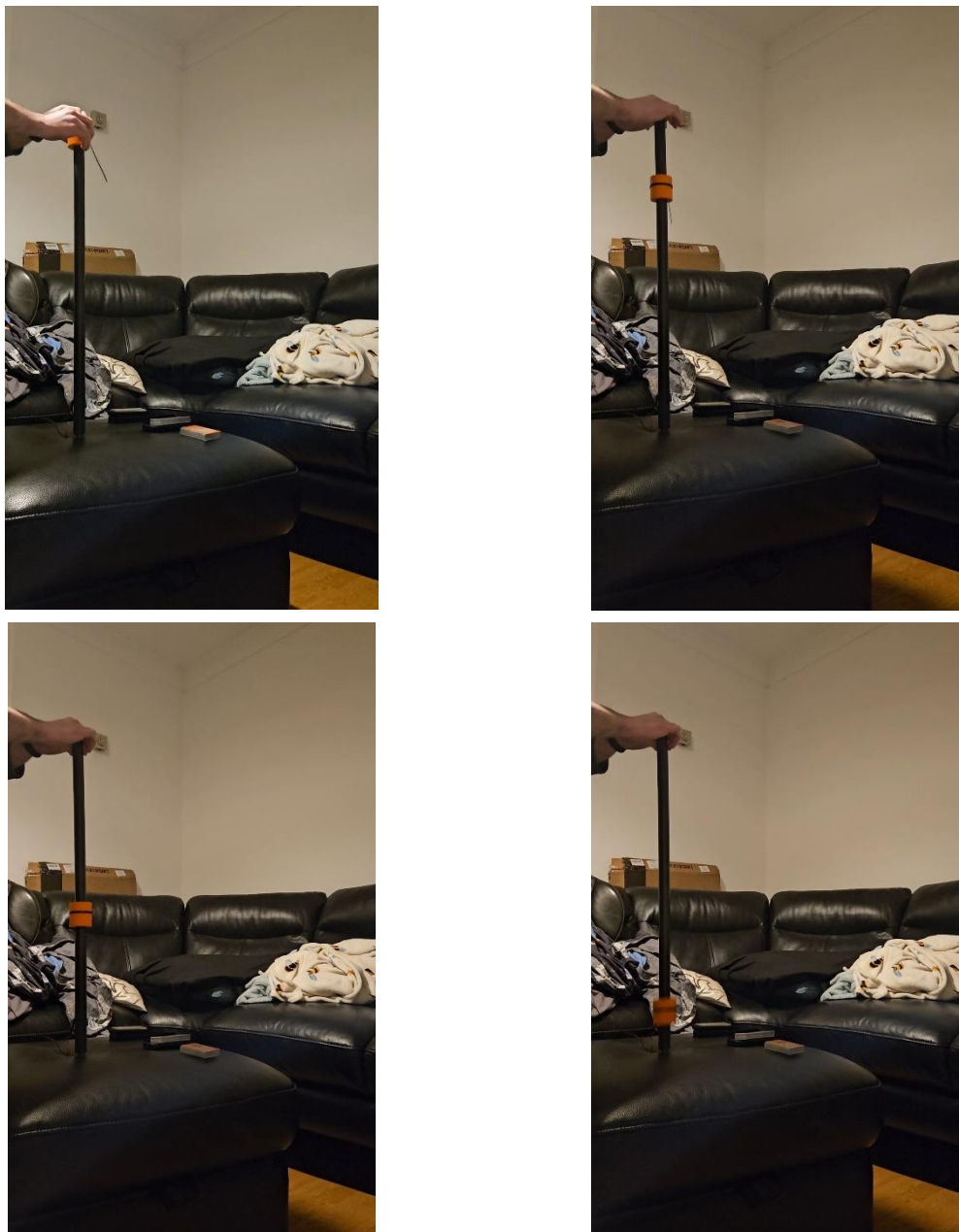


Figure 4.2.1 : Drop Test Time Collection

4.2.2 Theoretical EMF Calculations

By combining the flux gradient results from Ansys Maxwell with the measured velocity, it became possible to apply Equation 3.3.2, which states that $\varepsilon = -N \frac{d\phi}{dt}$. Since $d\phi/dt$ can be replaced by $(d\phi/dx) \cdot v$, the velocity from the drop-time trials and the flux gradient from Ansys Maxwell served as the primary inputs. Coils featuring both 45 and 135 turns were modelled at a 15 mm coil height to ascertain the impact of varying the number of turns while keeping the PMs and weight velocity constant. Plots of EMF versus magnet distance were generated and indicated an increase in voltage as the magnet approached the coil, followed by a change in polarity once it passed through. This sign change reflected the switch in magnet polarity

relative to the coil. This visually demonstrates Lenz's law, which states that the direction of the induced EMF opposes the change that produced it.

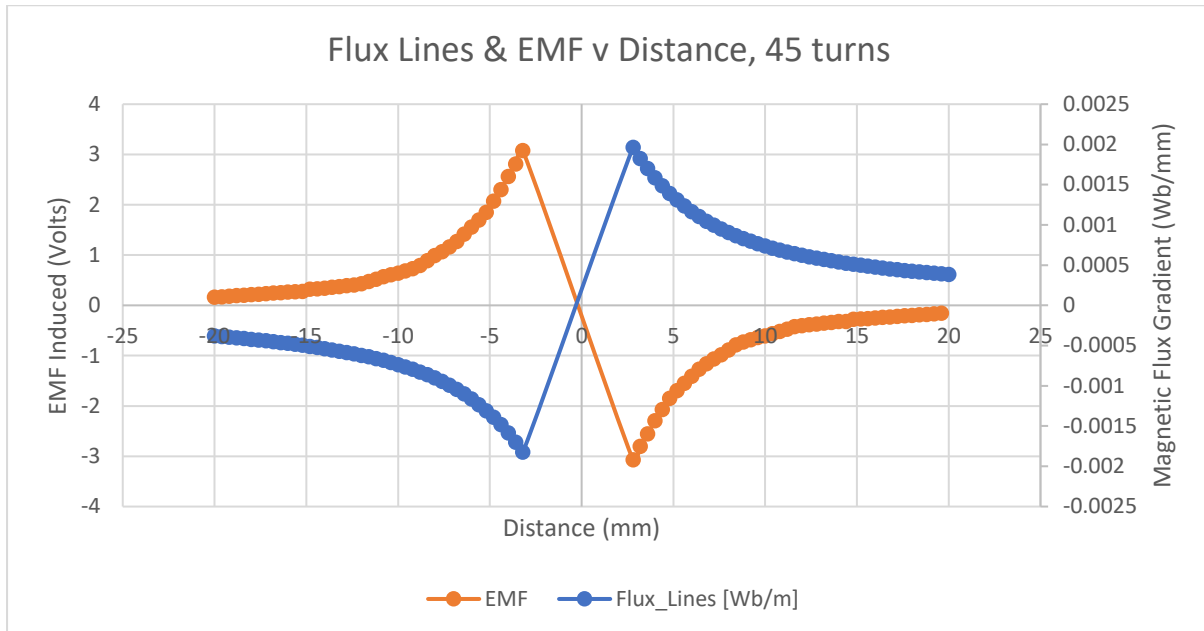


Figure 4.2.2 : EMF Induced in 45 Turn Prediction

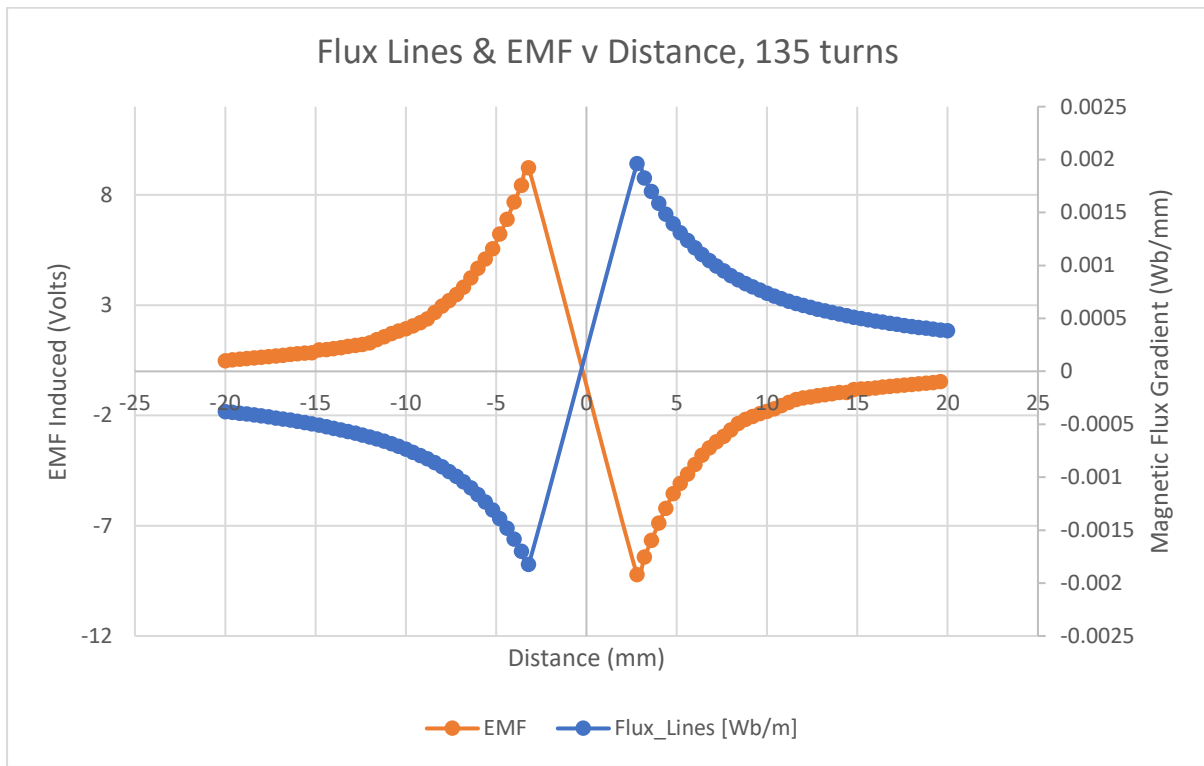


Figure 4.2.3 : EMF Induced in 135 Turn Prediction

Figure 4.2.2 focused on the 45-turn coil, illustrating a magnitude of just over 3 Volts induced. Figure 4.2.3 addressed the 135-turn coil under identical conditions, revealing that the EMF amplitude roughly tripled, consistent with the linear relationship between coil turns and

induced voltage. Although the drop-time tests were informal, the measured velocity provided enough accuracy for an accurate assessment. The predictions from these simulations and equations illustrate how the coil configuration can substantially influence voltage output in a gravity-based energy storage design.

Reflective Discussion on Flux Threshold Assumptions

Upon carefully revisiting the flux gradient findings and the prototype's performance, it became clear that the assumed threshold for coil placement was actually 50%, rather than the initially reported 25%. Although this misunderstanding arose after the experiments were conducted, it does not undermine the validity of the recorded data. The prototype coil, which operates above the 50% flux threshold, demonstrated robust electromagnetic coupling across both 45 and 135 turns, a result consistently supported by laboratory measurements. Notably, the measured EMF in generation mode was in extremely close agreement with predictions from Ansys Maxwell simulations, confirming that this higher threshold maintained adequate magnetic interaction between the coil and magnet to facilitate energy conversion.

This retrospective insight highlights the importance of accurately specifying the flux threshold during coil design, rather than negating any findings. Indeed, the consistency between theoretical and experimental EMF values showcases the effectiveness of the 50% threshold in achieving the necessary energy coupling for both storing and generating modes.

Comparing different flux thresholds underscores how coil length and flux density interplay in determining the voltage capture range. At a 50% threshold, corresponding to a 15 mm coil length, the 45-turn configuration generated voltages ranging from approximately 0.98 V to 3.075 V. Increasing the winding count to 135 enlarged this range to about 2.96 V to 9.22 V. These observations, detailed in the *Results and Analysis* section, reflect the higher flux density available at a shorter coil length and demonstrate how an increased turn count can enhance the overall voltage output.

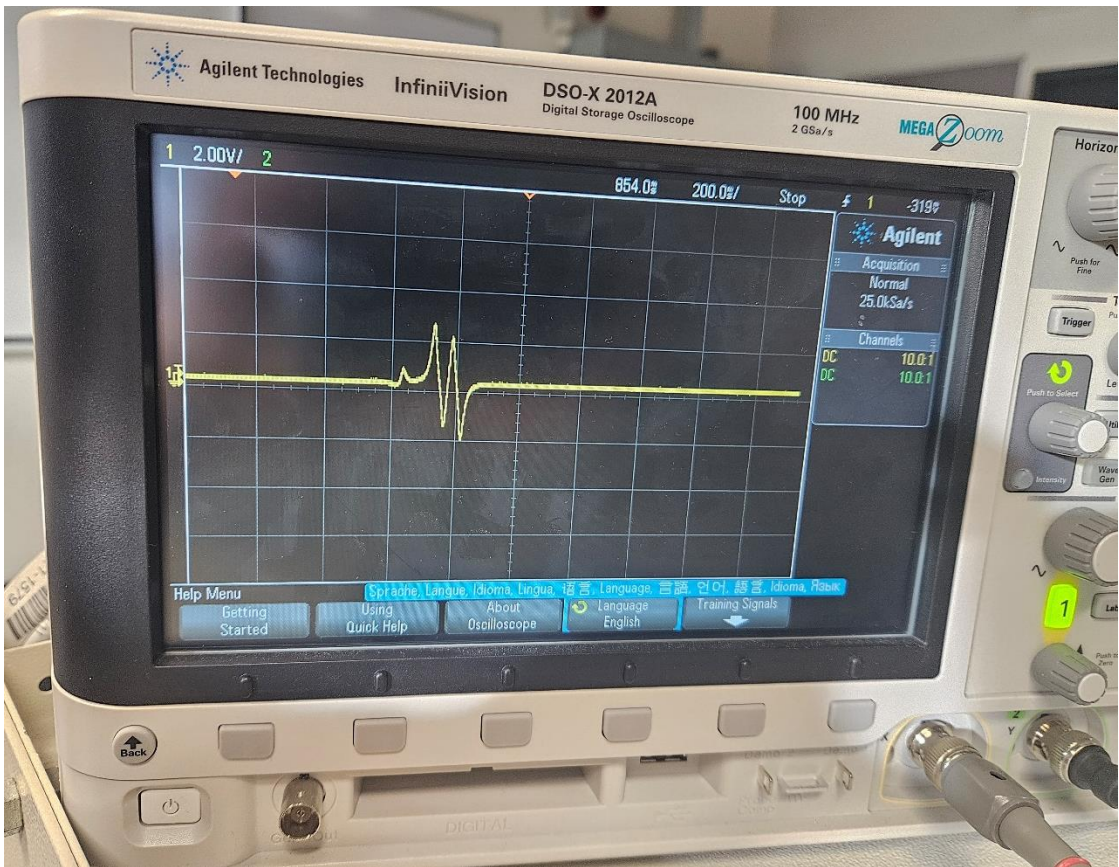


Figure 4.2.4 : Actual 45 Turn EMF Pattern for 1 Coil

By contrast, adopting a 25% threshold would demand a 30 mm coil, extending into regions of lower flux density. This modification could broaden the operational voltage range. For instance, the 45-turn coil at the 25% threshold produces a similar 0.98 V to 3.075 V interval, retaining the same lower and upper limits as the 15 mm design. More notably, the 135-turn version at 25% varies from around 0.82 V to 9.22 V, potentially improving performance in generation mode when the weight and permanent magnet traverses the coil. This wider acceptance of voltages may prove advantageous in scenarios involving fluctuating magnet velocity or slight positional misalignments.

Ultimately, the choice between a 50% and 25% threshold is a balance between focusing on a narrower, higher-flux region for stronger coupling and embracing a wider zone to accommodate a greater range of induced voltages. In practice, a broader capture range can be beneficial for dynamic energy harvesting conditions, whereas a higher threshold design can achieve more intense conversion in a smaller space. If additional time and resources were available, an experimental comparison to validate a 25% threshold using a 30 mm coil would offer valuable insight into how varying thresholds and coil dimensions influence not only electromagnetic efficiency but also manufacturability and overall system performance.

4.2.3 Comparison with Experimental Waveforms

To evaluate how closely these theoretical predictions match real-world performance, an oscilloscope capture was obtained during a physical drop test of the single 45-turn, 15 mm coil arrangement. The oscilloscope was configured so that each vertical grid division represented 2 Volts, while each horizontal division was 200 ms. The recorded voltage pattern largely coincided with the expected waveform, showing a first spike near 3 Volts corresponding to the magnet's north pole entering the coil, followed later by a negative swing as the south pole continued its transit. An initial transient bump was observed and is likely attributable to slight vibrations or electrical noise at the onset of the drop.

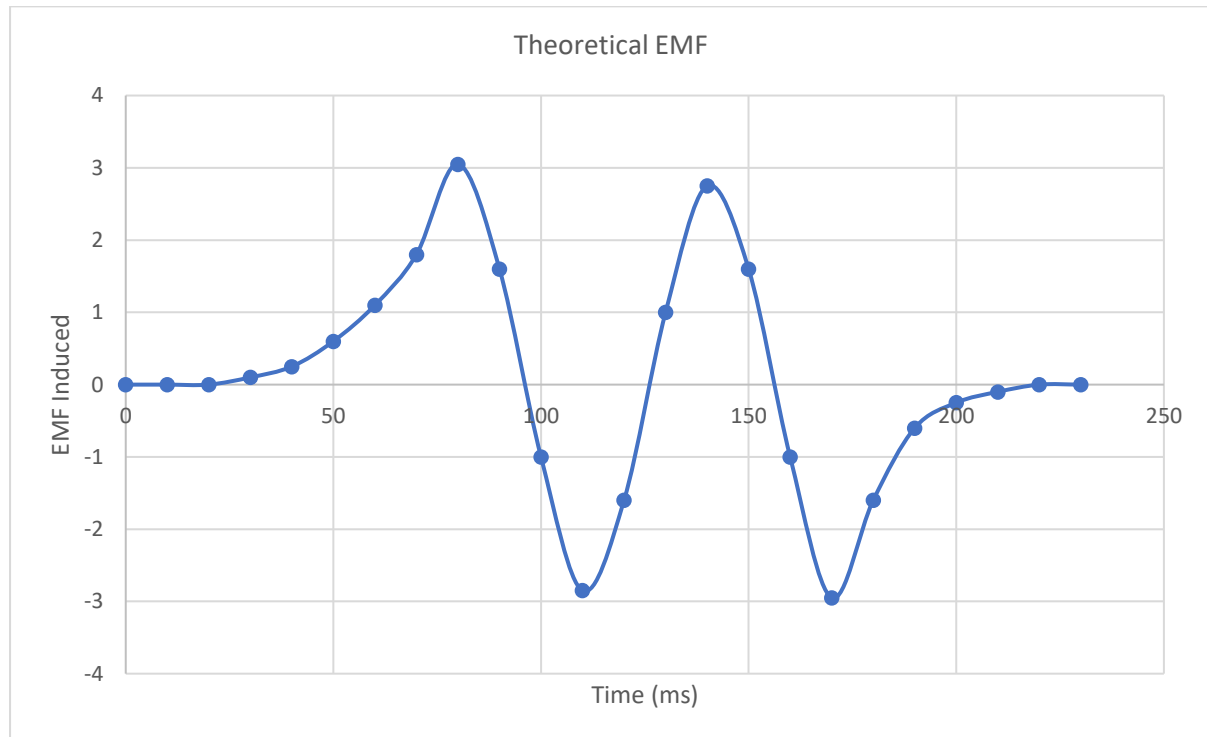


Figure 4.2.5 : Predicted EMF Pattern for 1 Coil

Eddy Current Effects

In principle, the Ansys Maxwell simulations accounted for eddy current losses, but they were found to be minimal. During experimentation, however, eddy currents in nearby conductive materials and in the coil itself had a more pronounced effect than anticipated. Even with an open-circuit measurement, these currents generated opposing fields that reduced the magnet's speed through the coil, causing subsequent voltage spikes to remain below the 3 V initially predicted. Nevertheless, the overall shape of the waveform still confirmed the polarity shifts in accordance with Faraday's Law, demonstrating how the magnet's north and south poles each induced positive or negative voltages as they crossed the coil.

Taken together, the simulation results and experimental data illustrate how coil geometry, magnet velocity, and eddy current effects all combine to determine the observed EMF. These findings validate the general theoretical approach while highlighting the importance of

factoring in loss mechanisms for more accurate performance estimates in a gravity-based energy storage system.

4.3 Magnet v Iron Core Position

A key observation in this study is that each permanent magnet has a specified pull force of 20 kg on its surface. Practically, this corresponds to approximately 196 N when it contacts or closely approaches a ferromagnetic object, such as the iron core. When two identical magnets of the same cross-sectional area are used, each magnet independently exhibits the same pull force on a ferromagnetic material. Because of their similar geometry, the force is not simply doubled by combining two magnets in parallel; instead, each magnet has its own attraction region that similarly exerts around 20 kg of pull.

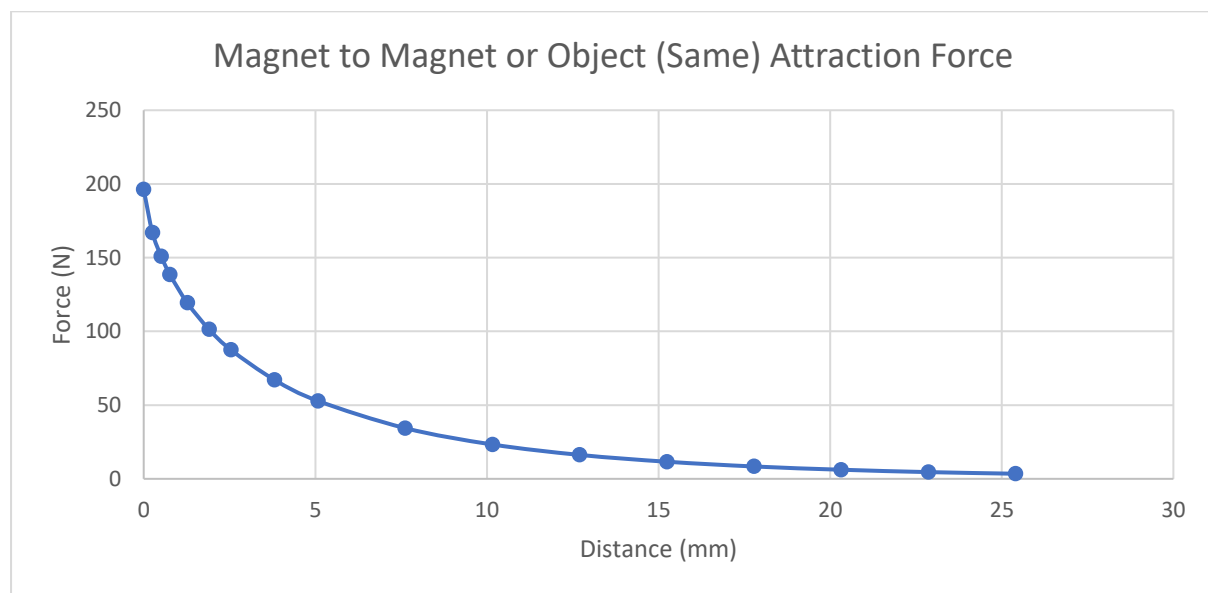


Figure 4.3.1 : Magnetic Force of Attraction vs Distance

Figure 4.3.1 above illustrates how the force of attraction decreases as the separation between the PM and ferromagnetic surface increases. Initially (at zero distance), the force measured is around 196.2 N, which aligns with the nominal 20 kg pull rating. As the gap between the magnet and ferromagnetic material grows, the force gradually diminishes. For instance, at 3.81 mm of separation, the force drops to approximately 67.14 N, and it falls further to around 3.45 N at 25.4 mm. This decline follows the general principle that magnetic attraction weakens with distance, especially in an axially magnetised magnet where the north and south poles reside on opposite circular faces.

4.3.1 Ring Magnet

To ensure accurate simulation results, all components in Ansys Maxwell were modelled along the same central z-axis. This alignment minimised the net forces in the x and y directions, allowing the solver to converge with negligible error. Under the constraints of the student version of Ansys Maxwell, the global error could only be reduced to approximately 0.6%. This

level of convergence was sufficient to demonstrate that, in an ideally centred arrangement, the magnet experiences minimal off-axis pulling forces.

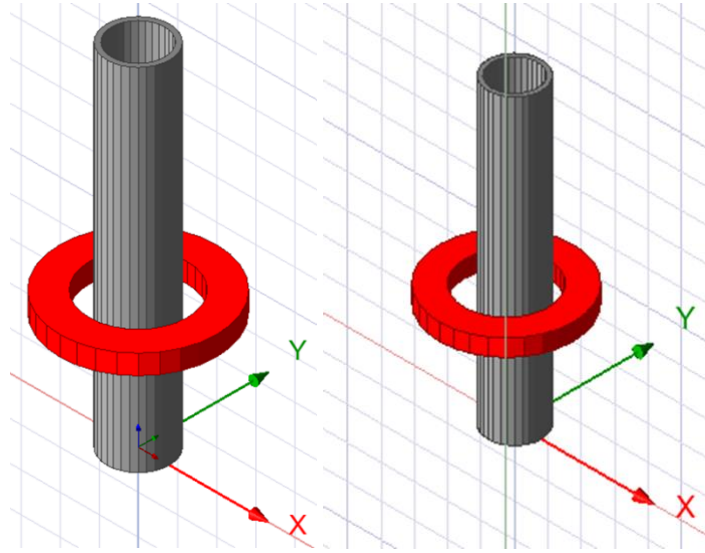


Figure 4.3.2 : PM and Iron Core z-axis Alignment and Misalignment

However, a subsequent test was conducted by displacing the magnet 2.5 mm off-centre (in the x-axis) relative to the iron core. In this scenario, the solver reported an increased net force of approximately -7.1164 N (where the negative sign denotes the direction towards the core). Despite the core itself experiencing an equal and opposite force, it remains stationary, so the magnet assembly is compelled to shift laterally. Notably, this lateral attraction far exceeds the gravitational force acting on the magnet and attached weight in storing mode, preventing them from falling freely in generation mode. Consequently, maintaining precise alignment within the apparatus is essential to avoid undesired sideways motion that could compromise both the energy storage and generation processes.

Figure 4.3.3 depicts the measured increase in lateral force (along the x-axis) as the PM is incrementally displaced from the central z-axis towards the iron core. The trend clearly indicates that even a minor offset in alignment can lead to a pronounced lateral pull, which becomes particularly significant at smaller separations. This increase arises from the intensifying magnetic flux density in the narrow gap between the PM and the ferromagnetic core, effectively amplifying the off-axis attraction whenever the magnet is not perfectly centred.

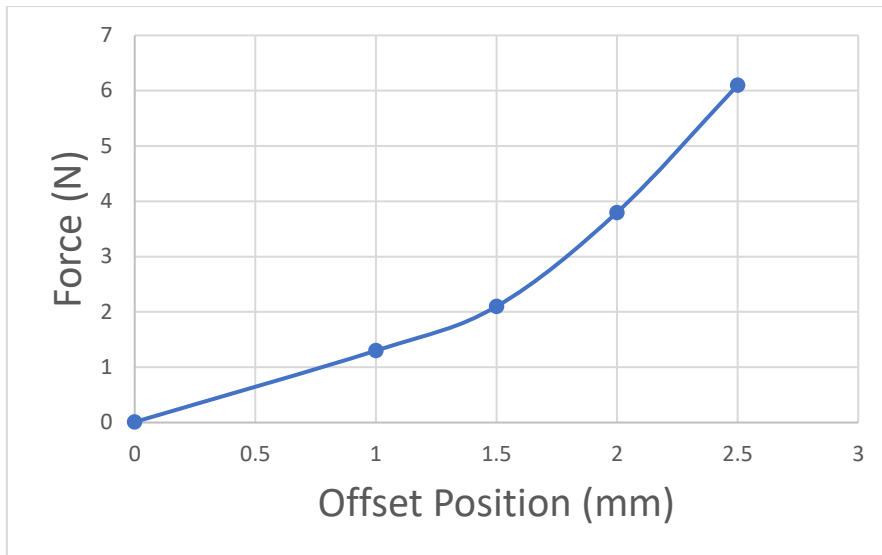


Figure 4.3.3 : Force vs Alignment Offset Ring Magnet

In practice, maintaining perfect alignment between the PM and the iron core proved challenging during the prototype assembly. Despite meticulous efforts to position the PM, iron core and surrounding support structures along a common z-axis, slight deviations in the build process and small manufacturing tolerances tended to shift the magnet off-centre. During testing, it was evident that as the magnet drew closer to the iron core, the lateral pull became increasingly pronounced, making it difficult to keep the assembly aligned by hand. Although a calibrated spring force meter was not employed to measure this effect quantitatively, there was a discernible and substantial attraction towards the ferromagnetic core whenever the PM was situated even a few millimetres off-axis.

These observations align with the simulation results, confirming that lateral forces can pose significant challenges in a gravity-based energy storage system. Even minor misalignments can introduce unwanted sideways motion, potentially compromising the system's efficiency and stability. Hence, careful mechanical design and robust guiding strategies are essential to ensure that the magnet assembly remains axially centred, thereby minimising the risk of off-axis attraction and preserving the intended performance of both the storage and generation processes.

4.3.2 Disc Magnet

To further investigate the influence of lateral misalignment on magnetic behaviour, a comparative analysis was carried out using a 5 mm radius, 5 mm thick disc-shaped permanent magnet placed concentrically inside the iron core. The disc magnet shared the same magnetic properties as the ring magnet used in the earlier external positioning analysis, allowing for a direct comparison. In the initial simulation, the centre of the disc magnet was aligned precisely with the centre of the iron core at position (0, 0, 0). Under this ideal condition, the lateral force along the x-axis was negligible, recorded at just 0.01588 N. This result confirmed that the system, when perfectly centred, experiences minimal off-axis loading, preserving axial symmetry in the magnetic field distribution.

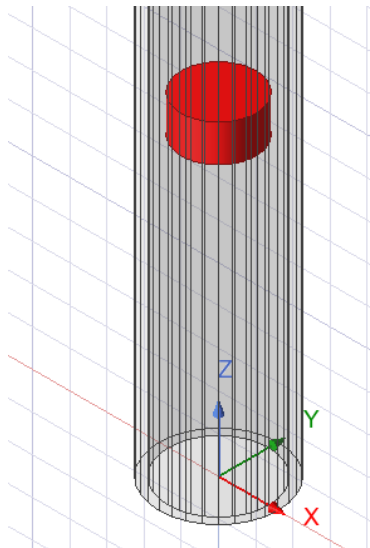


Figure 4.3.4 : Disk PM Inside Iron Core

As the disc magnet was incrementally displaced in the x-direction by 0.25 mm intervals, the lateral force increased rapidly. At 0.25 mm offset, the x-axis force reached 0.95863 N, and at 0.5 mm offset it rose to 1.979 N. When displaced by 1 mm, the lateral force became significant at 4.4326 N, and at 1.5 mm, it peaked at 8.3647 N. In all instances, the forces in the y- and z-axes remained minor compared to the dominant x-axis component. This pronounced increase in lateral attraction is attributed to the enhanced magnetic flux concentration inside the enclosed core geometry, which intensifies as the PM's centre diverges from the iron core's central axis.

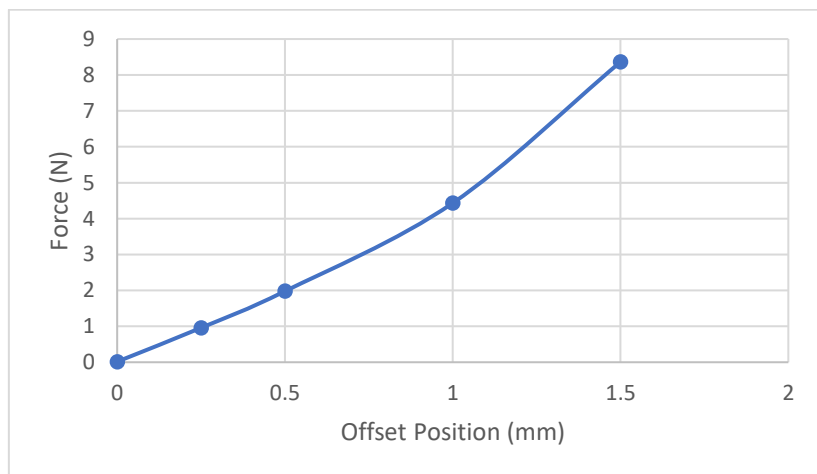


Figure 4.3.5 : Force vs Alignment Offset Disk Magnet

When compared to the ring magnet configuration analysed previously—where the PM is positioned externally adjacent to the core—this internal disc magnet setup demonstrated a substantially higher sensitivity to misalignment. For instance, at a 1 mm lateral offset, the disc magnet generated a force of 4.4326 N compared to 1.3 N for the ring magnet. At a 1.5 mm offset, the discrepancy widened further, with the disc magnet producing 8.3647 N while the ring magnet produced only 2.1 N.

This comparison highlights a critical design consideration: the ring magnet configuration provides greater tolerance for mechanical misalignment. Its broader magnetic footprint and lower off-axis sensitivity make it a more stable and forgiving choice in practical applications where perfect alignment is difficult to maintain. The reduced lateral forces also minimise the risk of the magnet veering off-track during operation, thereby enhancing system reliability in both storing and generation modes.

4.4 Coil & PM Zones of Interaction (Storage mode)

4.4.1 System Weight, Force Requirements & Area of Interaction

The total force that must be overcome to lift the system in storing mode includes both the attached weight and the magnetic components. The primary load consists of a 2.0 N mass and two PMs, each contributing approximately 0.1 N of gravitational force, bringing the total system weight to 2.2 N. This defines the minimum net upward force that must be achieved through electromagnetic attraction.

To accomplish this, the design employs a multi-coil lifting strategy in which four coils are active at any given moment along the lift path. This distributed actuation approach significantly reduces the magnetic force each individual coil must generate. Rather than requiring a single coil to produce 2.2 N, the load is shared equally, meaning each coil must supply a minimum of 0.55 N to maintain equilibrium and enable vertical lift. This design also allows for lower individual current requirements and reduces stress on individual coils, leading to improved thermal and electrical efficiency.

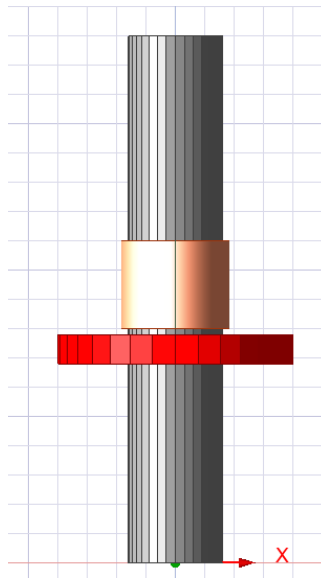


Figure 4.4.1 : Single PM and EM Setup for Force Analysis

A full 3D electromagnetic simulation environment was constructed in Ansys Maxwell to closely replicate the physical arrangement and operation of the prototype as seen in Figure 4.4.1. This included accurate geometric modelling of the iron core, copper coils, and PM

positioning. The aim was to analyse the spatial distribution of magnetic flux density B and validate the assumptions used in the theoretical force and ampere-turn calculations.

As mentioned previously, while Ansys Maxwell offers a transient motion solver, it was found to be unsuitable for this application due to convergence issues when attempting to simulate continuous motion of the PM through the coil. As a result, an alternative approach was adopted: the PM was incrementally repositioned in 1 mm steps over a 10 mm travel distance, and separate static simulations were executed at each position. This method, though time-consuming, allowed for detailed flux density and force data to be extracted across the full interaction zone between the PM and the EM.

The simulation results confirmed that the magnetic field is most attracted to the face of the iron core, particularly along the central axis and immediately adjacent radial zones. These findings supported the decision to define a conservative area of interaction equal to the physical cross-sectional area of the core. This assumption was then applied in all theoretical calculations of flux density B , magnetic force, and ampere-turn requirements to avoid overestimating the effective force generation capabilities of the electromagnet.

4.4.2 Selection of Coil Position Lines

To characterise how the PM interacts with the electromagnetic field at different lateral offsets, three distinct lines were defined and analysed within the Ansys Maxwell 3D simulation environment. These lines were selected to capture a range of realistic alignment scenarios that may occur due to manufacturing tolerances, lateral displacement during motion, or intentional design offsets between the coil and the PM. Each line was defined in the z-direction, corresponding to the direction of vertical travel, and extended over a 30 mm range, comprising 7.5 mm prior to the coil, 15 mm across the full coil height, and 7.5 mm beyond the top of the coil. This provided sufficient resolution to capture the full spatial profile of flux interaction during coil traversal.

- Line 1 was positioned along the central axis of the coil, both in the x- and z-directions. This line passed through the coil's magnetic centre, located at 8.3 mm in the x-direction, and represented the ideal case of perfect alignment between the PM and the electromagnet. It was expected that this position would yield the strongest magnetic coupling and require the least amount of current to achieve the necessary lifting force.
- Line 2 was defined along the inner radius of the PM, situated at 12.5 mm from the PM's centre. This placed it approximately 4.2 mm laterally offset from the coil's central axis. This line intersected the edge of the core's magnetic field and represented a more realistic alignment case, where the PM may not be perfectly centred due to movement or structural clearance.
- Line 3 corresponded to the centre of the PM's active magnetic surface, positioned between the PM's inner radius (12.5 mm) and outer radius (20 mm). This placed the line approximately 8 mm offset from the coil axis. It represented the lowest coupling

case among the three and served to evaluate the electromagnet's ability to produce sufficient force even under unfavourable alignment conditions.

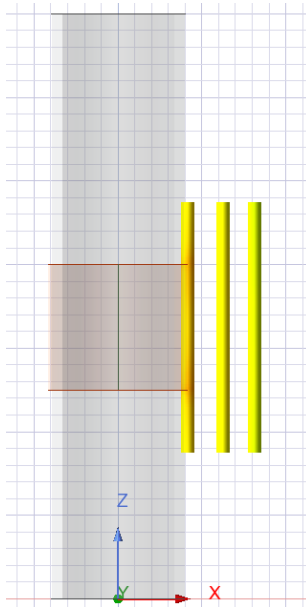


Figure 4.4.2 : Magnetic Flux Density on each line

These three lines were selected to reflect the range of magnetic coupling likely to be experienced in practice and to assess how the system's performance degrades with increasing lateral offset. The magnetic flux density generated along each line was extracted from the Ansys Maxwell simulations and later used to determine the ampere-turn (AT) requirements necessary to achieve a minimum lifting force of 0.55 N at a consistent 3 mm vertical separation between the coil and the PM.

This methodology allowed for a direct comparison between ideal and non-ideal alignment cases and informed design decisions regarding coil current control, alignment tolerances, and mechanical positioning of the PM within the lift system.

4.4.3 Ampere-Turn Analysis and Force vs Distance Behaviour

The analysis of electromagnetic force generation was conducted by exploring a range of AT configurations, with the objective of identifying the required magnetic field strength to produce a force of at least 0.55 N. This value represented the necessary lifting force per coil, based on a total system weight of 2.2 N and the assumption that four coils would be active simultaneously to distribute the load evenly along the vertical structure.

The primary set of results presented in this thesis focused on a coil comprising 135 turns with a coil height of 15 mm. This configuration was chosen to maintain consistency with the physical prototype, which was constructed to these specifications. However, several other AT configurations were also tested in simulation to verify the accuracy of the AT analysis and to evaluate the influence of varying the number of turns on current requirements. Simulations were conducted for coils with 225, 270, and 360 turns. In each case, the current was adjusted to achieve the required AT values that generated the required force to propel the PMs and weight upwards across the three defined interaction lines. These additional cases confirmed

the expected trend that increasing the number of turns allows for a reduction in current to achieve the same magnetic field strength, though at the cost of higher coil resistance and increased inductance.

The ampere-turn values presented were derived through a combination of simulation and analytical modelling. In Ansys Maxwell, static simulations were performed in which both the number of turns and the coil current were varied. The resulting magnetic flux density (B) was exported along each of the three predefined lines: Line 1 (coil centre), Line 2 (4.2 mm offset), and Line 3 (8.0 mm offset). For each configuration, the B field was extracted at a vertical separation of 3 mm between the coil and the PM, and imported into Excel for further processing [71].

From these B field data, the force exerted on the PM was calculated using Equations 3.3.10 and 3.3.11. These equations model the force of attraction between two magnetic bodies by incorporating the superposition of magnetic flux densities from the EM and PM, along with the conservative area of interaction defined by the cross-sectional face of the iron core. This approach ensured that force estimates remained realistic and avoided overestimation due to flux fringing or localised field intensities.

The AT values required to achieve a lifting force of 0.55 N at a 3 mm separation varied significantly with position. For Line 1, located at the centre of the coil (8.3 mm in the x-direction), an AT value of 140 was sufficient, corresponding to a current of approximately 1.04 A with 135 turns. For Line 2, at a 4.2 mm offset (aligned with the PM's inner radius at 12.5 mm), the required AT increased to 238, demanding a current of 1.76 A. For Line 3, at an 8.0 mm offset from the coil axis, an AT of 374 was necessary, resulting in a current of 2.77 A for the same number of turns.

This variation in ampere-turn requirement across different lateral offsets demonstrated a clear relationship between magnetic coupling efficiency and the PM's distance from the centre of the coil. Each of the three lines analysed—Line 1, Line 2, and Line 3—was offset by approximately 4 mm in the x-direction from the previous, resulting in a spacing pattern of roughly 0 mm, 4 mm, and 8 mm from the coil centre. This provided an opportunity to observe how AT demand scales with horizontal displacement.

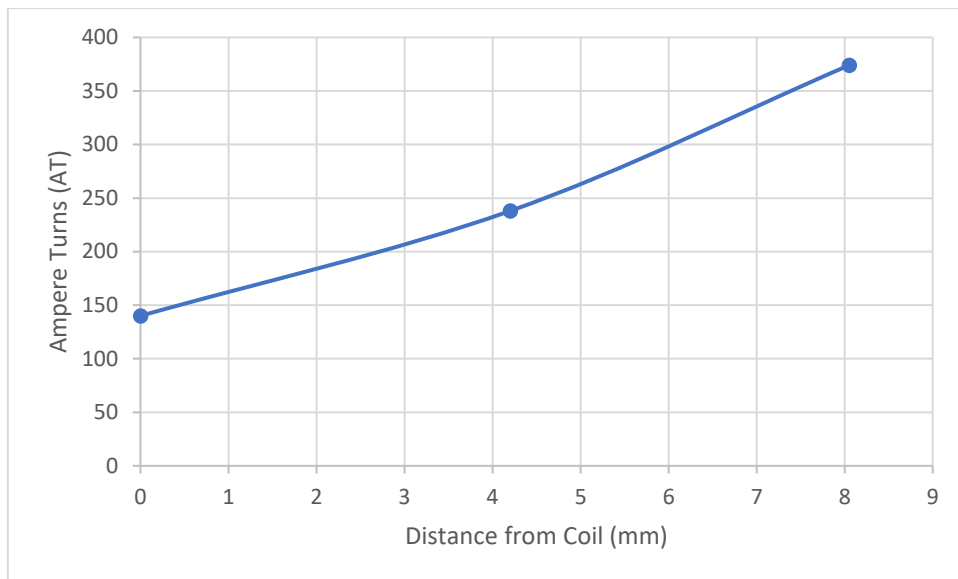


Figure 4.4.3 : Ampere-Turns vs Lateral Distance from Coil

As shown in Figure 4.4.3, the ampere-turns required to maintain a constant 0.55 N lifting force at a fixed vertical separation of 3 mm increased in a non-linear but approximately quadratic fashion with increasing distance from the coil. Between Line 1 and Line 2 (a 4 mm offset), the required AT increased from 140 to 238—an increase of 98 AT. Between Line 2 and Line 3 (a further 4 mm offset), the AT requirement rose to 374—an increase of 136 AT. This corresponds to an average rate of increase of approximately 110 AT per 4 mm of lateral distance.

This trend reflects the natural decline in flux density with increasing distance from the centre of the coil, as the magnetic field becomes more diffuse and fringing effects dominate. These findings support the importance of maintaining close alignment between the coil and PM where possible, or compensating for lateral misalignment by increasing current when higher offsets are unavoidable.

It was observed that each of the three line locations exhibited a similar structural pattern in their force–distance plots, despite significant differences in magnitude. This pattern consisted of a sharp increase in force as the PM approached the coil under constant current conditions, a local maximum when the PM was aligned with the centre of the coil in the z-axis, a reduction in force as the PM passed through the coil centre, and a second peak at the far end of the coil before falling off as the PM moved away.

As shown in Figure 4.4.4, the force along Line 1 increased rapidly to a peak of **0.936 N** when the PM was directly aligned with the coil’s centre due to a constant current being applied. This was followed by a dip and secondary peak before falling below the 0.55 N threshold beyond the coil region.

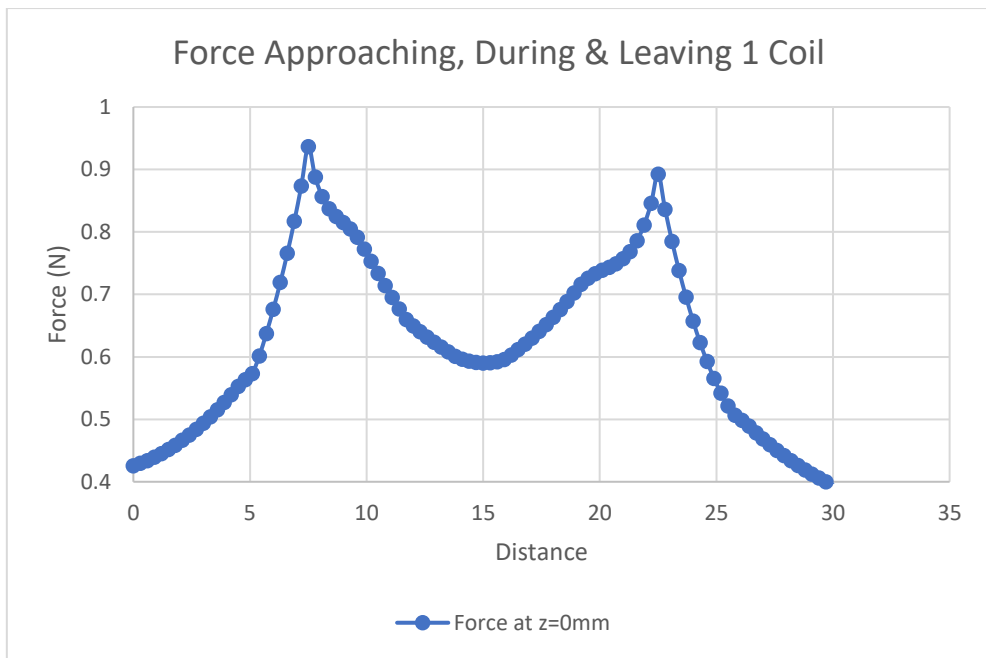


Figure 4.4.4 : Force vs Distance Plot for Line 1

Line 2 exhibited the same general force structure, albeit with a reduced peak force of **0.604 N**. The rate of increase and the difference between the force peaks and troughs were both more gradual compared to Line 1, consistent with the lower coupling efficiency further from the magnetic centre.

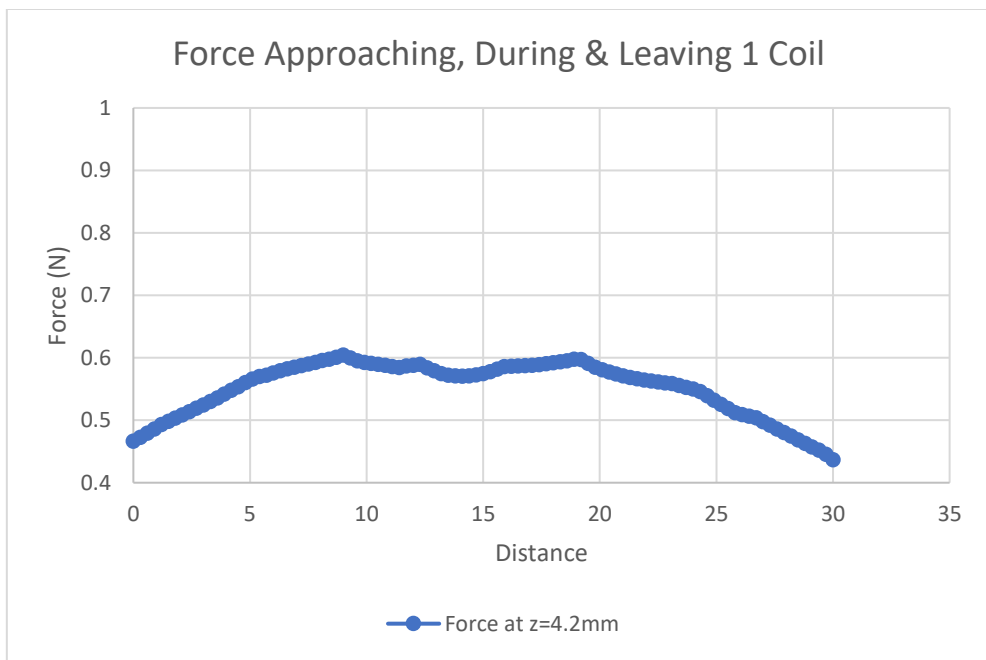


Figure 4.4.5 : Force vs Distance Plot for Line 2

Similarly, Line 3 showed the same dual-peak structure, but with a peak force of **0.601 N**. The variation in force along the travel distance was also less pronounced, reflecting the further decay of flux density at greater lateral offsets.

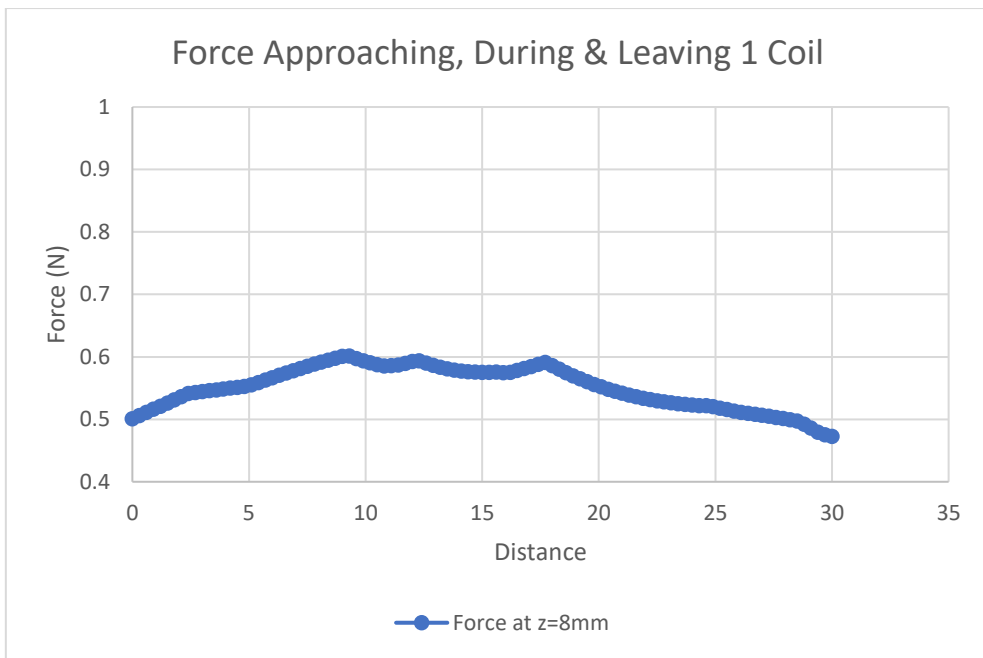


Figure 4.4.6 : Force vs Distance Plot for Line 3

These plots highlighted that, although the same qualitative magnetic behaviour was observed across all three lines, the performance varied significantly with position. The data further justified the use of positional current modulation in the control system, as different line positions would require different current profiles to maintain effective and efficient lifting across the entire structure.

These results clearly demonstrated the sensitivity of magnetic coupling to lateral displacement. As the PM moved away from the coil centre, greater ampere-turns were required to maintain the same level of magnetic attraction. This behaviour informed both the control strategy—where current is modulated to suit the PM position—and the coil layout, ensuring that the electromagnetic system could maintain lifting performance across realistic alignment tolerances.

4.4.4 Comparison Between 3D Ansys Maxwell Simulation and Line-Based Force Calculations

To further evaluate the electromagnetic force characteristics and validate the ampere-turn analysis described in Section 5.4, a full 3D simulation model was constructed in Ansys Maxwell. This model was configured using the same coil dimensions used in previous analyses—135 turns, 15 mm coil height, and 1.04 A current—and was intended to more closely reflect the physical prototype setup.

The simulation was run using 1 mm vertical increments of the permanent magnet's position relative to the electromagnet, and the resulting force values were recorded along the z-axis. The output is summarised in the table and visualised in the graph below.

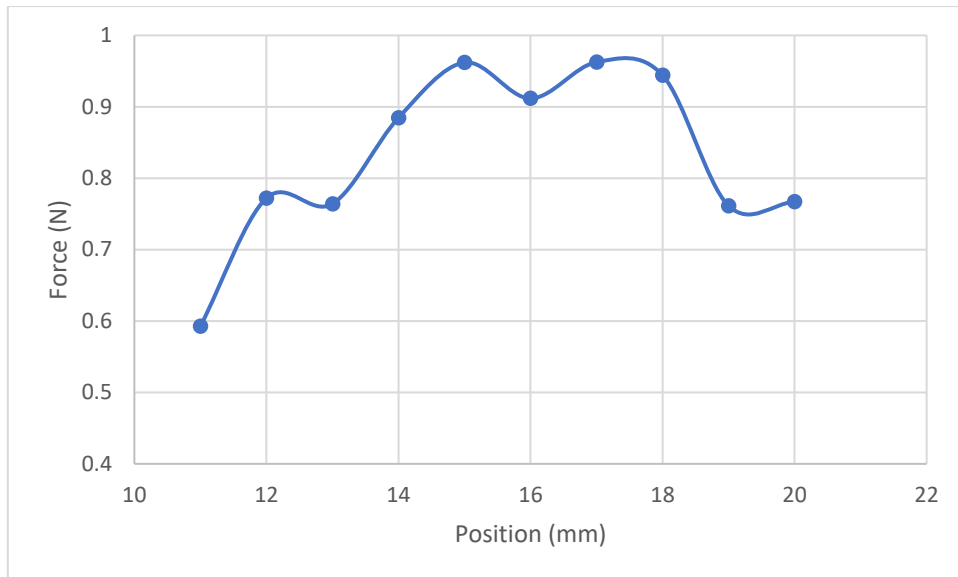


Figure 4.4.7 : 3D Simulation Force Output ($N = 135$, $I = 1.04$ A)

As seen in the results, the peak force recorded was 0.9626 N, occurring at 17 mm (2mm past the EM end). This value is significantly greater than the forces calculated in the 2D line-based analysis, where Line 1 required 140 ampere-turns to produce only 0.55 N of force at a 3 mm separation. Across the full 10 mm vertical span recorded, the simulated forces remained relatively high, ranging between 0.59 N and 0.96 N, indicating a generally strong electromagnetic interaction.

The behaviour of the force curve in the 3D simulation raises some important concerns. Based on standard magnetic theory and prior analytical modelling, it was expected that the force experienced by the permanent magnet would increase as it approached the electromagnet, due to the intensifying interaction between the PM's magnetic field and the EM's field. This force would typically peak when the PM and EM were axially aligned, with their magnetic pole faces overlapping, and then decrease symmetrically as the PM continued past the coil. This anticipated profile reflects the fundamental behaviour of magnetic attraction, where proximity strongly amplifies the net force.

Instead, the force fluctuated inconsistently—rising from 11 mm to a peak at 15 mm, decreasing slightly, and then peaking again at 17 mm, before gradually declining. This non-monotonic force profile, with irregular peaks and troughs, contradicts the expected magnetic response and suggests potential limitations in how the 3D solver modelled this particular configuration or its boundary conditions. Notably, 15 mm marks the point where the top of the PM is aligned with the bottom of the EM, a position where the force should peak as the PM moves closer under constant current conditions.

For this reason, the results from the 3D simulation were treated with caution. While they confirm that a high force can be generated with 135 turns at 1.04 A, the inconsistency in the force–position relationship suggests that the solver may not be accurately capturing the dynamic nature of the magnetic coupling or the spatial superposition of the magnetic fields.

Possible contributing factors include mesh limitations, overly simplified motion assumptions, or non-ideal boundary effects in the 3D model.

In contrast, the line-based analysis provided a smoother and more predictable force-distance curve, in line with theoretical expectations derived from superposition and flux gradient calculations. The line model better reflected how the force increased as the PM approached, peaked at alignment, and decreased as it passed the coil. For these reasons, the line-based results were considered more reliable for informing the control strategy and force calculations used in later sections.

4.4.5 Acceleration and Velocity Calculation

The motion of the permanent magnets and attached weight during the lifting phase was examined by translating force data into acceleration, velocity, and time of flight. This analysis was performed to understand how the system transitions from rest into steady-state vertical motion under electromagnetic actuation. The motion profile was derived from discrete points along the PM's vertical travel path, using simulation data collected at 0.3 mm intervals.

At each recorded point, the **net force** acting on the system was determined by subtracting the gravitational force from the total electromagnetic force. The system's mass was known to be 0.224 kg, corresponding to a total gravitational force of approximately 2.2 N. Using Newton's Second Law:

$$a = \frac{F_{net}}{m} \quad 4.4.1$$

The acceleration of the system at each position was calculated directly. This provided a pointwise understanding of how the EM force translated into vertical motion.

Once acceleration was known, the velocity at each distance increment was calculated using the kinematic relation:

$$v_f^2 = v_i^2 + 2a \times \Delta x \quad 4.4.2$$

where v_i was the velocity at the previous position and Δx the displacement interval (0.3 mm). The average velocity between two points was then used to estimate the **time elapsed**:

$$t = \frac{v_f - v_i}{a} \quad 4.4.3$$

Through this iterative process, a full velocity and time profile was constructed across the initial acceleration region of the motion.

The first three increments, covering a total vertical travel of 0.9 mm, marked the transition from rest to motion. The initial electromagnetic force of 0.002464 N produced an acceleration of 0.11 m/s^2 , resulting in a velocity of 0.002569 m/s after the first interval. In the second interval, a force of 0.013 N yielded an acceleration of 0.058 m/s^2 , with a resulting velocity of

0.006434 m/s. The third interval, at a force of 0.0224 N, led to an acceleration of 0.1 m/s² and a final velocity of 0.01007 m/s.

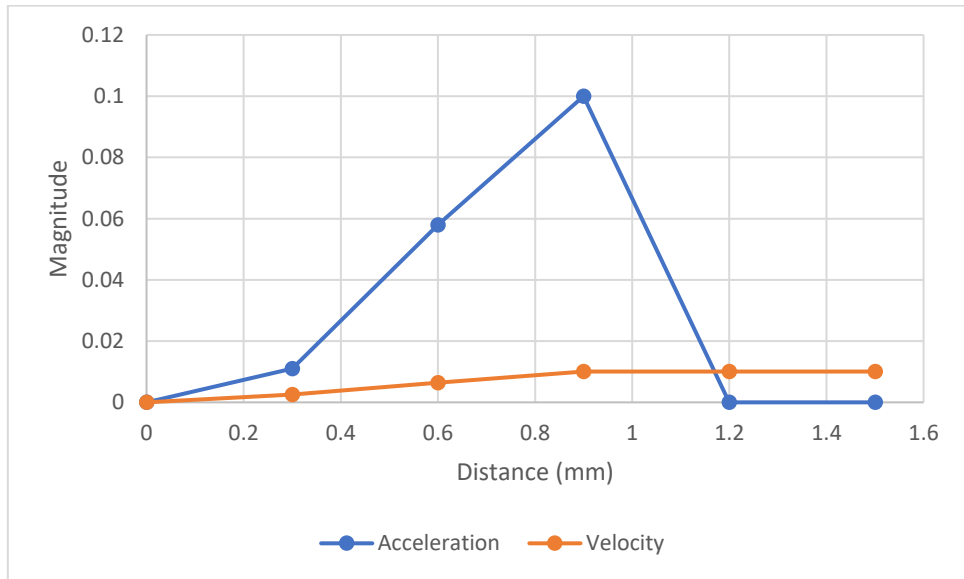


Figure 4.4.8 : Acceleration and Velocity vs Distance

From this point forward, a constant velocity regime was assumed based on the AT analysis. To maintain this velocity, the electromagnetic force at each coil needed to exactly counteract the gravitational force acting on the system, resulting in net zero acceleration. This was achieved by modulating the coil current to maintain a consistent lifting force of 0.55 N per coil.

This approach offered two primary advantages: it simplified timing coordination between sequential coil activations, and it reduced the risk of overshoot or instability that might result from uncontrolled acceleration. The control strategy, therefore, shifted from initial acceleration management to force balancing as soon as the desired velocity was achieved.

This section laid the groundwork for developing a practical control system based on both position-dependent current modulation and coil-switching logic. By mapping force data into acceleration and time domains, the dynamic behaviour of the system could be fully characterised and used to inform hardware implementation.

4.4.6 Time of Flight and Motion Control

Following the derivation of velocity from force and acceleration data, the full time of flight for the PMs and weight was calculated based on a constant velocity profile. This value was essential for defining the timing intervals required for sequential coil activations in generation mode.

As established in Section 4.4.4, the system transitioned from a short acceleration phase to a steady-state velocity of approximately 0.01007 m/s. The total lift height of the structure was 0.6 m, with the first 0.9 mm dedicated to acceleration and 15mm dedicated to the first coil. The remaining 0.5841 m was traversed at constant velocity, resulting in a time of flight of approximately 58 seconds.

When combined with the initial acceleration duration (~ 0.34 seconds), the total time of flight was approximately 58.34 seconds.

Unlike a simple model where coils would be evenly spaced with no overlap, the actual design adopted a more refined approach to ensure consistent magnetic force across the full range of PM motion. Each coil was designed to be 15 mm in height, with 3 mm vertical spacing between coil ends. This spacing strategy resulted in an overlap between adjacent coils and ensured that both the north and south poles of the PM were always within 3 mm of 4 active coils. This design was necessary to consistently deliver the required electromagnetic force to achieve net zero acceleration and maintain constant upward velocity.

As a result, a total of **nine overlapping coils** are seen in Figure 4.4.9 used along the active lift section of 39mm. One additional coil was positioned at the bottom of the structure but remained inactive during generation mode, serving only as a lower mechanical stop point.

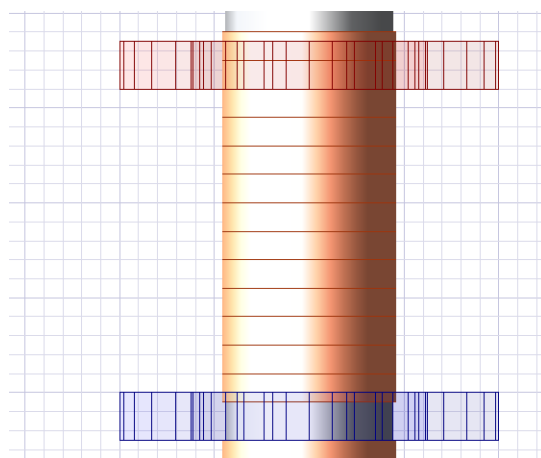


Figure 4.4.9 : Overlapping Coil Segment

Due to the overlapping arrangement, the coils did not need to switch in large intervals. Instead, the control strategy could activate or deactivate one coil at a time, every 3 mm of vertical PM movement, as long as 4 coils remained active at any one time. At a velocity of 0.01007 m/s, this corresponded to a coil-switching interval of approximately 0.298 seconds. This meant that every 298 milliseconds, one coil would be switched off as the PM moved out of range, and the next would be activated as it came into range. This staggered and overlapping switching sequence ensured a smooth transition of force application, eliminated discontinuities in net force, and allowed for constant velocity motion throughout the generation cycle.

The coil layout and overlapping configuration, as visualised in Figure 5.6.1, were thus fundamental in enabling stable, controlled lift operation. By ensuring that at least one pole of the PM was always within range of a coil, the system achieved consistent magnetic interaction and simplified the timing logic for current modulation and activation control.

4.4.7 Inductance and Fixed Turn Design Choice

The decision to fix the number of turns per coil at 135 was made following an evaluation of the trade-offs between magnetic field strength, electrical response time, and practical

construction constraints. One of the key considerations in this decision was the impact of coil inductance on the system's ability to respond quickly to changes in current, particularly in a setup that relied on regular coil switching to maintain consistent force application during constant velocity motion.

Inductance L in a coil is directly related to the number of turns squared, $L \propto N^2$

An increase in the number of turns enhances the magnetic field for a given current, which is desirable for maximising lifting force. However, it also leads to a proportional increase in inductance. High inductance values can introduce delays in current ramp-up and ramp-down times, due to the voltage–inductance relationship:

$$V = L \frac{dI}{dt} \quad 4.4.4$$

In this system, where coils are activated and deactivated approximately every 0.3 seconds during generation mode, a high inductance could delay current response and result in a mismatch between force application and PM position. This would reduce force efficiency and potentially lead to oscillations or uneven motion.

The electrical time constant τ of a coil is defined as:

$$\tau = \frac{L}{R} \quad 4.4.5$$

Where R is the coil's electrical resistance. A longer time constant implies a slower electrical response. By fixing the number of turns at 135, a balance was achieved between producing adequate magnetic field strength and ensuring sufficiently fast current response to meet the timing requirements of the motion control system.

This decision was reinforced by simulation results and practical considerations. At 135 turns, the required ampere-turns for each interaction line could still be met by adjusting the current alone, as described in Section 4.4.3. Moreover, this turn count allowed the coil to be physically constructed within a 15 mm height constraint, using commonly available wire gauges such as 24 AWG or 22 AWG, depending on the current requirements at each line.

Additional turn configurations were investigated, including 225, 270, and 360 turns. While these increased the magnetic field strength per ampere, they also raised the coil resistance and inductance significantly, resulting in larger voltage requirements and slower electrical transients. The benefit of reduced current demand was offset by the associated drawbacks in switching speed and control complexity.

By selecting a 135-turn configuration, the system remained compatible with time-based coil switching, allowed for consistent force delivery through current modulation, and supported the practical winding of coils on a hollow iron core. This decision also simplified the simulation setup in Ansys Maxwell, as it standardised the coil geometry across all test cases and ensured that B-field results could be compared directly without needing to normalise for turn count.

In summary, the choice to fix the number of turns at 135 allowed the system to meet magnetic force requirements, minimise switching delays due to inductance, and align with the physical limitations of the prototype's coil form factor.

4.4.8 Coil Design – Appropriate Wire Selection

With the number of coil turns fixed at 135 and the coil height defined as 15 mm, it was necessary to select a wire gauge capable of handling the current required to generate sufficient magnetic force across the three line locations discussed previously. The current required to achieve the target lifting force of 0.55 N at a 3 mm coil–PM separation distance varied significantly based on lateral alignment, as determined in Section 5.4.

For Line 1, located centrally along the coil axis, a current of 1.04 A was required to meet the 140 AT target. Line 2, offset by 4.2 mm, required 1.76 A to achieve 238 AT, while Line 3, located 8 mm off-axis, required 2.77 A to produce 374 AT. The variation in current demand introduced the need for different wire gauges to ensure safe operation, particularly under short-duration current pulses used in generation mode.

Wire gauge selection was guided by standard American Wire Gauge (AWG) current ratings, which specify both continuous and maximum allowable current values. For each scenario, the wire was selected to operate near or below its maximum rating, assuming short activation intervals of under 0.5 seconds per pulse. Table 6 below summarises the wire selection corresponding to each AT requirement:

Line	Offset from Coil Edge (mm)	Required AT	Current (A)	Recommended AWG	Max Current Rating (A)
1	0	140	1.04	24	0.921
2	4.2	238	1.76	22	1.46
3	8	374	2.77	20	2.335

Table 6 AWG Recommendation Per Line

The analysis indicated that while 24 AWG wire is suitable for Line 1, Lines 2 and 3 require progressively thicker wire to manage the higher currents. In particular, Line 3 exceeds the standard maximum rating for 20 AWG, although the brief nature of each pulse suggests this may be acceptable under controlled conditions with thermal monitoring.

In addition to thermal considerations, increased wire diameter reduces resistive losses and improves efficiency. However, larger gauges reduce winding density and increase coil bulk, which must be accounted for in the coil form factor and packing strategy. These trade-offs were carefully evaluated in the design process to ensure that the physical coils could be constructed within the specified height and diameter constraints, without compromising electrical performance.

Furthermore, the fixed coil geometry allowed the AT requirement to be met entirely through current modulation. This simplified the construction process by avoiding the need to fabricate multiple coil variants with different turn counts. A single coil design could be used throughout

the system, with control logic varying the current to match positional demands along the PM's vertical path.

Due to time constraints, extended laboratory testing across the full range of wire gauges and ampere-turn configurations was not feasible. Experimental validation was instead limited to a single test setup comprising a 135-turn coil wound to a height of 15 mm using 28 AWG wire, **with** 0.5 A of current supplied while interacting with a single permanent magnet. Although 28 AWG is not suitable for the higher current levels required in Line 2 and Line 3 configurations, this test confirmed that the coil could operate without insulation breakdown or immediate thermal degradation under short-duration activation.

The experimental setup was configured such that the north pole of the permanent magnet faced the south pole of the electromagnet above, creating an attractive force, while the south pole of the magnet aligned with the south pole of the coil below, resulting in a repulsive force. This combination produced a net upward force acting against gravity, leading to visual acceleration of the PM–mass assembly. Despite the limited scope of testing, the results aligned well with simulation predictions and helped validate the proposed coil design and magnetic interaction strategy.

This outcome demonstrated the fundamental operational principle of the storing mode: that careful control of magnetic polarity and current direction can produce effective lift. Although limited in scope, the test confirmed that the coil–magnet arrangement could generate the correct directional force response when energised appropriately. Together with the detailed ampere-turn analysis and wire selection process, these findings supported the electromagnetic system's capability to operate within defined electrical and thermal boundaries, enabling safe and consistent performance across both storing and generation modes.

4.5 Performance Results

4.5.1 Storage Mode: Power & Energy Input

This section presents a detailed analysis of the power and energy required to lift the permanent magnets and attached weight in storing mode. The results are based on the Line 1 configuration from Section 4.4.3, with electrical and physical characteristics matched to the prototype system. These calculations provide a realistic estimate of energy consumption during one full lift cycle using the EMGES.

Coil Placement and Configuration

A total vertical lift of 570 mm was required, beginning at 15 mm and ending at 585 mm. Coils were physically arranged such that each coil's lower edge was placed 3 mm above the upper edge of the previous coil, creating significant overlap. This method was selected based on simulation and analytical results showing that the maximum magnetic force is exerted at the coil's edge.

Each coil had a physical height of 15 mm, and the 3 mm vertical step between them resulted in 132 coils being used to span the full 570 mm travel distance. At any given moment during storing mode, four coils were simultaneously energised to evenly distribute the required lifting force of 2.2 N (0.55 N per coil).

Coil Electrical Characteristics

Each coil was constructed with 135 turns of 28 AWG copper wire, matching the prototype used in generation mode testing. The resistance of 28 AWG is approximately $0.227 \Omega/m$, and the total wire length per coil was calculated from the winding layout as:

- 1st layer (radius 8.00 mm, 45 turns): 2.262 m
- 2nd layer (8.32 mm, 36 turns): 1.886 m
- 3rd layer (8.64 mm, 30 turns): 1.629 m
- 4th layer (8.96 mm, 24 turns): 1.350 m
- **Total wire length = 7.127 m**
- **Total coil resistance = $7.127 \text{ m} \times 0.227 \Omega/\text{m} = 1.618 \Omega$**

Current and Power Requirement

To maintain net zero acceleration and achieve constant upward velocity, each coil needed to generate a force of approximately 0.55 N. Based on previous ampere-turn analysis, the current required to achieve this force in the Line 1 configuration varied between 0.615 A and 1.04 A, depending on the PM's exact alignment with the coil. An average current of 0.8275 A was assumed to cover the entire 3 mm active zone of each coil.

Using the power equation:

$$P = I^2 R \quad 4.5.1$$

The power required by a single coil was calculated to be 1.11 W based on its electrical resistance and the average current applied. As four coils are energised simultaneously during storing mode, the total system power demand was determined to be 4.43 W. Using the relationship defined in Equation 4.5.2, the corresponding voltage drop across each coil was found to be 1.34 V.

$$V = IR \quad 4.5.2$$

Energy Requirement Over Full Lift

The total time of flight for the lift was previously calculated as 58.34 seconds, based on a constant velocity of 0.01007 m/s. Therefore, the energy required to complete one full lift is 258.55 J as calculated from 4.5.3 below:

$$E = Pt \quad 4.5.3$$

By dividing the total energy consumption by the number of seconds in an hour, the energy required for one full lift cycle was calculated to be **0.0718 Wh**.

Summary

- **Total coils: 132**
- **Average current per coil: 0.8275 A**

- **Power required by system:** 4.43 W
- **Energy required per lift (58.34 s):**
 - 258.55 J
 - 0.0718 Wh
- **Voltage per coil:** ~1.34 V
- **Wire gauge used:** 28 AWG (consistent with the prototype)

This analysis confirms that the EMGES, in storing mode, requires modest power but must maintain continuous delivery over nearly a minute of operation. While 28 AWG wire provides a valid estimate consistent with experimental data, it is not optimal for high-efficiency storage mode operation. Future designs should consider thicker wire (e.g., 24 AWG) to reduce resistive losses and voltage demands, improving thermal and electrical performance.

4.5.2 Storing Mode Efficiency

The overall efficiency of the system in storing mode was assessed by comparing the useful mechanical energy gained during the lift to the total electrical energy consumed. The useful output energy is represented by the gravitational potential energy of the mass–magnet system, calculated as:

$$E = mgh = Fh \quad 4.5.4$$

Where the force is the PMs and weight under gravity are 2.2 N and the height of the system is 0.57m, the gravitational potential energy of the system is 1.254 J. The electrical input energy was determined using the time-of-flight approach, which most accurately reflects the system's operation.

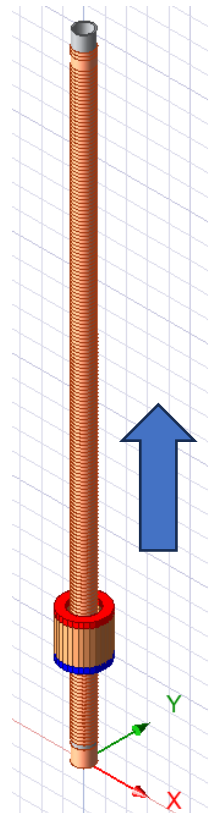


Figure 4.5.1 : EMGES in Storage Mode

In this method, four coils remained continuously energised throughout the lift duration of 58.34 seconds, drawing a combined average power of 4.43 W, resulting in a total energy consumption of 258.55 J. The resulting energy efficiency is given by the maximum potential energy over the energy required to get it there multiplied by 100%. In this case, the efficiency of the system in storage mode is 0.49%.

This low efficiency is expected at the prototyping stage and is largely attributed to resistive losses in the 28 AWG copper wire, magnetic leakage, and continuous energisation of overlapping coils. These heat losses account for between 95 to 97% of the system. Future improvements such as the use of lower-resistance wire, refined coil timing strategies, and enhanced magnetic coupling will be necessary to improve the overall energy efficiency of the system in storing mode.

To evaluate the influence of wire gauge on system efficiency, a comparison was conducted between the prototype configuration using 28 AWG copper wire and an improved design using 24 AWG wire. Both cases were based on an identical coil geometry, consisting of 135 turns wound over a 15 mm height, with a total wire length of 7.127 metres per coil. It was assumed that four coils were simultaneously active, each carrying an average current of 0.8275 A over a lift duration of 58.34 seconds. The only parameter that varied was the electrical resistance of the wire, taken as 0.227 Ω/m for 28 AWG and 0.085 Ω/m for 24 AWG.

Under these conditions, the power consumption per coil decreased from 1.108 W to 0.415 W, leading to a reduction in total system energy consumption from 258.55 J to 96.80 J. The system efficiency, defined as the ratio of useful mechanical energy (gravitational potential energy) to total electrical input, increased from 0.49% using 28 AWG to 1.30% with 24 AWG. This highlights the significant role that wire selection plays in energy efficiency, particularly in systems where resistive losses dominate. While 28 AWG was suitable for low-current prototype testing, 24 AWG offers a substantial improvement in electrical performance and thermal resilience, making it more appropriate for an operational EMGES system.

4.5.3 Line 2 & 3 Comparison

Following the in-depth analysis of Line 1, additional energy and efficiency evaluations were conducted for Lines 2 and 3, which represent off-axis interaction regions located 4.2 mm and 8.0 mm, respectively, from the electromagnet's central axis. These lines required progressively stronger magnetic fields to achieve the same lifting force, and thus demanded higher current levels. To maintain consistent comparison, all scenarios assumed four coils active simultaneously, each operating over a lift duration of 58.34 seconds.

Each case was evaluated using the prototype wire gauge (28 AWG) and then again using a more suitable gauge selected based on current handling needs and coil heating concerns: 24 AWG for Line 1, 22 AWG for Line 2, and 20 AWG for Line 3.

Parameter	Line 1 (28 AWG)	Line 1 (24 AWG)	Line 2 (28 AWG)	Line 2 (22 AWG)	Line 3 (28 AWG)	Line 3 (20 AWG)
Average current (A)	0.8275	0.8275	1.4	1.4	1.905	1.905
Resistance per coil (Ω)	1.618	0.606	1.618	0.377	1.618	0.239
Voltage per coil (V)	1.34	0.5	2.27	0.53	3.08	0.45
Power per coil (W)	1.11	0.415	3.171	0.747	5.872	0.866
Total power (4 coils) (W)	4.43	1.659	12.685	2.989	23.487	3.466
Total energy consumed (J)	258.55	96.8	740.05	174.4	1370.23	202.19
Useful energy (J)	1.254	1.254	1.254	1.254	1.254	1.254
Efficiency (%)	0.49	1.3	0.169	0.719	0.092	0.62

Table 7 Line & AWG Comparison

This full comparison reveals several important trends. First, as the point of electromagnetic interaction moves further from the coil's central axis (from Line 1 to Line 3), the current required to maintain a net lifting force increases substantially. As a result, the total power and energy consumption also increase, particularly when using thinner wire (28 AWG). However, replacing the prototype wire with a more suitable gauge greatly reduces resistive losses, voltage drop, and thermal buildup.

Line 1, when paired with 24 AWG wire, showed the highest system efficiency of 1.30%, consuming just 96.8 joules of energy over the lift period. This makes it the most energy-efficient configuration tested. Line 2 followed closely, with 22 AWG reducing the energy requirement to 174.4 joules and boosting efficiency to 0.719%. Even Line 3, which initially had the worst performance using 28 AWG, showed strong improvement with 20 AWG, reducing energy demand from 1370.23 to 202.19 joules and lifting efficiency from 0.092% to 0.62%.

These results demonstrate that the physical location of the PM-coil interaction and the chosen wire gauge are key factors influencing power consumption and overall system performance. While Line 1 remains the most efficient configuration, Lines 2 and 3 can also be made viable with appropriate material choices.

4.5.4 Generation Mode: Power & Energy Output

4.5.4.1 Influence of Number of Turns on Instantaneous Power Output

To evaluate the performance of the EMGES system in generation mode, experimental and theoretical tests were conducted on two coil configurations: a 45-turn coil and a 135-turn coil, both wound with 28 AWG copper wire and wrapped around an 8 mm radius iron core with a consistent coil height of 15 mm. The open-circuit voltage was recorded during the free fall of two identical permanent magnets through the coil structure. These tests aimed to assess the magnitude and structure of the induced EMF and the resulting instantaneous power output.

The approach adopted for power analysis followed the methodology outlined by Dr Carroll, whereby the generator is modelled as a time-varying open-circuit voltage source $V(t)$, with internal coil resistance R_c and a matched resistive load R_L such that $R_L=R_c$. The instantaneous power delivered to the load is given by [68]:

$$P(t) = \frac{V(t)^2 R_L}{(R_c + R_L)^2}$$

4.5.5

For the 45-turn coil, the calculated resistance was 0.51346Ω . Using this value, the theoretical and experimental EMF waveforms (Figure 4.2.2, Figure 4.2.5 Figure 4.2.4) were processed to produce instantaneous power curves over a 230 ms interval. The resulting power waveform was plotted over a time window of 230 ms. Both the theoretical and experimental EMF waveforms were processed using this model. The predicted waveform yielded peak power outputs of over 4.4 W and maintained power above 3.7 W, while the experimental waveform peaked at approximately 4.3 W but severely dropped to maintaining over 1.5 W. These spikes occur as the north and south poles of the falling magnets induce voltage pulses while passing through the magnetic region of the coil.

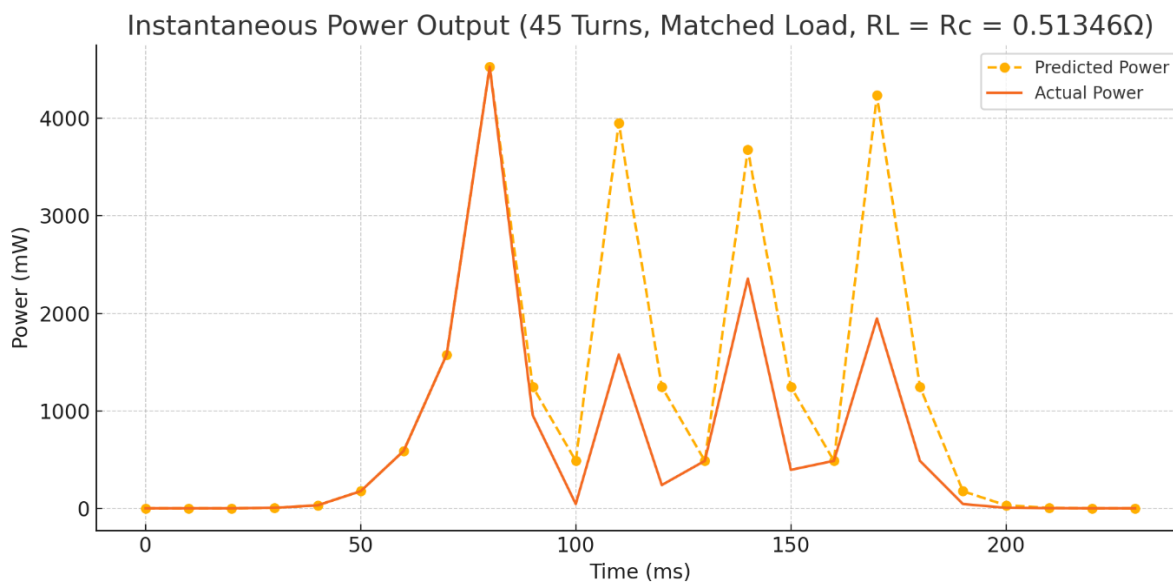


Figure 4.5.2 Predicted Power vs Actual Power 45 Turns [72]

The waveform profile was consistent with expectations, featuring four main pulses—two for each magnet—as predicted by Faraday’s Law of Induction. The difference between predicted and measured values can be attributed to system losses such as mechanical friction, alignment deviation, and eddy current effects. Nonetheless, the results confirmed that meaningful electrical power can be generated from a single compact coil using passive magnet motion.

To investigate the scalability of the generation system, a second test was conducted using a 135-turn coil with the same physical dimensions. The resistance for this configuration was calculated as 1.618Ω , and the same matched load methodology was applied. With the number of turns tripled, Faraday’s Law predicted a proportional increase in EMF magnitude (Equation 3.3.2). The open-circuit voltage data collected for this test confirmed this, with significantly higher peak voltages.

The predicted power waveform for the 135-turn coil reached a peak of approximately 18.7 W, while the experimental power waveform peaked at 18.5 W, demonstrating excellent agreement. Both waveforms exhibited the same four-pulse structure observed in the 45-turn

analysis, with similarly timed voltage peaks resulting from the sequential entry and exit of the permanent magnets' poles. While the amplitude was significantly higher, the energy was still delivered over a short interval (less than 250 ms), as expected.

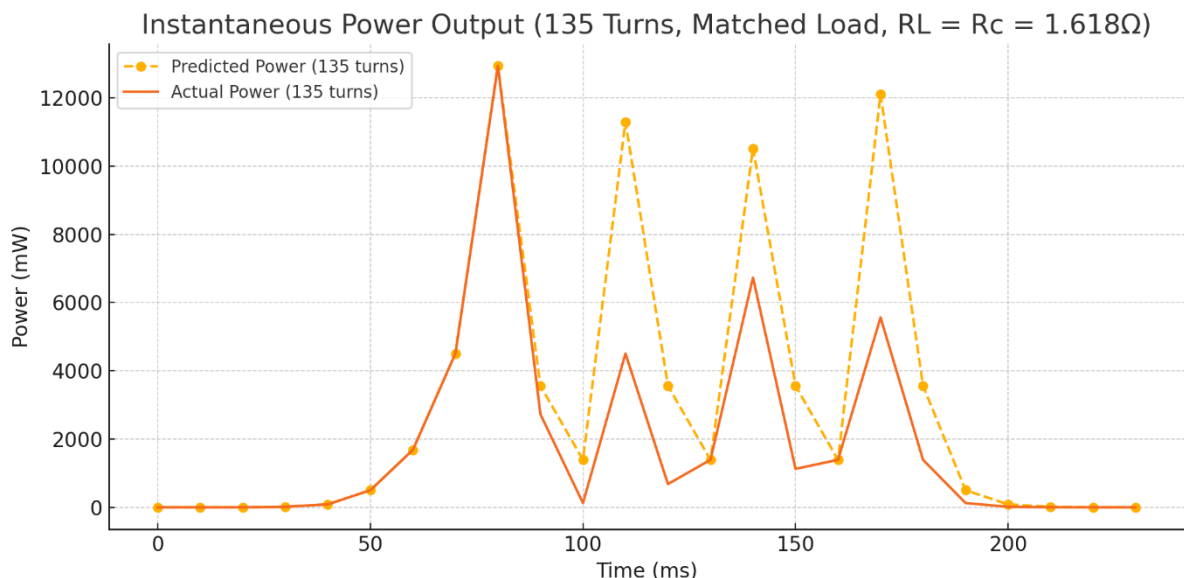


Figure 4.5.3 : Predicted Power vs Actual Power 45 Turns

Although a photograph of the oscilloscope output during the 135-turn test was not captured—due to the test being conducted independently in the laboratory—the observed waveform matched the 45-turn test profile shown in Figure 4.2.5. The same distinct four-peak structure was evident on the oscilloscope, further validating the consistency of the EMF response across different coil turn counts. The primary distinction between the two tests lay in the waveform amplitude, which scaled proportionally with the number of turns, in agreement with theoretical expectations.

These findings confirm that increasing the number of turns in the coil boosts the induced EMF and, correspondingly, the instantaneous power output. However, the increase in resistance that accompanies more turns must be carefully considered, as it can introduce additional losses if not properly matched or controlled. Together, these results provide a high-fidelity comparison between two generation-mode configurations and form a valuable foundation for assessing overall system efficiency to storage mode energy input.

4.5.4.2 Influence of AWG on Power Output

To examine the effect of wire gauge on electrical performance during generation mode, the predicted EMF waveform from the 45-turn coil test was used to compare two wire gauges: the originally used 28 AWG and a lower-resistance alternative, 24 AWG. While the magnetic and geometric properties of the coil remained constant—meaning the EMF waveform did not change—the internal resistance of the wire varied significantly. The 28 AWG wire used in testing had a resistance of approximately 0.513Ω for the 45 turns, while the 24 AWG wire, over the same coil length, exhibited a resistance of approximately 0.213Ω .

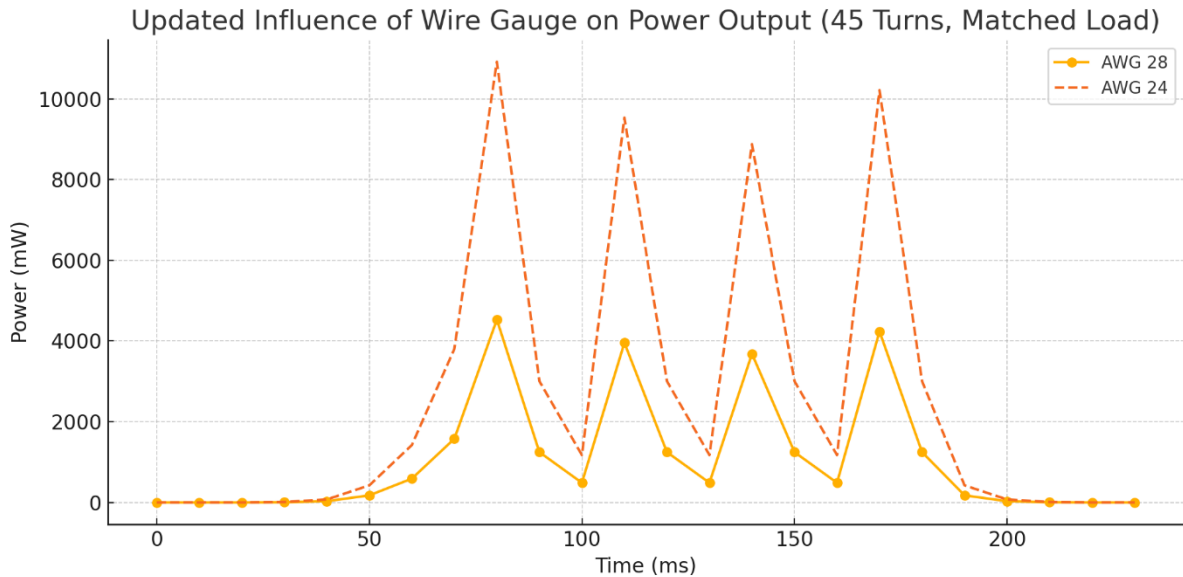


Figure 4.5.4 : AWG 28 vs 24 Power Output Prediction

Using Carroll's method for power estimation under matched load conditions, the instantaneous power output was calculated for each wire type. The results, shown in Figure 4.5.4, demonstrate that the predicted 24 AWG coil produced significantly higher power throughout the waveform. Peak power increased from approximately 4.3 W with 28 AWG to 10.7 W with 24 AWG, with consistently higher power output across all time steps.

This improvement is attributed to the reduced resistive losses in the thicker wire, which allows more of the generated voltage to be transferred to the load. The matched load condition ensures maximum power transfer, and the reduced coil resistance in the 24 AWG setup results in greater efficiency without altering the induced EMF.

These findings highlight the importance of selecting an appropriate wire gauge in energy harvesting applications. While thinner wires may be easier to wind and occupy less space, they introduce greater electrical resistance, which can significantly limit power delivery to the load. In contrast, thicker wires such as 24 AWG offer superior power transfer characteristics, particularly when the goal is to maximise energy recovery during each generation cycle.

4.5.4.3 Average AC Power Calculation and Conversion Potential

To estimate the useful energy generated by a single coil during generation mode, a time-domain analysis of the open-circuit EMF waveform was performed. The RMS voltage provides a measure of the effective DC-equivalent value of this time-varying voltage. The EMF data were squared and integrated over the pulse duration (230 ms), as shown in the fourth column of Table 8.

Time (ms)	Theoretical EMF(V)	Actual EMF(V)	Theoretical $V(t)^2$	Actual $V(t)^2$
0	0	0	0	0
10	0	0	0	0
20	0	0	0	0

30	0.1	0.1	0.01	0.01
40	0.25	0.25	0.0625	0.0625
50	0.6	0.6	0.36	0.36
60	1.1	1.1	1.21	1.21
70	1.8	1.8	3.24	3.24
80	3.05	3	9.3025	9.3025
90	1.6	1.4	2.56	1.96
100	-1	-0.3	1	0.09
110	-2.85	-1.8	8.1225	3.24
120	-1.6	-0.7	2.56	0.49
130	1	1	1	1
140	2.75	2.2	7.5625	4.84
150	1.6	0.9	2.56	0.81
160	-1	-1	1	1
170	-2.95	-2	8.7025	4
180	-1.6	-1	2.56	1
190	-0.6	-0.3	0.36	0.09
200	-0.25	-0.1	0.0625	0.01
210	-0.1	-0.05	0.01	0.0025
220	0	0	0	0
230	0	0	0	0

Table 8.45 Turn, 28 AWG Theoretical & Actual Waveform

From the integral of $V(t)^2$, the RMS voltage was calculated using:

$$V_{rms} = \sqrt{\frac{1}{T} \int_0^T V(t)^2 dt} \quad 4.5.6$$

Applying this numerically to the sum of the EMF waveform over time yielded an RMS voltage of approximately 0.465 V.

For resistive load matching (where load resistance R_L equals coil resistance $R_c=0.513 \Omega$), the average power delivered was calculated using:

$$P_{avg,AC} = \frac{V_{rms}^2}{4R_c} \quad 4.5.7$$

This yielded a power output of approximately 105 mW per coil.

The time during which the PM interacts with a single coil is approximately 75 ms, based on a 15 mm coil height and a drop velocity of 0.2 m/s.

This results in an energy contribution per coil of 7.88mJ. For the complete 132-coil system, the total energy delivered in one drop is 1.04J

This gives the system a theoretical efficiency of 81%. However, 8 coils will not be energised by the second magnet, therefore a more realistic efficiency is 79%

Assuming a total descent time of 2.925 seconds, this corresponds to a continuous average power output of 356 mW.

The same calculation was processed for the fifth column of data in Table 8. The results can be compared in the table below:

Parameter	Value Theoretical	Value Actual	Unit
RMS Voltage	0.465	0.397	V
Avg. AC Power per Coil	105	76.8	mW
Energy per Coil per Pass	7.88	5.76	mJ
Total AC Energy (132 coils)	1040	760	mJ
Continuous AC Power	356	260	mW
DC Power (Diodes)	84	Infeasible	mW
DC Power (Synchronous Rectifier)	354	258	mW

Table 9 Comparison of Theoretical v Actual Power Output

These results form a baseline for assessing the viability of DC power extraction. Because the output waveform is pulsed and asymmetric, conversion to DC is necessary for practical use. The subsequent section will discuss the implications of rectification techniques—specifically, the advantages of synchronous rectification over traditional diode-based approaches—on energy harvesting efficiency from the EMGES prototype.

AC-to-DC Conversion for Optimal Power Extraction

In order to effectively utilise the AC power generated by the EMGES system, conversion to stable DC power is essential. This section compares two rectification strategies—passive diode-based rectifiers and active synchronous rectifiers—with a focus on their efficiency, power loss characteristics, and implementation viability for low-voltage, pulse-based energy harvesting scenarios. Emphasis is placed on system compatibility, component selection, and quantitative performance analysis to support optimal design decisions for EMGES energy recovery.

Conventional full-wave rectifiers based on Schottky diodes introduce forward voltage drops of approximately 0.3 V per diode, which is particularly detrimental in low-voltage systems. In this case, where the average current through the rectifier (V_{rms} over the R_L+R_c) was approximately 0.453 A, the associated power loss was calculated as 0.272 W from Equation 4.5.8 below:

$$P_{loss} = 2 I_{avg} V_f \quad 4.5.8$$

Given an AC power input of approximately 356 mW (derived from the total system generation energy at a drop speed of 0.2 m/s), this results in a DC output power of 84mW

This yields a theoretical efficiency of only 23.6%, excluding further downstream losses due to voltage regulation or storage.

Synchronous rectification replaces lossy diodes with actively controlled MOSFETs, which conduct with significantly lower resistance. Using IRF3205 transistors (with $R_{DS} = 0.008\Omega$), the theoretical conduction loss becomes 1.6mW from the Equation 4.5.9 below:

$$P_{loss} = I^2 R_{DS(on)}$$

4.5.9

Thus, nearly the entire generated AC power is preserved (354.4mW). This equates to an ideal efficiency exceeding 99.5%. In practice, controller and gate driver overhead reduce this to an estimated range of 85–93%, which still marks a substantial improvement over diode-based rectification.

Component Selection and Design Implementation

The proposed synchronous rectification setup includes:

- **MOSFETs:** Two IRF3205 transistors ($V_{GS} = 4V$, $R_{DS(on)} = 8m\Omega$), capable of handling the required current while minimising conduction losses [73].
- **Controller:** LTC4357, selected for its low-voltage compatibility and integrated gate driver functionality [74].
- **Gate Driver:** IRS2004, enabling precise control of high-side and low-side MOSFETs where required [75].
- **Output Filtering:** A 220 μF capacitor ensures ripple suppression to within 10% of the peak voltage.
- **Voltage Regulation:** An LTC3105 boost converter is used to step up the rectified DC voltage to a regulated 3.3 V or 5 V, suitable for downstream electronics [76].

Parameter	Diode Rectifier	Synchronous Rectifier
Loss Mechanism	Forward voltage (V_f)	Conduction resistance ($R_{DS(on)}$)
Theoretical Loss	272 mW	1.6 mW
DC Output Power	84 mW	354 mW
Efficiency	23.60%	~93%
Circuit Complexity	Low	Moderate

Table 10 Comparative Performance Summary

The comparative analysis clearly demonstrates the superiority of synchronous rectification for low-voltage energy harvesting applications such as the EMGES system. In traditional diode-based rectifiers, the forward voltage drop—typically around 0.3 V—results in a substantial loss of energy, particularly detrimental when the peak generated voltages are in the range of 3 V or less. This inefficiency becomes even more pronounced in high-current, pulsed systems where energy must be captured rapidly and with minimal loss.

Synchronous rectifiers, by contrast, replace passive diodes with actively controlled MOSFETs, dramatically reducing conduction losses. This not only improves power conversion efficiency but also reduces thermal dissipation within the rectifier circuitry. For the EMGES

configuration, theoretical analysis indicated that synchronous rectification could increase usable DC output by nearly a factor of four compared to diode-based designs, elevating efficiency from approximately 24% to over 90%.

However, these performance gains are accompanied by added design complexity. Synchronous rectification requires precise gate timing, careful PCB layout to minimise parasitic effects, and suitable power allocation for gate drivers and control circuitry. These factors must be carefully considered in any practical implementation.

To better evaluate and refine the performance of the proposed rectifier topologies, a series of time-domain simulations were carried out using LTspice. These simulations modelled the pulsed nature of the coil-induced voltages and allowed for detailed exploration of MOSFET switching behaviour, rectifier performance, and ripple control strategies.

The next section presents the design and results of these LTspice simulations, highlighting key insights into the transient behaviour of the synchronous rectifier system under EMGES operating conditions.

4.5.5 Rectification of Experimental EMF

To evaluate the viability of passive rectification for the EMGES system, a full-wave bridge rectifier was simulated using LTSpice, incorporating the actual EMF waveform recorded during the laboratory open-circuit voltage (OCV) test. The measured waveform was implemented using a piecewise linear (PWL) voltage source in LTSpice, thereby accurately replicating the non-sinusoidal, pulsed nature of the EMF signal generated by the 45-turn coil configuration in generation mode.

Figure 4.5.5 shows the schematic of the simulation. A full-wave bridge was formed using four ideal diodes (D5–D8), with a resistive load placed in parallel with a smoothing capacitor at the output node. The series inductance and resistance elements (L1 and R1) represent the coil's measured properties during the EMF test, and the input source (V1) reflects the lab-captured waveform.

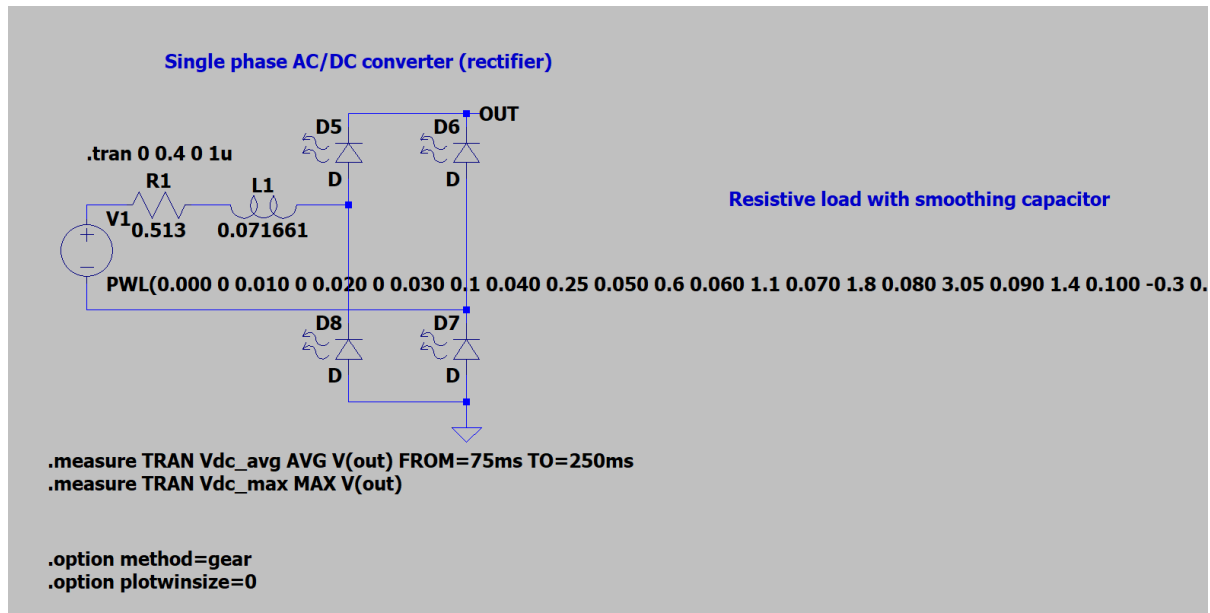


Figure 4.5.5 : LTSpice Rectifier Circuit Using Measured EMF as PWL Input

The corresponding output waveform is shown in Figure 4.5.6. The output demonstrates sharp voltage peaks that closely follow the input EMF envelope, but with the negative portions of the waveform flipped to positive — as expected from full-wave rectification. Due to the absence of a smoothing capacitor, the voltage immediately drops between pulses, resulting in a **pulsed DC output** rather than a stable DC level.

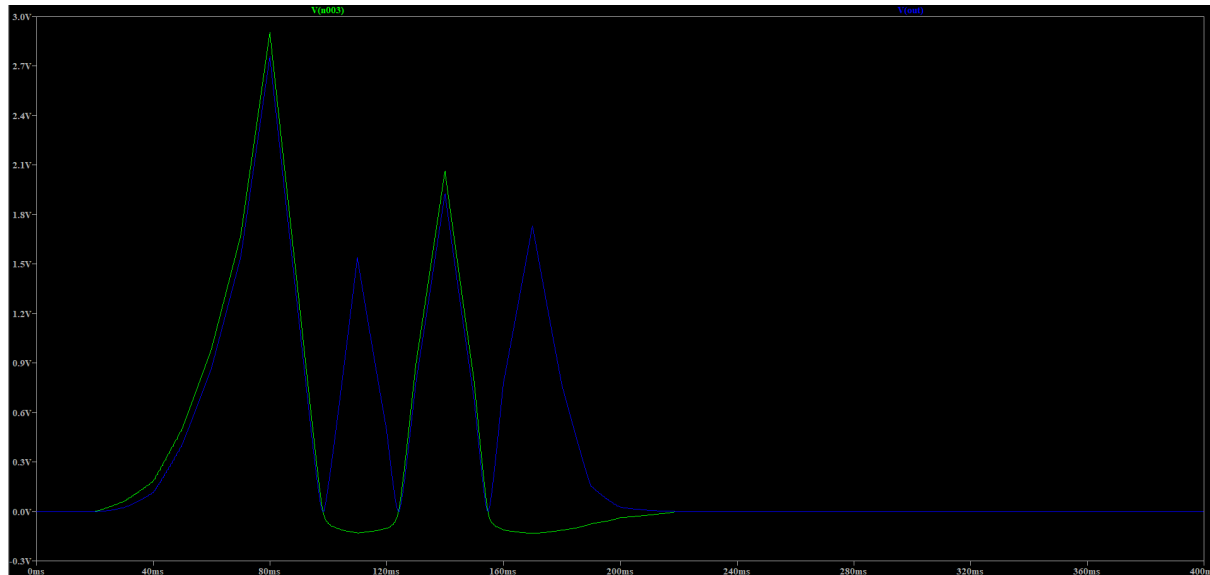


Figure 4.5.6 : Output Voltage from LTSpice Simulation of Experimental EMF Through Bridge Rectifier

These spikes represent the instantaneous power transfer moments where the coil voltage exceeded the forward voltage threshold of the diodes, allowing current to flow. This highlights a key insight: without smoothing, the system produces bursts, and momentary power outputs, which may not be suitable for direct storage or use by sensitive electronics.

This unfiltered output highlights the need for downstream power conditioning — such as smoothing capacitors or active rectification — to make the harvested power more usable. In

practice, any energy storage element would need to account for this pulsed profile, which could also affect charge efficiency and converter performance if not properly managed.

4.6 Scaled -Up Model

To assess the practicality of deploying the EMGES at industrial scale, this section evaluates two methods for scaling the system from the prototype to a mine shaft installation of 400 m height. Each method was assessed in terms of current, voltage, power, and energy requirements during the storage mode (lifting phase), and compared for feasibility and efficiency.

A direct scale-up from the prototype configuration was performed by proportionally enlarging key geometric and mass-related parameters. Table 4.9.1 summarises the scaled values and associated scaling factors.

Parameter	Prototype	Mineshaft Scale	Scaling Factor
Magnet radius	5 mm	0.75 m	150×
Magnet mass	0.224 kg	1,834.86 kg	8,191×
Lift height	0.57 m	400 m	702×
Coil spacing	3 mm	90 mm	30×
Coil height	15 mm	450 mm	30×
Magnet thickness	5 mm	150 mm	30×

Table 11 2kWh Scaled-up Parameters

4.6.1 Method 1 – Direct Scale-Up Using Prototype Turn Count

In this approach, the number of turns per coil was kept the same as in the prototype (135 turns). The scaled system must lift a mass of 1,834.86 kg, giving a gravitational force of 18,000N. Assuming four coils are activated simultaneously, the force per coil is 4500 N.

From the prototype, an average of 112 AT generated 0.55 N, thus 916,364 AT would be required for this scaled up model. To achieve this with 135 turns, it was calculated that 6,788 A of DC would be required.

Given a mean coil radius of 0.85 m, a wire length per turn of 5.34m was calculated. This led to a total wire length of 720.9 m. Using AWG 4/0 wire, which has a resistance of 0.049 Ω /km, the resistance was found to be 0.035 Ω . Hence the voltage per coil was calculated as 237.6 V and power per coil as 1.61 MW. As 4 coils would be active at any instance, the power required from the 4 coils would be 6.44 MW.

Assuming a constant scaled-up velocity of 30 times the prototype, $v = 0.3021$ m/s. The time of flight is then calculated to be 1,324 seconds, approximately 22 minutes. From here the energy consumed is found to be 8,528 MJ which is approximately 2.37 MWh. This is 1,185 times greater than the potential energy of the 2 kWh system, giving an efficiency of 0.084%.

This method results in extremely high currents, impractical even with large copper conductors. Hence a second method was deployed.

4.6.2 Method 2 – High-Turns, Lower Current Approach

Increasing the number of turns per coil reduces the current requirement for the same AT. Using 3,000 turns gives a required current of 305 A, which is within AWG 4/0 normal operating current range. This increase in turns gave a new total wire length of 16,020 m and a new coil resistance of 0.78Ω . The voltage remained the same as the current and resistance scale accordingly however the power per coil reduced significantly to 72.6 kW per coil. This gave a P_{total} of 290.4 kW and led to a total energy consumption of 107 kWh as the time of flight also remained the same. This decrease led to a massive improvement in system efficiency of 1.87%.

The below table summarizes the findings of the two methods of scaling

Metric	Method 1 (135 Turns)	Method 2 (3,000 Turns)
Current/coil	6,788 A	305 A
Voltage/coil	237.6 V	238 V
Power (4 coils)	6.44 MW	290.4 kW
Energy input	2.37 MWh	107.5 kWh
Efficiency	0.08%	1.87%
Coil resistance	0.035Ω	0.78Ω
Implementation	Requires superconductors	Standard copper wires viable

Table 12 Comparison of Scaled Storage Methodology

The high-current, low-turns method (Method 1) imposes unsustainable demands on conductors, switching circuits, and thermal management. Even heavy copper cabling cannot safely conduct $\sim 6,800$ A without superconducting materials or extreme cooling.

By contrast, Method 2 significantly reduces current to a manageable level while only modestly increasing resistance and voltage. Though still inefficient, this approach offers a practical route to scaling. Most critically, it brings the EMGES closer to realistic power electronics, coil manufacturing, and structural tolerances.

Key Limitations:

- Substantial resistive losses persist in both cases.
- Efficiency remains low due to non-mechanical magnetic losses.
- Energy input is an order of magnitude higher than energy stored.

As the EMGES system is scaled to industrial dimensions, such as a 400 m-deep vertical mineshaft, the use of multiple PM assemblies within the same shaft becomes a practical and attractive strategy. Deploying several magnet-weight units in tandem offers not only greater flexibility and higher energy throughput, but also improves operational redundancy and load distribution across coil segments.

However, introducing multiple PMs along a shared shaft presents new challenges—most notably, the risk of magnetic interaction between vertically adjacent PM units. Such interactions can result in undesired attraction or repulsion, potentially destabilising the controlled lift or descent of the magnets. To avoid this, the axial magnetic force between two identical cylindrical magnets (3.3.12) is evaluated using the following criteria: $B_r = 1.3 \text{ T}$, $R = 0.85 \text{ m}$, $t = 0.3 \text{ m}$ and a force threshold of 0.5% of the weight of the system (90 N) to ensure negligible interaction.

Solving the equation under this constraint revealed that a minimum vertical spacing of 2.5 m between PM assemblies is required to maintain safe operation. This spacing defines the minimum “non-active” height between each magnet, thereby limiting the system’s depth of discharge (DoD).

While this sacrifices a portion of the shaft’s energy storage potential, the trade-off ensures mechanical stability and magnetic decoupling, which are essential for reliable and autonomous operation.

Despite the DoD impact, the use of multiple PMs introduces several **critical operational benefits**:

- **Increased Instantaneous Power Output:** Releasing two or more PM assemblies concurrently doubles or triples the energy output during a generation cycle. This capability is invaluable for short-term grid balancing and high-power dispatch events.
- **Dynamic Energy Management:** The EMGES system becomes a tuneable resource capable of adapting its power output based on real-time energy demand. For instance, during grid oversupply, one or more PMs can be lifted to absorb excess power.
- **Regenerative Braking:** By modifying the coil switching pattern during descent, it is possible to slow the fall rate of the magnets, effectively increasing energy extraction time and boosting total kWh output. This flexibility aligns with grid response strategies that prioritise sustained power delivery over instantaneous output.
- **Modular Design:** Distributed PMs reduce the force required per coil, lowering per-unit stresses and simplifying mechanical design. Additionally, if one unit fails or is removed for maintenance, others can continue to operate, enhancing system resilience.

In summary, multi-magnet operation is a transformative element of the scaled EMGES system. It offers operational scalability, dispatchability, and energy management flexibility, but must be carefully balanced against design trade-offs like shaft spacing and depth-of-discharge. The design choice to space PMs at 2.5 m ensures stability without severely compromising energy capacity.

4.6.3 Conclusion and Recommendations

The scaling analysis of the EMGES system has highlighted several critical engineering challenges, particularly in relation to current delivery and energy efficiency. Method 1, which

directly scaled the prototype's coil geometry while maintaining the original 135-turn configuration, resulted in impractical current demands of over 6,700 A per coil—well beyond the capabilities of conventional copper conductors. In contrast, Method 2 introduced a higher turn count of 3,000 turns per coil, significantly reducing the required current to approximately 305 A. This modification not only brought the system into a more manageable operational range but also improved energy efficiency from 0.084% to 1.86%, representing a 22-fold increase.

To further enhance the feasibility and performance of the EMGES concept, future work should focus on the following areas:

- Improving electromagnetic coupling under both static and dynamic conditions to increase force output and reduce energy loss.
- Investigating the use of active magnetic switching strategies to minimise idle power consumption and better control the timing of electromagnetic forces.
- Exploring the integration of superconducting coils, which could eliminate resistive losses and enable higher efficiency at scale.
- Conducting detailed simulation and experimental validation of multi-magnet configurations, including their behaviour under regenerative braking and variable descent profiles.

Collectively, these developments will be essential for advancing the EMGES system from a laboratory-scale prototype toward a robust, scalable energy storage solution capable of meeting the demands of modern electrical grids.

4.7 Scaled-Up EMGES LCOS

The LCOS is a key economic metric used to assess the viability of energy storage technologies by expressing the lifetime cost per unit of energy output, typically in \$/kWh. This section presents a detailed LCOS analysis for the proposed EMGES system under two scenarios: a 20-year deployment and a 40-year extended-lifetime scenario. Both cases are based on the high-turn, low-current configuration (3,000 turns per coil, 305 A) with a total energy storage capacity of 2 kWh (7.2 MJ).

4.7.1 Methodology and Assumptions

The LCOS was calculated using the following expression:

$$LCOS = \frac{CAPEX_0 + \sum_{t=1}^n \frac{OPEX_t}{(1+r)^t} + \frac{CAPEX_{rep}}{(1+r)^{t_{rep}}}}{\sum_{t=1}^n \frac{E_{out,t}}{(1+r)^t}} \quad 4.7.1$$

Where:

$CAPEX_0$ = Initial capital expenditure

$CAPEX_{rep}$ = Mid-life capital replacement costs

$OPEX_t$ = Annual operational expenditure

$E_{out,t}$ = Annual Energy output (kWh)

r = Discount rate

n = System lifetime

t_{rep} = Year of component replacement

Parameter	Original Scenario	Revised Scenario
System Lifetime	20 years	40 years
Cycles per Year	200	260
Round-Trip Efficiency	1.51% (includes Generation efficiency)	1.51%
Annual Output	400 kWh	520 kWh
Discount Rate	5%	5%

Table 13 Operating Comparison Assumptions

4.7.1.1 Cost Breakdown and Input Parameters

Capital Expenditures (CAPEX)

Component	Estimate	Notes
NdFeB Magnets (1,835 kg)	\$55,050	\$30/kg, 40-year lifespan
Coils (132 units)	\$1,584,000	\$12,000 per coil; replaced at year 20
Power Electronics	\$500,000	Includes inverters, controllers
Mineshaft Modifications	\$2,000,000	Shaft retrofitting and structural works
Cooling System	\$200,000	Active cooling for high-current coils
Total Initial CAPEX	\$4,339,050	

Table 14 Scales EMGES CAPEX

Operational Expenditures (OPEX)

Component	Annual Estimate
Electricity (lifting energy)	\$14,000
Maintenance (parts + repair)	\$50,000
Labour	\$100,000
Total OPEX	\$164,000/year

Table 15 Scaled EMGES OPEX

Mid-life replacements at year 20 include:

- Coil set: \$1,584,000
- Power electronics: \$500,000

- Cooling: \$200,000

Total CAPEX at Year 20: \$2,284,000

4.7.1.2 LCOS Results and Comparison

Using discounted cash flow analysis over each scenario's lifetime

Scenario	LCOS (\$/kWh)	Efficiency	Total Output (kWh)	Total Cost (PV)
20-Year, 200 cycles	\$1,258	1.51%	4,988 kWh	\$6.28 million
40-Year, 260 cycles	\$924	1.51%	8,700 kWh	\$8.04 million

Table 16 Scaled Scenario Comparison

The extended operation and increased cycle count reduced LCOS by 27%, from \$1,258/kWh to \$924/kWh. This improvement reflects the amortisation of fixed capital costs over a longer operating horizon and increased throughput.

The below table compares EMGES to other SOTA technologies. EMGES currently underperforms compared to conventional options. The largest contributor to high LCOS is poor round-trip efficiency—driven by ohmic losses in long copper coils and energy loss during lifting.

Storage Technology	LCOS (\$/kWh)	Round-Trip Efficiency	Lifespan
EMGES (proposed)	924–1,258	1.5–1.9%	20–40 yrs
Lithium-Ion	200–400	85–90%	10–15 yrs
Pumped Hydro	100–150	70–85%	40–60 yrs
Flywheel	300–500	85–90%	20 yrs

Table 17 SOTA Technology Comparison

The current EMGES configuration demonstrates the feasibility of mechanical-to-electrical energy storage using magnetic and coil interactions, but its LCOS remains high, ranging from \$924 to \$1,258 per kWh. Substantial improvements are required in system efficiency and cost structure to make EMGES competitive with conventional grid storage technologies.

Future research and prototyping should focus on:

- Incorporating superconductors to increase round-trip efficiency.
- Investigating modular, scalable coil systems for easier replacement and manufacturing.
- Exploring material costs through alternative wire types.

- Increasing the cycle rate to improve utilisation of capital investment.

With these refinements, EMGES could become a niche solution for long-duration, site-specific applications where traditional methods are impractical.

4.7.2 Utilisation of Waste Heat from EMGES Operation

The operation of the EMGES results in significant energy dissipation as heat, with simulations indicating that approximately 98.5% of the input energy (e.g., 387 MJ for a 107.5 kWh input in the scaled 400 m model) is lost, primarily through resistive heating in the coils and power electronics. This section examines potential strategies to harness this waste heat, transforming an inefficiency into a valuable resource to enhance the system's overall utility. Three feasible approaches are considered, prioritising practicality within the context of repurposed mineshafts and renewable energy integration.

Firstly, district heating offers a practical means to utilise this heat for space heating or industrial applications. Heat exchangers installed at the coils, where temperatures may reach 60–80°C or higher during peak operation, could transfer this energy to a water circuit, distributing hot water through insulated pipes to nearby residential, commercial, or agricultural facilities, such as greenhouses. Given the near 6.44 MW thermal output, this could meet substantial heating demands—potentially supplying hundreds of households or an industrial complex—offsetting local energy costs by an estimated 30–50%, with infrastructure costs ranging from €100,000 to €1,000,000 depending on scale and proximity.

Thirdly, an Organic Rankine Cycle (ORC) system could exploit the high thermal output to drive a micro-turbine, using a low-boiling-point fluid like pentane to generate electricity at an efficiency of 10–15%. At close to 6.44 MW of heat, this could produce 644–966 kW of additional power, a significant improvement over the EMGES's native 1.87% storage efficiency, aligning more closely with industrial-scale energy recovery needs. However, the substantial capital investment—exceeding €1,000,000 for a suitably sized ORC unit—alongside integration complexity, positions this as a longer-term solution, better suited to future large-scale deployments.

These approaches—district heating and ORC—demonstrate viable pathways to mitigate the thermal losses of EMGES, with district heating offering the most immediate and cost-effective application given the scale of heat available.

4.8 Exploration of Unimplemented Design Concepts

4.8.1 Halbach Array

During the conceptual development of the EMGES, one of the more ambitious magnetic configurations considered was the implementation of a Halbach array. A Halbach array is a specialized arrangement of permanent magnets designed to amplify the magnetic field on one side of the array while significantly reducing it on the other. This directional enhancement is achieved by orienting the magnets in such a way that their individual magnetic field vectors

combine constructively on one face and destructively on the opposite. In a simplified linear array, for instance, the magnetic field lines emerge strongly from one side and curve back weakly or nearly cancel out on the other, resulting in a highly asymmetric magnetic field profile.

While this seemed advantageous at first—especially for reducing stray fields and maximizing magnetic flux density through the coils—the concept was ultimately deemed unsuitable for the EMGES system. The primary limitation arises from the requirement for symmetrical magnetic field strength on both faces of the moving magnet. During the storage phase, electromagnets interact with both the north and south poles of the permanent magnet to create lift. A Halbach array, by design, suppresses the magnetic field on one side, which would have compromised the levitation and controlled the lifting of the mass by reducing the available magnetic interaction surface.

Furthermore, in the generation phase, when the magnetic mass descends through or past the copper coils, a Halbach array would have resulted in uneven electromagnetic induction. Because the field is concentrated on one side, the EMF induced in the coils would be heavily biased toward the side with the stronger field. For example, if the Halbach array were falling through a coaxial coil assembly, the positive EMF induced as the stronger side entered the coil would be disproportionately large compared to the EMF induced when the weaker side exited, potentially creating an imbalance in the AC waveform or reducing overall generation efficiency.

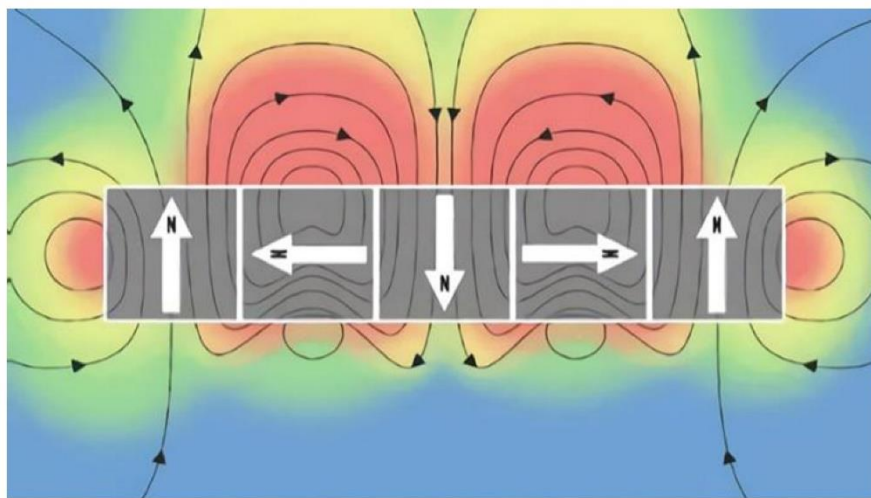


Figure 4.8.1 : Halbach Array Field Lines Diagram [77]

These asymmetries—in both field interaction and energy conversion—ultimately conflicted with the system's requirements for bidirectional and uniform magnetic performance. While the Halbach array remains a fascinating innovation in magnetics, its field characteristics were found to be misaligned with the symmetrical and consistent flux demands of the EMGES system architecture.

4.8.2 Integrated Three-Coil Loop Concept

Another concept considered during the EMGES design phase was the use of an integrated three-coil loop, as shown in Figure 4.8.2 below. This design involves three identical coils placed end-to-end along the same axis, spaced such that they occupy the same overall length as a single, continuous coil would. The coils are energized or induced individually, not connected in series or parallel.

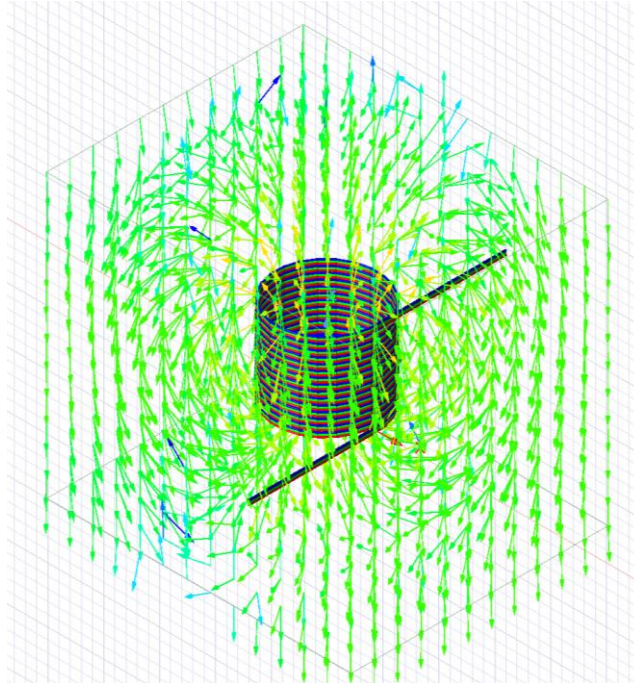


Figure 4.8.2 : 3-Coil Magnetic Flux Density Vectors

The original motivation for this layout was to explore whether energizing or extracting voltage from three separate coils in close proximity could yield a threefold voltage gain during the generation phase. This hypothesis was based on the idea that each coil, when exposed to a moving magnetic field, would independently induce a voltage, and that these could be harvested in parallel to increase output.

However, after further consideration and simulation, several challenges emerged:

- **Reduced Turns per Coil:** Because the same axial space is divided among three coils, the number of wire turns in each coil is roughly one-third of a single continuous coil design. Since induced voltage is directly proportional to the number of turns, the net voltage gain was effectively cancelled out.
- **Increasing Coil Length Not Practical:** To counteract the reduced number of turns, a logical workaround would be to increase the total coil length threefold, maintaining the same number of turns per coil. However, optimal coil length calculations—based on flux linkage and impedance matching—indicated that increasing coil length beyond a certain threshold reduces efficiency due to magnetic field tapering and internal resistance.

- **Magnetic Interaction with Permanent Magnets:** The spatial distribution of the three separate coils affects how their north and south faces interact with the passing PMs. In a traditional single-coil setup, the ends of the coil experience the highest magnetic flux density (B), leading to the strongest induced EMF. With three shorter coils spaced out, the strongest magnetic interactions occur only at the beginning and end of the full array, while the centre coil experiences a weaker gradient. This non-uniformity can result in asymmetric induction, reducing efficiency and potentially skewing the waveform.
- **Flux Leakage and Unused Field Regions:** The gaps between coils allow more magnetic flux to escape laterally rather than passing directly through the coil windings. This contributes to flux leakage, reducing the net amount of magnetic energy converted into electricity.

Ultimately, while visually and conceptually compelling, the three-coil design did not provide the performance improvements initially hoped for. The simplified layout of a single, optimally dimensioned coil remains the more effective approach for maximized EMF generation, symmetry in field interaction, and compact coil geometry.

4.9 Chapter Summary

This chapter evaluated the performance of the EMGES, combining experimental results, simulations, and modelling techniques to assess both storage and generation modes. Storage mode efficiencies were found to range from 0.49% to 1.87%, while generation mode tests yielded peak outputs of up to 18.5 W using a 135-turn coil, closely matching Ansys Maxwell predictions. Coil behaviour was further explored using LTSpice simulations, confirming the timing and polarity of current control logic. A levelized cost of storage (LCOS) analysis revealed high costs of €924–€1,258/kWh, driven largely by low efficiency and high coil costs. Scaling the system to a 400 m vertical shaft demonstrated a potential storage capacity of 2 kWh, though this also introduced challenges in current delivery and overall energy efficiency. Additional discussions considered unimplemented strategies such as Halbach arrays and waste heat utilisation as avenues for improving system performance.

The next chapter synthesises these findings, draws overarching conclusions, and outlines key recommendations for future development of the EMGES concept.

5 CONCLUSIONS AND FUTURE WORK

5.1 Summary of Findings

This study has explored the Electro-Magnetic Gravity Energy Storage System (EMGES) as a novel approach to renewable energy storage, producing several key findings from theoretical and experimental analyses. Simulations of a small-scale prototype, designed with 132 coils of 135 turns each, predicted the ability to lift a 2.2 N mass using 258.55 J (0.0718 Wh) in storage mode, with efficiencies ranging from 0.49% to 1.30% depending on wire gauge, while experimental tests demonstrated generation mode outputs of 1.04 J per drop at 79% efficiency, with instantaneous power scaling from 4.3 W to 18.5 W as coil turns increased from 45 to 135. Scaling the system to a 400 m shaft for a 2 kWh capacity, also simulated, improved storage efficiency to 1.87% with 3,000 turns, though the levelized cost of storage (LCOS) ranged from €924 to €1,258 per kWh, far exceeding that of established technologies such as lithium-ion (€200–€400/kWh) or pumped hydro (€100–€200/kWh). These findings, validated through Ansys Maxwell simulations and limited experimental data, confirm the technical potential of EMGES for DC power systems integration, yet reveal significant challenges with low efficiency and high costs that limit its current practicality for widespread application.

5.2 Conclusions

Conclusions are not simply a recap of results or discussions. This section takes a step back and looks at the overall aims and specific objectives you set for yourself, and the extent to which you achieved them. How does your work help address the issue that you set out to address? What were the truly key findings? What issues did you face that possibly impeded this progress?

This research set out to explore the feasibility of a novel Electro-Magnetic Gravity Energy Storage (EMGES) system, with the dual aim of supporting renewable energy integration and pioneering an alternative to conventional energy storage technologies. The project specifically targeted the development of a scalable, mechanically simple solution capable of storing and dispatching surplus solar energy on demand, using a combination of gravitational potential and electromagnetic induction.

The first aim—to enhance grid compatibility with intermittent renewables—was partially met. A 132-coil small-scale EMGES prototype was successfully designed, manufactured, and simulated in Ansys Maxwell. It demonstrated predictable EMF outputs (up to 18.5 W), consistent electromagnetic coupling, and a generation capacity of 1.04 J per coil per drop. This confirmed the theoretical feasibility of the energy conversion principle. However, while integration with solar PV systems was explored through LTSpice circuit models and power flow simulations, physical implementation of solar inputs and full grid integration was not

achieved, limiting the system's demonstrated capability to actively stabilise renewable energy fluctuations.

The second aim—to pioneer a novel energy storage concept—was effectively fulfilled through the development, validation, and performance evaluation of EMGES. The system was proven to operate using a passive gravitational fall of permanent magnets through copper coils, producing repeatable voltage waveforms and power outputs across both 45-turn and 135-turn coil configurations. It exhibited functional mechanical simplicity, scalability in design, and long-term sustainability by eliminating moving parts like cables or pulleys. These features directly address the technological gap identified in the literature surrounding ropeless gravity storage solutions.

The first objective—design and simulation of a small-scale EMGES—was achieved through the creation of a functioning prototype, validated both through laboratory experimentation and Ansys Maxwell simulations. The prototype confirmed that electromagnetic lift and generation could be realised using compact, concentric magnet-coil arrangements. Simulation results closely matched experimental outputs, particularly concerning EMF waveform shape and force profiles. This alignment confirmed that the foundational electromagnetic theory could effectively be applied to a real-world model.

In relation to the second objective—integration of EMGES with DC power systems—the project explored power electronics and coil activation strategies using LTSpice modelling. The design of H-bridge circuits and the testing of matched load conditions through instantaneous power simulation confirmed that EMGES could be interfaced with DC-based renewable systems like solar PV. While hardware integration with actual solar input was outside the project's scope, the simulated control logic forms a clear framework for such future integration.

The third objective—**evaluation of system performance and efficiency**—highlighted critical performance limitations. While the system achieved generation outputs of up to 18.5 W from a single coil, storage mode revealed low round-trip efficiencies of between 0.49% and 1.87%. These figures, though expected for an early-stage prototype, underscore the need for optimisation in force application, magnetic coupling, and electrical resistance management. Nevertheless, the work demonstrated that power could be generated through passive magnet descent, offering proof-of-concept for further development.

In addressing the final objective—**technical and economic feasibility analysis**—the thesis conducted a levelized cost of storage (LCOS) study for a full-scale 400 m shaft design. The analysis showed an LCOS of approximately €924–€1,258/kWh, far above conventional storage technologies, due primarily to low efficiency and high material costs. Two scaling methods were explored: the first was found to be infeasible due to excessive current requirements, while the second, using high-turn, low-current coils, offered a 22× improvement in efficiency and reduced current demands to practical levels. These findings highlight the EMGES concept's potential but also identify cost and performance challenges that must be overcome.

Key challenges included thermal losses, material limitations, and the difficulty of integrating coils into confined spaces—particularly in the disc magnet configuration. Time constraints prevented experimental validation of regenerative braking, Halbach arrays, or superconducting components, all of which represent promising areas for future work.

In summary, the EMGES system meets its conceptual aims: it offers a working model that merges gravitational and electromagnetic energy conversion, provides a pathway to renewable energy integration, and introduces a mechanically distinct alternative to battery-based storage. However, to become a viable grid-scale solution, the system must undergo substantial technical refinement and economic optimisation. This thesis provides the groundwork for such innovation and lays the foundation for continued exploration in the rapidly evolving field of gravity-based energy storage.

5.3 Future work

The research conducted in this thesis lays the groundwork for a novel electromagnetic gravity energy storage (EMGES) system, but several opportunities exist to further develop and refine both the methodology and the system design. These future directions are essential to improve efficiency, scalability, and integration with existing renewable energy systems.

One of the most immediate areas for future work involves enhancing the electromagnetic coupling efficiency of the system. Although the prototype successfully demonstrated energy recovery through falling permanent magnets, the round-trip efficiency remained below 2%. Optimisation of coil design—particularly through advanced winding geometries (e.g. layered or conical coils), higher fill factors, and alternative magnet arrangements such as Halbach arrays—may significantly increase the captured EMF. In parallel, the use of superconducting wire materials could drastically reduce resistive losses, especially in high-turn coil configurations, and improve the overall electrical-to-mechanical energy transfer ratio.

Further experimental work is also recommended to implement and test regenerative braking in the generation cycle. This technique, which was only simulated in this study, has the potential to slow the descent of the permanent magnet while extending the energy harvesting window, thereby increasing both energy output and flexibility in grid response.

At the system level, the EMGES design would benefit from exploration of multi-magnet operation. This approach, suggested in Section 4.6, would allow multiple PM units to descend in parallel with adequate spacing to avoid magnetic interaction. Such a configuration could provide stepwise energy delivery or allow higher instantaneous power outputs, making the system more adaptable to fluctuating grid demands. However, further simulation is required to validate spacing strategies, magnetic safety thresholds, and the control logic required for staggered coil activation.

In terms of control systems, the development of a microcontroller-based logic board capable of monitoring coil states and synchronising current flow through the coils in real time would

be a valuable next step. This would transition the design from simulation-based logic control (e.g. LTSpice PWL inputs) to a deployable system architecture with real-time responsiveness.

On the economic side, a full-scale techno-economic model incorporating potential cost reductions, advanced manufacturing techniques, and projected efficiency improvements is warranted. If future iterations of EMGES can push round-trip efficiency above 10%, levelized cost of storage (LCOS) could become competitive with niche or remote-use storage technologies. Additional analysis should also investigate hybridisation with other technologies—e.g., coupling EMGES with flywheels or battery banks to stabilise short-term delivery while the magnet cycles.

Finally, further refinement of the vertical shaft design and modular unit deployment should be explored. Customisable shaft lengths, support infrastructure for coil mounting, and autonomous lift/release mechanisms for the magnets could all contribute to a more robust and commercially viable system.

In summary, while the EMGES system presented in this thesis validates the foundational principles of ropeless gravity energy storage, considerable scope remains for improving efficiency, scalability, and control. Pursuing these future developments will be essential for moving EMGES from experimental concept toward practical, field-ready implementation in the growing landscape of renewable energy technologies.

6 REFERENCES

- [1] *Electronics Desktop.* (2025). [Online]. Available: <https://www.ansys.com/products/electronics/ansys-maxwell>
- [2] P. E. a. P. Experts, "Stationary Energy Storage Market Size, Share, and Trends 2025 to 2034," in "Energy and Power," Precedence Research, 1533, 2025, vol. 1. [Online]. Available: <https://www.precedenceresearch.com/stationary-energy-storage-market>
- [3] D. A. Elalfy, E. Gouda, M. F. Kotb, V. Bureš, and B. E. Sedhom, "Comprehensive review of energy storage systems technologies, objectives, challenges, and future trends," *Energy Strategy Reviews*, vol. 54, p. 101482, 2024/07/01/ 2024, doi: <https://doi.org/10.1016/j.esr.2024.101482>.
- [4] L. Pamfile, "Energy transition: the importance of energy storage systems towards a more sustainable world," *EMERG - Energy Environment Efficiency Resources Globalization*, vol. 9, pp. 37-61, 07/15 2023, doi: 10.37410/EMERG.2023.2.03.
- [5] M. E. Ölmez, I. Ari, and G. Tuzkaya, "A comprehensive review of the impacts of energy storage on power markets," *Journal of Energy Storage*, vol. 91, p. 111935, 2024/06/30/ 2024, doi: <https://doi.org/10.1016/j.est.2024.111935>.
- [6] T. M. Masaud, K. Lee, and P. K. Sen, "An overview of energy storage technologies in electric power systems: What is the future?," in *North American Power Symposium 2010*, 26-28 Sept. 2010 2010, pp. 1-6, doi: 10.1109/NAPS.2010.5619595.
- [7] Z. Li and D. Deusen, "Role of energy storage technologies in enhancing grid stability and reducing fossil fuel dependency," *International Journal of Hydrogen Energy*, vol. 102, pp. 1055-1074, 2025/02/10/ 2025, doi: <https://doi.org/10.1016/j.ijhydene.2024.12.489>.
- [8] M. Mann, S. Babinec, and V. Putsche, "Energy Storage Grand Challenge: Energy Storage Market Report," National Renewable Energy Laboratory (NREL), Golden, CO (United States), United States, 2020. [Online]. Available: <https://www.osti.gov/biblio/1908714>
<https://www.osti.gov/servlets/purl/1908714>
- [9] S. M. Schoenung, J. M. Eyer, J. J. Iannucci, and S. A. Horgan, "ENERGY STORAGE FOR A COMPETITIVE POWER MARKET," *Annual Review of Environment and Resources*, vol. 21, no. Volume 21, 1996, pp. 347-370, 1996, doi: <https://doi.org/10.1146/annurev.energy.21.1.347>.
- [10] S. M. Hoosh, H. Ouerdane, V. Terzija, and D. Pozo, "Assessing the Value of Energy Storage Systems for Distribution Grid Applications," in *2023 IEEE 7th Conference on Energy Internet and Energy System Integration (EI2)*, 15-18 Dec. 2023 2023, pp. 813-818, doi: 10.1109/EI259745.2023.10513229.
- [11] C. D. Botha and M. J. Kamper, "Capability study of dry gravity energy storage," *Journal of Energy Storage*, vol. 23, pp. 159-174, 2019/06/01/ 2019, doi: <https://doi.org/10.1016/j.est.2019.03.015>.
- [12] G. Bottenfield, K. Hatipoglu, and Y. Panta, "Advanced Rail Energy and Storage : Analysis of Potential Implementations for the State of West Virginia," in *2018 North American Power Symposium (NAPS)*, 9-11 Sept. 2018 2018, pp. 1-4, doi: 10.1109/NAPS.2018.8600665.
- [13] K. Chen, "Types, applications and future developments of gravity energy storage," *Highlights in Science, Engineering and Technology*, vol. 3, pp. 23-30, 07/08 2022, doi: 10.54097/hset.v3i.689.
- [14] ARES. "Advanced Rail Energy Storage." <https://aresnorthamerica.com/> (accessed).
- [15] Gravitricity. "Gravitricity." <https://gravity-storage.com/> (accessed).
- [16] C. D. Botha, M. J. Kamper, and R. J. Wang, "Design optimisation and cost analysis of linear vernier electric machine-based gravity energy storage systems," *Journal of Energy Storage*, vol. 44, p. 103397, 2021/12/15/ 2021, doi: <https://doi.org/10.1016/j.est.2021.103397>.
- [17] W. Tong *et al.*, "Solid gravity energy storage: A review," *Journal of Energy Storage*, vol. 53, p. 105226, 2022/09/01/ 2022, doi: <https://doi.org/10.1016/j.est.2022.105226>.

- [18] M. Franklin, P. Fraenkel, C. Yendell, and R. Apps, "5 - Gravity energy storage systems," in *Storing Energy (Second Edition)*, T. M. Letcher Ed.: Elsevier, 2022, pp. 91-116.
- [19] J. D. Hunt *et al.*, "Lift Energy Storage Technology: A solution for decentralized urban energy storage," *Energy*, vol. 254, p. 124102, 2022/09/01/ 2022, doi: <https://doi.org/10.1016/j.energy.2022.124102>.
- [20] J. D. Hunt *et al.*, "Buoyancy Energy Storage Technology: An energy storage solution for islands, coastal regions, offshore wind power and hydrogen compression," *Journal of Energy Storage*, vol. 40, p. 102746, 2021/08/01/ 2021, doi: <https://doi.org/10.1016/j.est.2021.102746>.
- [21] F. Cava, J. Kelly, W. Peitzke, M. Brown, and S. Sullivan, "Chapter 4 - Advanced Rail Energy Storage: Green Energy Storage for Green Energy," in *Storing Energy*, T. M. Letcher Ed. Oxford: Elsevier, 2016, pp. 69-86.
- [22] R. Mohan. "Disruptors : Gravity based Energy Storage - Energy Vault." <https://www.linkedin.com/pulse/disruptors-gravity-based-energy-storage-vault-rohit-mohan?> (accessed).
- [23] A. Berrada, A. Emrani, and A. Ameur, "Life-cycle assessment of gravity energy storage systems for large-scale application," *Journal of Energy Storage*, vol. 40, p. 102825, 2021/08/01/ 2021, doi: <https://doi.org/10.1016/j.est.2021.102825>.
- [24] E. Vault. "Energy Vault." <https://www.energyvault.com/> (accessed).
- [25] M. A. Hannan *et al.*, "Battery energy-storage system: A review of technologies, optimization objectives, constraints, approaches, and outstanding issues," *Journal of Energy Storage*, vol. 42, p. 103023, 2021/10/01/ 2021, doi: <https://doi.org/10.1016/j.est.2021.103023>.
- [26] A. A. Kebede *et al.*, "Techno-economic analysis of lithium-ion and lead-acid batteries in stationary energy storage application," *Journal of Energy Storage*, vol. 40, p. 102748, 2021/08/01/ 2021, doi: <https://doi.org/10.1016/j.est.2021.102748>.
- [27] A. R. Dehghani-Sanij, E. Tharumalingam, M. B. Dusseault, and R. Fraser, "Study of energy storage systems and environmental challenges of batteries," *Renewable and Sustainable Energy Reviews*, vol. 104, pp. 192-208, 2019/04/01/ 2019, doi: <https://doi.org/10.1016/j.rser.2019.01.023>.
- [28] Z. Yang *et al.*, "Electrochemical Energy Storage for Green Grid," *Chemical Reviews*, vol. 111, no. 5, pp. 3577-3613, 2011/05/11 2011, doi: 10.1021/cr100290v.
- [29] A. Z. Weber, M. M. Mench, J. P. Meyers, P. N. Ross, J. T. Gostick, and Q. H. Liu, "Redox flow batteries: a review," *JOURNAL OF APPLIED ELECTROCHEMISTRY*, vol. 41, no. 10, pp. 1137-1164, OCT 2011, doi: 10.1007/s10800-011-0348-2.
- [30] U. Koehler, "Chapter 2 - General Overview of Non-Lithium Battery Systems and their Safety Issues," in *Electrochemical Power Sources: Fundamentals, Systems, and Applications*, J. Garche and K. Brandt Eds.: Elsevier, 2019, pp. 21-46.
- [31] J. P. Deane, B. P. Ó Gallachóir, and E. J. McKeogh, "Techno-economic review of existing and new pumped hydro energy storage plant," *Renewable and Sustainable Energy Reviews*, vol. 14, no. 4, pp. 1293-1302, 2010/05/01/ 2010, doi: <https://doi.org/10.1016/j.rser.2009.11.015>.
- [32] R. M. Nienhuis, M. van Rooij, W. A. Prins, B. Jayawardhana, and A. I. Vakis, "Investigating the efficiency of a novel offshore pumped hydro energy storage system: Experimental study on a scale prototype," *Journal of Energy Storage*, vol. 74, p. 109374, 2023/12/25/ 2023, doi: <https://doi.org/10.1016/j.est.2023.109374>.
- [33] S. Galant, E. Peirano, and L. Debarberis, "Electricity Storage: A New Flexibility Option for Future Power Systems," *Power Systems*, vol. 69, pp. 247-284, 10/01 2013, doi: 10.1007/978-1-4471-4549-3_7.
- [34] S. Rehman, L. M. Al-Hadhrami, and M. M. Alam, "Pumped hydro energy storage system: A technological review," *Renewable and Sustainable Energy Reviews*, vol. 44, pp. 586-598, 2015/04/01/ 2015, doi: <https://doi.org/10.1016/j.rser.2014.12.040>.
- [35] H. Ibrahim, A. Ilinca, and J. Perron, "Energy storage systems—Characteristics and comparisons," *Renewable and Sustainable Energy Reviews*, vol. 12, no. 5, pp. 1221-1250, 2008/06/01/ 2008, doi: <https://doi.org/10.1016/j.rser.2007.01.023>.

- [36] J. I. Pérez-Díaz, M. Chazarra, J. García-González, G. Cavazzini, and A. Stoppato, "Trends and challenges in the operation of pumped-storage hydropower plants," *Renewable and Sustainable Energy Reviews*, vol. 44, pp. 767-784, 2015/04/01/ 2015, doi: <https://doi.org/10.1016/j.rser.2015.01.029>.
- [37] J. Menéndez, J. M. Fernández-Oro, M. Galdo, and J. Loredo, "Efficiency analysis of underground pumped storage hydropower plants," *Journal of Energy Storage*, vol. 28, p. 101234, 2020/04/01/ 2020, doi: <https://doi.org/10.1016/j.est.2020.101234>.
- [38] R. Madlener and J. M. Specht, "An Exploratory Economic Analysis of Underground Pumped-Storage Hydro Power Plants in Abandoned Deep Coal Mines," *Energies*, vol. 13, p. 5634, 10/28 2020, doi: 10.3390/en13215634.
- [39] Z. Zhao *et al.*, "Stability and efficiency performance of pumped hydro energy storage system for higher flexibility," *Renewable Energy*, vol. 199, pp. 1482-1494, 2022/11/01/ 2022, doi: <https://doi.org/10.1016/j.renene.2022.09.085>.
- [40] E. Pujades, P. Orban, S. Bodeux, P. Archambeau, S. Erpicum, and A. Dassargues, "Underground pumped storage hydropower plants using open pit mines: How do groundwater exchanges influence the efficiency?," *Applied Energy*, vol. 190, pp. 135-146, 2017/03/15/ 2017, doi: <https://doi.org/10.1016/j.apenergy.2016.12.093>.
- [41] A. H. Alami, M. Ayoub, A. Yasin, A. Alashkar, H. Aljaghoub, and S. A. Alabdalla, "Performance assessment of buoyancy work energy storage system with various buoy materials, coatings, and gasses," *Journal of Energy Storage*, vol. 72, p. 108524, 2023/11/25/ 2023, doi: <https://doi.org/10.1016/j.est.2023.108524>.
- [42] G. Power. "Gravity Power Module." <https://www.gravitypower.net/> (accessed).
- [43] Gravity-Storage. "Hydraulic Hydro." <https://gravity-storage.com/> (accessed).
- [44] E. Heindl, "Hydraulic Hydro Storage System for Self-sufficient Cities," *Energy Procedia*, vol. 46, pp. 98-103, 2014/01/01/ 2014, doi: <https://doi.org/10.1016/j.egypro.2014.01.162>.
- [45] EscoVale. "Ground Breaking Energy Storage." <https://www.escovale.com/GBES.php> (accessed).
- [46] J. Hunt, W. Tong, and Y. Wada, "Deep Ocean Gravity Energy Storage: An Affordable Seasonal Energy Storage Alternative," *SSRN Electronic Journal*, 09/19 2024, doi: 10.2139/ssrn.4961170.
- [47] T. M. I. Mahlia, T. J. Saktisahdan, A. Jannifar, M. H. Hasan, and H. S. C. Matseelar, "A review of available methods and development on energy storage; Technology update," *Renewable and Sustainable Energy Reviews*, vol. 33, pp. 532–545, 05/01 2014, doi: 10.1016/j.rser.2014.01.068.
- [48] H. Chen, T. N. Cong, W. Yang, C. Tan, Y. Li, and Y. Ding, "Progress in electrical energy storage system: A critical review," *Progress in Natural Science*, vol. 19, no. 3, pp. 291-312, 2009/03/10/ 2009, doi: <https://doi.org/10.1016/j.pnsc.2008.07.014>.
- [49] GridRadar. "Real-time behaviour of power frequency." <https://gridradar.net/en/mains-frequency> (accessed).
- [50] R. Ravaud, G. Lemarquand, S. Babic, V. Lemarquand, and C. Akyel, "Cylindrical Magnets and Coils: Fields, Forces, and Inductances," *Magnetics, IEEE Transactions on*, vol. 46, pp. 3585-3590, 10/01 2010, doi: 10.1109/TMAG.2010.2049026.
- [51] M. Behtouei, F. Luigi, S. Bruno, V. Alessandro, and M. and Migliorati, "A novel exact analytical expression for the magnetic field of a solenoid," *Waves in Random and Complex Media*, vol. 32, no. 4, pp. 1977-1991, 2022/07/04 2022, doi: 10.1080/17455030.2020.1842554.
- [52] R. Flükiger, "Overview of Superconductivity and Challenges in Applications," *Reviews of Accelerator Science and Technology*, vol. 05, pp. 1-23, 01/01 2012, doi: 10.1142/S1793626812300010.
- [53] J. M. D. Coey, *Magnetism and Magnetic Materials*. Cambridge: Cambridge University Press, 2010.
- [54] D. J. Griffiths, *Introduction to Electrodynamics*. 1942.

- [55] E. E. Callaghan and S. H. Maslen, "THE MAGNETIC FIELD OF A FINITE SOLENOID," United States, 01 1960. [Online]. Available: <https://www.osti.gov/biblio/4121210>
- [56] J. L. Simpson, John Immer, Christopher Youngquist, Robert, "Simple Analytic Expressions for the Magnetic Field of a Circular Current Loop," 2001. [Online]. Available: <https://ntrs.nasa.gov/api/citations/20010038494/downloads/20010038494.pdf>.
- [57] T. P. Hypertextbook. "Ampere's Biot-Savart Law." <https://physics.info/law-ampere/> (accessed.
- [58] E. P. Furlani, "Chapter 3 - Field Analysis," in *Permanent Magnet and Electromechanical Devices*, E. P. Furlani Ed. San Diego: Academic Press, 2001, pp. 97-205.
- [59] E. P. Furlani, "Chapter 2 - Review of Maxwell's Equations," in *Permanent Magnet and Electromechanical Devices*, E. P. Furlani Ed. San Diego: Academic Press, 2001, pp. 73-95.
- [60] E. P. Furlani, "Chapter 4 - Permanent Magnet Applications," in *Permanent Magnet and Electromechanical Devices*, E. P. Furlani Ed. San Diego: Academic Press, 2001, pp. 207-333.
- [61] E. P. Furlani, "Chapter 1 - Materials," in *Permanent Magnet and Electromechanical Devices*, E. P. Furlani Ed. San Diego: Academic Press, 2001, pp. 1-72.
- [62] D. Jiles, *Introduction to Magnetism and Magnetic Materials*, 3 ed. 2015, p. 626.
- [63] S. Babic and C. Akyel, "Improvement in the analytical calculation of the magnetic field produced by permanent magnet rings," *Progress In Electromagnetics Research C*, vol. 5, pp. 71-82, 09/28 2008.
- [64] R. Ravaud, G. Lemarquand, V. Lemarquand, and C. Depollier, "Analytical Calculation of the Magnetic Field Created by Permanent-Magnet Rings," *Magnetics, IEEE Transactions on*, vol. 44, pp. 1982-1989, 09/01 2008, doi: 10.1109/TMAG.2008.923096.
- [65] S. Wu. "AWG standard wire gauge and current comparison table." <https://www.romtronic.com/awg-standard-wire-gauge-and-current-comparison-table/#:~:text=Divide%20the%20range%20between%20a,the%20outer%20diameter%20and%20current>. (accessed).
- [66] DGcourage. "Various Shape Types of Neodymium Magnets." <https://www.dgcourage.com/xinwen/hyxw/708.html> (accessed).
- [67] "The Hysteresis Loop." Iowa State University. <https://www.nde-ed.org/Physics/Magnetism/HysteresisLoop.xhtml#:~:text=A%20great%20deal%20of%20information,to%20as%20the%20B%2DH%20loop>. (accessed).
- [68] D. Carroll, "Miniaturised Electromagnetic Generators for Portable Applications," PhD PhD, Electrical and Electronic Engineering, National University of Ireland, Galway, National University of Ireland, Galway, 2012.
- [69] VCELINK. "A Deep Dive into Wire Gauge." <https://www.vcelink.com/blogs/focus/a-deep-dive-into-wire-gauge> (accessed).
- [70] LTSpice. [Online]. Available: <https://www.analog.com/en/resources/design-tools-and-calculators/ltpice-simulator.html>
- [71] Excel. (2025). [Online]. Available: <https://www.microsoft.com/en-ie/microsoft-365/excel>
- [72] Python. (2025). [Online]. Available: <https://www.python.org/>
- [73] Infineon, "IRF3205," ed, 2010.
- [74] L. Technology, "LTC4357," ed.
- [75] Infineon, "IRS2004," ed.
- [76] L. Technology, "LTC3105," ed, 2015.
- [77] J. Qin, M. Feng, and Q. Cao, "Processing Optimization for Halbach Array Magnetic Field-Assisted Magnetic Abrasive Particles Polishing of Titanium Alloy," *Materials*, vol. 17, p. 3213, 07/01 2024, doi: 10.3390/ma17133213.